DESIGN STUDY OF AN EARTHQUAKE RESCUE ROBOT

By

Zhelong Wang

School of Engineering

University of Durham

A thesis submitted to the University of Durham

for the degree of Doctor of Philosophy

2004

To Yuzhuo, Yingrui, my parents and sister

ABSTRACT

This thesis describes the design of a brush robot for earthquake rescue and for traversing pipes with varied cross sectional shape. Earthquake rescue is a very dangerous, difficult and challenging task, in which emergency services rescue people who are trapped in man-made structures, such as collapsed buildings after an earthquake. The building collapse may have been caused by natural or man-made events. This technology is also applicable to tunnel collapse and land slips. The focus of this work is finding the location of victims and provision of primary life support and communications. To illustrate the concept of the robot, the thesis first discusses the current development of rescue robots and pipe robots. Then the thesis focuses on the description of a brush based pipe robot, developed by the University of Durham, which would be used as the basis of an earthquake rescue robot. The concept of the robot was illustrated and compared with other current rescue robots and pipe robots. After outlining the advantages of this robot concept, a robot body shape change theory was proposed and theoretical simulations were used to verify the practicality of the robot shape change theory. The thesis also illustrates the design of the working principle and design of a robot sensor, which was subsequently used in the robot shape change experiments. The robot body shape change experiments and the experimental results are described and discussed. The experimental results illustrate the robot concept and support the robot body shape change theory. Chapter 6 focuses on the brush unit traction investigation, bristle theory and mathematical model. Furthermore, the bristle theory and mathematical model were used to explain the variation of traction force in the traction experiments.

It was concluded that the robot shape change algorithm and mechanism were found feasible by use of computer simulation and lab experiments. Research results of the brush unit traction experiments, bristle theory and mathematical model can be used as guidance for future robot design. Further work is proposed for the improvement of the current robot concept and for robot field experiments.

ACKNOWLEGEMENTS

I would like to express my sincere thanks to my supervisor, Prof. Ernest Appleton, for his valuable advice, professional guidance, enthusiastic encouragement and assistance throughout this research. His patience and time spent on editing this thesis has been invaluable to the production of the thesis.

I wish to forward my gratitude to the Audi Foundation for providing funds for the development of the robot prototype and experiments. The gratitude is also extended to University of Durham, which sponsored me to pursue a Ph.D. study and carry out this research.

I would like to thank all the technical staff of the School of Engineering, University of Durham. Particular thanks are due to the Mechanical Workshop and Electric Workshop, including Neil Clarey, Brian Blackburn, Colin Dart, Harry Kelly, Colin Wintrip, Ian Hutchinson, etc. Thanks also go to Andrew Yates in the Bioengineering Lab, Bernie McEleavey and Stephen Richardson in the Civil Engineering Lab for their help with all the gauge calibration and measurement work.

A special thank you to Jonathan Southgate and Neil Stutchbury for their constructive discussions and great help to polish my English.

Thanks to my parents, my sister and Yuzhuo for their love and continuous support.

Finally, I would like to thank all players of the Durham Chinese Football Team. I shared unforgettable enjoy, experience and time in the regular Sunday football match, where I gained the energy and encouragement to benefit my research work.

DECLARATION

This thesis is the result of my own work. No part of the thesis has been submitted for a degree in this or other Universities.

Zhelong Wang

University of Durham

2004

TABLE OF CONTENTS

LIST OF FIGURES

LIST OF TABLES

GENERAL NOTATION

β	Bristle tip angle (Radian)
ε	Engineering strain
Δe	Bridge output voltage (V)
θ	Complementary angle of the friction angle (Radian)
μ	Friction coefficient
d	Bristle diameter (mm)
E	Modulus of elasticity
F	Force (N)
F_n	Normal force (N)
F_μ	Bristle friction force (N)
F_X, F_Y, F_Z, F_W	Forces acting on the steel strip hoop (N)
G_1	Strain gauge resistance (Ω)
h	Projected bristle length (mm)
I	Second moment of area
K	Coefficient of Euler theory model
l	Bristle length (mm)
l_{opt}	Optimum projection of the bristle (mm)
L	Chord length (mm)
L_i	Deflection (mm)
P	Thrust force (N)
R_i	Resistance of resistor arm (Ω)
V	Output voltage (V)

V_i	Output voltage (V)
V_L	Cantilever deflection length (mm)
x_i, y_i	Coordinates of a point on the steel strip hoop
X_i, Y_i	Coordinates of a point on the void wall

Specific symbols can be found in the relevant text.

CHAPTER 1

INTRODUCTION

This thesis deals with the concept and prototype study of a brush-based earthquake rescue robot. This concept is based on an innovative pipe crawling vehicle invented in the School of Engineering, University of Durham. The rescue robot could be used in earthquake rescue and in pipes with various cross sections.

1.1 GENERAL INTRODUCTION TO ROBOTICS

Robot entered the English vocabulary with the translation of Karel Capek's play R.U.R. (Rossum's Universal Robots) in 1923 (Seig, J., 1992). Capek was a Czech, and in his native language the word robot simply meant a worker. In the play, robots were the humanoid creations of Rossum and his son, constructed in the fond hope that they would perform obediently in the service of man. Now, thanks to Capek and a generation of science fiction writers, everyone knows what a robot is. The popular conception is a mechanical man, crammed full of near-miraculous components, and capable of clumsy imitations of human actions and speech. They are generally thought to combine superhuman strength with superhuman intelligence. (Seig, J., 1992)

Apart from the fictional description, robotics has become an extremely important discipline within its short history. The study of robots involves elements of mechanical and electrical engineering, as well as control theory, computing and artificial intelligence, etc.

Originally, robots were intended to replace human workers. More recently, newer forms of robots are promoted as being able to do jobs humans cannot perform, such as working in hazardous environments in the mining, offshore oil and nuclear industries or in fire fighting. Robots can work in places inaccessible to humans, in outer space, on the seabed or inside contorted pipework. Finally, robots can work on a scale humans find difficult, for instance in very large-scale assembly or handling tasks. Alternatively, robots can manipulate objects at an almost microscopic scale.

There are three main areas in which robots can be used but these areas should not be thought of as necessarily separate, as there is considerable overlap between them. The areas include production, exploration and aids for handicapped people (Seig, J., 1992). Generally, much of the current research can be seen as leading to robots capable of working in disordered environments and able to deal with greater levels of uncertainty. In the U.K., research in these areas has been termed 'advanced robotics' and many developments are underway, particularly in domestic robots, which could perform housework and medical robots for surgery. For example, Prassler introduced the current development of cleaning robots in his paper (Prassler, E., 2000). For application in agricultural engineering, Sarig described robots for fruit harvesting (Sarig, Y., 1993). The harvesting robots were designed to be able to

emulate the human picker and automatically judge fruit quality as well as undertaking fruit picking. Manipulators, which can replace lost human limbs, have been possible for some years now. The development of robots for use by the disabled is also a small but lively area of research.

In Cambridge University, a diamond-cutting robot was developed to analyse, cut and polish gems. The robot was claimed to be able to cut gems faster and more accurately than skilled craftsmen. Gemonologyists say that working with small gems takes its toll on human eyesight and the dust produced is a particular health hazard. The robot is set to reduce these risks as well as producing a more efficient production method and a much superior end product. (CUEA, 1995)

Internet technology allowed a new research branch in robotics, which is web telerobotics. A web telerobot in the University of Western Australia has attracted a large number of visitors who access the site. Visitors are able to operate the lab-based robot remotely (Trevelyan, J., 1999). In University of Essex, a remote operator can control an internet-based mobile robot to navigate a laboratory with visual feedback and a simulated environment map via internet (Hu, H., 2001). The web telerobots could have a great potential value for recreation and other uses in the future.

Now robots have appeared in almost all sectors in our community. Many of them have completely or partially taken the place of human being to do work. It is anticipated that more robots, with more advanced intelligence, will be developed to serve the human being community in the next decades.

1.2 URBAN SEARCH AND RESCUE (USAR)

On the 17th January 1995, an earthquake of magnitude 7.2 Richter scale hit Kobe City, Japan, killing over 6,432 people, injuring at least 43,800 people (recorded in hospitals) and crushing houses belonging to one-fifth of the city's 1.5 million people. Approximately 104,900 buildings completely collapsed and only 20 percent of the city's buildings were usable after the earthquake. The damage area covered a strip of land 13 miles (20.92km) by 0.6 (0.96km) miles and over 2,300,000 people were seriously affected. The cost of repair of the basic infrastructure damage exceeded $100 billion and total property damage, including private properties was well in excess of $1 trillion. Similar tragedies have also taken place in the U.S.A., Turkey and Taiwan. (Kitano H. et al, 2001)

The great danger and difficulties encountered in the earthquake rescue have made researchers to start a new research filed named USAR. USAR is an abbreviation for Urban Search and Rescue, where people are trapped or lost in man-made structures, such as collapsed buildings. USAR is a very dangerous, difficult and challenging task. It requires different skills, training and equipment from Wilderness Search and Rescue, for example, when someone gets lost on a mountain.

1.2.1 USAR issues and USAR robots

Urban search and rescue is a difficult and risky task. Victims may be buried under rubble piles created by collapsed structures. Search activities are impeded by

hazardous conditions and confined spaces that deny human access to voids, which may contain survivors.

Structural instability is one of the factors that make a rescue activity difficult. 135 rescuers died in the Mexico City rescue effort in 1985, 65 of them were trapped in confined spaces and flooded areas. As rescue teams search damaged structures, falling debris and further collapse threatens the safety of the rescue teams. For example, after shocks, high winds can create further casualties through falling debris or structural collapse. Hygroscopic materials, which were used to build the structure, may absorb liquids and add stress to already weakened structures. These factors often interrupt rescue operations until an acceptable factor of safety can be restored to the site. This restoration task can be very difficult because structural engineers need to look at blueprints of the structure to understand its layout, analyse the characteristics of the damaged structure and compute appropriate shoring-up points. These precautions will cost precious time for survivors who are in a serious condition and need immediate rescue. (Borden, W., 1994)

Confined workspace also makes the rescue task difficult. Survivors in collapsed structures are most often found in voids, which are created by partial structural failure. Sharp objects such as broken glass or twisted steel bars often protrude into the voids. These voids vary extensively in size, location and volume. It is essential for crisis site managers to identify such voids and survivor locations to allocate rescue assets effectively. Small size voids may be too small for human or rescue dogs to enter. Sharp objects may hurt rescue workers and dogs. In addition, a wealth of sensory distractors such as random noise, scattered clothing, and false

odours may exacerbate the problem of discriminating between potential survivors and those already dead. (Borden, W., 1994)

Fire and hazardous materials are often found in crisis sites. However, disrupted emergency services have to allow for fires, toxic contamination and electrical power disruption, which may continue unchecked for extended periods. Fire fighters and rescue workers will be unable to operate in such areas without a supply of water, electrical power and protective clothing. The search for survivors often has to wait until such collateral threats can be controlled before rescue teams can gain access to these areas. (Borden, W., 1994)

It often happens that there are insufficient properly trained and certified rescuers during USAR. It takes special, time-consuming certification to be qualified for USAR, on top of regular fire rescue credentials. For example, in the USA, only certified rescue workers can enter a collapsed site and even then it must be shored up and meet OSHA (Occupational Safety & Health Administration) confined space regulations. So, there are relatively few qualified rescuers for USAR. A study by the Federal Emergency Management Agency in the USA indicated that if a person is trapped in a void space inside a building, the average removal time is four hours and requires ten rescue workers. If that person happens to be entombed, pancaked or wedged in the rubble, the average time jumps to ten hours with ten rescue workers. Hence, if a major earthquake happens, there will not be enough certified workers to work round the clock. (Murphy, R. et al, 2000 a)

As a consequence of the above, expendable USAR robots are a solution to some of this dangerous rescue work. Some USAR robots were demonstrated in the 2000 Disaster and Rescue conference in Miami, where a collapsed building was used to test these robots. While the rescuers began the time-consuming process of shoring up the entry points, to permit safe human entry, the robots were inserted through a small hole and started getting camera data, showing things the rescuers could not see from outside (Murphy, R. et al, 2000 b). In this way, robots were found to speed rescue work quite considerably.

Current technologies cannot produce a fully autonomous robot, which can find and rescue victims. However, robots that are used in conjunction with existing USAR personnel are now possible. In order to develop a robot that can be used by USAR personnel in practical rescue tasks, some design issues need to be addressed.

A USAR robot needs the ability to not only detect that a live victim exists in a rubble pile but also precisely locate that victim relative to the rescuers. To fulfill this requirement, the robot needs to be able to travel through voids and conduct the rescue search. This thesis mainly focuses on the concept and laboratory research of a shape reconfigurable brush robot, which can change its body shape to negotiate various voids. Position locating instruments are needed to record the victim's position. A microphone can be attached to the robot to enable victims to talk with rescuers. A camera can give visual information in voids and observation of the victims. A CO_2 detector may also be helpful to detect whether victims are alive or not. A gas detector may be used to detect the explosive gas in the voids. In addition, a suitable communication system and control system needs to be thoroughly considered and

designed for specific USAR applications. Furthermore, to be able to work in the complicated and harsh environment in a crisis site, which may have fires, flammable gas, toxic gas, flood, and sharp objects, USAR robot will be required to be waterproof, fireproof, robust and durable. Some technical challenges facing the USAR robot design will be described in section 1.3.3. Research of this concept is still at an initial stage, so detailed technical specifications are not considered here but will be addressed later.

1.2.2 The tasks of robots in USAR

There are four major tasks that USAR robots could undertake:

(1) Reconnaissance and site assessment.

In this process, the Incident Commander and structural engineers look over the site and determine where the hazards are, places to start searching, etc. This takes in the order of a few hours and rescue cannot proceed until this is done. As a consequence, having robots to explore, sample, record the data and use special sensors could help to speed up the process.

(2) Rescuer safety: environmental and structural monitoring.

Rescuers have to be vigilant about their safety. In trench collapses, the rescuers have to vacate about every hour so that another rescuer with specialized equipment can check for gas leaks and signs of a cave-in. If a robot could stay just ahead of the rescuer, it would be able to warn of danger.

(3) Victim detection in the rubble.

Eighty percent of the survivors in a building collapse are surface victims, who were mostly on the edges or top of the structure (Casper J., 2002). They are easier to find. The other twenty percent are buried in the interior and are hard to find. Robots could help to locate these people.

(4) Mapping and characterizing the structure.

At some points, the Incident Commander has to determine the best way and points at which to start removing rubble. Imagine a robot that has recorded all the data about the structure or could build a 3D model of where it had been and the material composition of the structure. Such information would be invaluable to the incident commander.

However, USAR robots cannot replace humans and dogs in all aspects of rescue work and they are just one tool to be applied. Rescue dogs do not replace people; they do things that people cannot do such as using smell to search and detect people. Dogs cannot enter very small confined spaces with lots of glass and sharp rubble without injury. Also, some collapses are too risky for dogs. If a person or a dog cannot get into an area, the only other option is to use a search camera or camera on a jointed pole. The longest search camera can reach to 18 feet (5.49m) and even that is difficult to use (Murphy, R. et al, 2000 a). Hence, small mobile robots could do things that people and dogs or current equipment cannot do or would be too dangerous.

1.2.3 Technical challenges to USAR robots

A USAR task is very difficult in terms of mobility, sensing, and communications. USAR robots are required to have intelligence, not just be operated by a joystick. First of all, think about a wheeled robot in a collapsed building. The collapsed building has lots of rubble, fabric and rugs that can get wrapped around wheels and treads. Then consider that some parts will be dry and some will be muddy because the emergency sprinkler system or water main has broken. As a result, it is difficult for the robot to move around and not get stuck. US army studies (Mills C., 1995) show that people are poor at teleoperating vehicles using the view from a camera. Research shows that operators experience problems with robots becoming stuck very easily, even when they are aware of obstacles. It is just too difficult to predict all the problems. Sensing is also a problem. Cameras are useful but not suitable for all conditions because in a building collapse, everything looks grey, from being covered by cinderblock, sheetrock, and ceiling tile dust. It is very hard for the human eye to detect people unless they are conscious and moving or have shaken some dust off. Plus, there are no lights. Sound is hard to use to locate the victim's position because of echoes. Infrared or thermal cameras are very desirable but interpreting the images is difficult.

For a joystick-controlled robot, wireless communication is difficult to maintain. In the earthquake in Turkey in 1999, a large number of people in residential buildings were able to use their cell phones and call for help and guide rescue workers. However, cell phone coverage is unreliable inside large buildings or multi-story car parks because of all the structural steelwork. Operators may routinely lose

communications with the robot when the robot is not within range, making a teleoperated robot less useful than a search camera.

If an operator tries to use wireless communications to control a robot, the robots can need 1000 times more bandwidth than a cell phone just to let someone drive it very slowly using a camera (Murphy, R. et al, 2000 a). There is also the question of what happens if the signal is lost? This depends on the manufacturer; the robot either keeps doing the last thing it was doing or stops and does nothing. The robot needs onboard intelligence to either go back towards the starting point or try to move forward hoping to re-establish a link. Hence, by way of an example the USAR robot needs to have intelligence in order not to collide with something, drive past a victim, or fall off a ledge whilst doing a task.

1.2.4 The history of USAR robots

Looking over the robotics literature for the past 30 years, USAR has always been talked about as a good application for robotics. Prof. Shigeo Hirose in the Tokyo Technical Institute was probably the first person to build robots specifically for USAR. Robin Murphy in the University of South Florida appears to be the first to have a sustained focus on artificial intelligence for USAR robotics. (Mills, C., 1995) Fortunately, many researchers are getting involved these days, both because of the terrible earthquakes in Turkey and Taiwan and because of the challenge. Prof. Satoshi Tadokoro in Kobe University became involved when one of his graduates was trapped for several days during the Kobe earthquake. (Mills, C., 1995) A competition called

RoboCup Rescue is dedicated to encouraging researchers to develop intelligent robots for USAR.

In the US, as a new rising research field, USAR robot research is funded by some large research organizations, such as FEMA (the Federal Emergency Management Agency), NSF (National Science Foundation), DARPA (Defence Advanced Research Projects Agency), etc. Industry is another funding source because if a robot can be used for USAR, it also can be used to access a possible biological, chemical, or nuclear spill, or help gather data in a hostile situation.

1.2.5 Types of USAR robots

To date, there are three types of USAR robots:

(1) Tethered wheeled vehicle, where a long cable (sometimes called an umbilical cord) connects the robot to a computer and power supply outside the accident site. Inuktun Services in Canada is a leading manufacturer of these robots for the chemical industry. The robot concept studied in this thesis is a tethered robot because the robot is pneumatically driven by means of an air hose.

(2) Untethered wheeled vehicle, tactical mobile robots, which have an onboard computer and battery in order to be fully autonomous. The RWI (Robot Wars Inc.) is a well known manufacturer of these robots.

(3) Snakes, or robots that look and move like snakes. These are generally tethered but remain laboratory models and it will be sometime before they can actually work in the

field. Howie Choset at Carnegie Mellon University and Edward Grant at North Carolina State University have been working on such USAR snake robots. (Edward, G., 1999)

A tethered rescue robot made by Inuktun Services costs about US$8-13K. An untethered urban robot that can climb stairs costs about US$33-40K. These prices do not include specialized sensors. A miniature infrared camera that sees body heat costs about US$15K, but here most of the cost is related to very specialized prototypes. There are only about 40 urban rescue robots in the world. If there were thousands of them, the price would drop. It is suggested that US fire rescue departments cannot realistically budget for a USAR robot until the cost drops to the order of $10K or less (Casper, J. et al, 2000). That would make it one of the most expensive tools, so there would probably be some hesitation to use it in risky situations for fear of damage or loss, which of course defeats the purpose. Robin Murphy suggests that, in fact, $3K is a more acceptable price, including sensors. It is possible for USAR robots to be mass-produced and thus be less expensive within several years, if advances in hardware and software continue to make progress.

1.3 AIMS AND OBJECTIVES OF THIS THESIS

The Durham pipe crawling robot is based on a simple working principle, that is, if a brush is inserted into a pipe and its bristles are swept back at an angle, then, it is easier to push the brush forwards through the pipe than pull it backwards. Thus, if a reciprocating cylinder interconnects two brush units, then, by cycling the cylinder, it is possible for the robot to crawl through the pipe (Stutchbury, N., 1999). This pipe

crawling robot can travel through fixed diameter pipes with a circular cross section. Work in this thesis explores the design of a new crawling pipe robot prototype, which can travel through voids and go through pipes with various non-circular cross sections. The shape changing principle of the robot is simple. That is, if a hoop that is made of a thin spring steel strip is squeezed in mutually perpendicular directions, the hoop will change its shape to an approximate square, a square, an approximate rectangle or an ellipse. The robot shape change mechanism is modelled by a mathematical algorithm and its feasibility has been proven by computer simulations. In practice, an experimental device, including robot void shape sensor, robot body component and related control system software was used to investigate feasibility in a laboratory environment. Traction force that the robot could achieve and the interaction between the robot brush unit and the void wall were investigated by means of experiments and experimental results were analysed by means of mathematical models.

1.4 THESIS OUTLINE

The initial introduction and review of the current development of robotics, particularly in the USAR robot field, reveals that USAR robot is a promising research field, which could extend the ability to access hazardous and ill-constrained environments. There is a high demand for a USAR robot that could effectively help a rescue team to do urban rescue work. This research has concentrated on developing a concept prototype and research methodology of a brush-based earthquake rescue robot. The research explored the possibility that the rescue robot could predict and change its body shape to correspond to the voids according to void shape information.

The research methodology focuses on the robot body shape altering mechanism and a searching algorithm to find an optimum body shape from a robot body shape information database. A robot body component prototype has been produced for laboratory experiments and to test the research methodology. Bristle traction force theory is discussed including mathematical modelling. The interaction between the robot body brush unit and the void wall is investigated to help the robot brush unit design in the future.

1.5 THESIS CONTRIBUTIONS

This thesis presents the concept design of a brush-based, shape reconfigurable, robot for earthquake rescue. This work sits within a general research activity in Durham relating to bristle based robots. At this point it is useful to identify the specific contributions made by the present author. The research work described in this thesis has made a number of significant contributions, which are as follows:

- The robot body shape change mechanism and its algorithm were developed to enable the rescue robot to change its body shape intelligently, to enable it to negotiate changes of void shape.
- A simulation of the robot body shape change algorithm was conducted and the simulation results show that the algorithm is feasible.
- A void shape sensor, based on a strain gauge system, was developed and used to detect void shapes in a number of robot body shape change experiments.
- A control system, including software and hardware for the robot body shape change device was developed and subsequently investigated in a number of robot

body shape change experiments. The experiments showed that the control system was effective.

- A set of programs, written in the C language, were used to automatically acquire and manipulate coordinate data of robot body shape control.
- Traction experiments were carried out to investigate the traction performance for different robot body shapes. The interaction between the robot body shape and the void shape and the bristle behaviour were investigated and analysed, using Euler buckling theory.
- A mathematical model of bristle traction force was set up and tested by conducting a simulation of reverse traction force of one single bristle. The simulation results matched the results of practical traction experiments.
- Five papers, based on the research described in this thesis, have been published in international journals and at an international conference.

CHAPTER 2

RESCUE ROBOTS

This chapter introduces the current development of Urban Search and Rescue Robots (USAR) around the world and the high challenge of doing research in this field. Several USAR robots are introduced and serve as representatives of recent outcomes in this newly developing area. Following the investigation of these robots, a discussion is given to clarify the deficiencies of such robots. Further discussions describe and compare a brush based pipe crawling robot developed by the University of Durham. Pipe crawling robots used in pipeline maintenance are also introduced and compared with the brush based pipe crawling robot. The design characteristics of a new brush-based rescue robot are described towards the end of the chapter. The robot design is characterized to fulfil the practical potential demand of rescue against the background of investigation of current USAR robot deficiencies.

2.1 URBAN SEARCH AND RESCUE ROBOTS

Earthquakes are unfortunately frequent happenings and are very dangerous natural phenomena. In almost every major earthquake, many victims are buried under collapsed buildings, bridges, roadways, etc. It is very difficult to rescue these people,

who may well be injured, hungry and weak. In addition, the structural conditions under the rubble can be complex, dangerous and unknown. So, there is a primary need to explore these conditions and determine the victims' locations and their condition without compromising the rescuer's safety.

Disasters involving structural collapse of buildings routinely inspire sympathy not only for victims and their families but also for the heroic rescue personnel, who are faced with a tremendously complex, hazardous, and often frustrating tasks and environment. Rescue activities in the aftermath of earthquakes and bombings indicate a need for safer access to dangerous areas within any sites involving collapsed structures. So, robotic systems for Urban Search and Rescue (USAR) have become an important research field.

2.1.1 "RoboCup Rescue"

Lessons learned from the Kobe, Turkey and Taiwan earthquakes include the serious need for robust, dynamic, intelligent planning systems for search-and-rescue operations and for powerful telephonic systems, including robots and digital assistants, to cope with the varied and changing situations. The scale of the disaster and the speed at which the system must change is far beyond human-based mission planning and results in extremely hostile conditions that make human search and rescue dangerous.

"RoboCup Rescue" was launched as a challenge project for the AI, multi-agent systems, and robotics communities. The aim of "RoboCup Rescue" is to develop a

series of technologies that can actually save people in the case of large-scale disasters and to enable such systems to operate on a worldwide basis. (Kitano H. et al, 2001)

"RoboCup Rescue" consists of four major projects:

(1) Simulation,

(2) Robotics and infrastructure,

(3) Integration,

(4) Operation.

The "simulation" project involves developing comprehensive disaster-rescue simulation systems that can evolve into deployable, real-time, decision-support systems. Such simulations could be used to investigate the best search-and-rescue strategies using autonomous and non-autonomous rescue agents. The "robotics and infrastructure" development project should directly and significantly improve search-and-rescue operations in real disasters by providing the rescue agents themselves. The "integration" project involves integrating the comprehensive simulation system, robotics and digital assistant systems for eventual, full-scale deployment. Thus, the "operation" project involves a stepwise deployment of the system in the real world.

2.1.2 Miniature robots for USAR (Urban Search and Rescue)

The use of miniature robots for Urban Search and Rescue (USAR) was first proposed to the Federal Emergency Management Agency (FEMA), U.S., in the aftermath of the Oklahoma City bombing (Blitch, J., 1994). Earlier consideration of mobile robots for USAR work involved systems, which were too bulky and unreliable for employment in structural collapse situations. However, a recent review of developments in mobile robot technology revealed that a variety of small, lightweight

and remarkably robust micro-rover systems have become commercially available for application to the challenging USAR task domain. (Mills, C. et al, 1995)

Practical experience in actual employment of these systems for search and rescue operations is virtually non-existent. The closest pool of related expertise is most probably found in the power production and management industry, where various micro-rover platforms are used for remote inspection of containment vessels and processing systems.

The primary advantages realized, through employment of micro robots as search assets, are explored in a paper by Blitch (Blitch, J., 1996). To summarize this paper, small robotic platforms are valuable to the USAR community mainly because they can provide access to areas otherwise denied to human and canine searchers, due to the confined space, structural instability, or the presence of hazardous materials. These small robotic platforms achieved their applicability as a result of a reduced footprint, hazard immunity, and flexibility of design. Some robots are logistically self-sufficient, and easy to transport to reposition within a crisis site. When combined with the usual robot advantages of 24 hours operation, relative immunity to fatigue and multiple sensors, micro robot systems can have a tremendous affect on the entire USAR capability. Even after survivors are located, micro robots can perform critical assistance tasks by returning to an entry point and towing tubes and microphones to survivors, in order to provide support, which can be in the form of air, water, medicine, food and communications. Such contact can have a tremendous effect on a survivor's will to live and their ability to convey critical information about other victims or crisis site characteristics. (Blitch, J., 1996)

The emergence of new technology in the form of remote inspection platforms has created a variety of small robots capable of providing extensive survey coverage of difficult or dangerous areas. The primary motivation for this technology comes from the need to inspect for nuclear containment but it has also allowed technology transfer to several related areas, such as NASA's Mars and Lunar rover programs. As a consequence, several families of micro robots are now commercially available. Figure 2.1 shows a miniature robot made by Inuktun Services Ltd, which has been given the name "MICRO VGTV".

2.1.2.1 Miniature robot "MICRO VGTV"

The Micro Variable Geometry Tracked Vehicle is a compact, durable, remotely powered and controlled video inspection system, capable of negotiating obstacles. The custom Micro VGTV can be built to order, incorporating features such as bi-directional audio and remote sensing. As the name implies, the vehicle's shape can be altered during its operation. The tracks, in their lowered configuration, take the shape of a conventional crawler unit. If the geometry is varied to the point where the vehicle is in its raised configuration, the tracks take the shape of a triangle. The Micro VGTV remains operational throughout these alterations and as a result can continue to travel and manoeuvre while its configuration is being changed. By combining the camera tilt function and the steering capability, the vehicle operates effectively as a remote mobile pan and tilt camera. A hand held control unit provides a joystick for speed and direction and separate controls for the shape change, variable lights and camera tilt. The robot can travel at a speed up to 15 feet (4.57m) per minute. The

maximum tilt angle of its CCD camera is 300 degree. Its tethered cable is 30m long and has an abrasion resistant jacket. Two 20W lights are attached to the robot for illumination. The robot can operate in a temperature range from 0° — 50°C. The robot in its lowered configuration is 12.5in (317.5mm) long, 6.5in (165mm) wide and 2.5in (63.5mm) high. The robot in its raised configuration is 7.5in (190.5mm) long, 6.5in (165mm) wide and 10in (253.9mm) high.

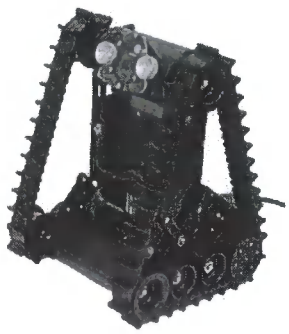

Figure 2.1: A miniature robot "MICRO VGTV"

2.1.2.2 Robot produced by IS Robotics

The IS Robotics robot was developed to aid military operations in urban terrain (Matthies, L. et al, 2000). Currently, it is a prototype under development; the robot is designed for durability and versatility. It features robust systems and onboard data processing capabilities that will enable rapid response to a dynamic, urban environment. Its portable size and ability to endure adverse conditions will make it ideal for aiding soldiers in overt and covert operations and for venturing into areas that are hazardous or inaccessible to humans. The robot is designed to operate on the principle of supervised autonomy, which allows the robot to perform autonomously or under remote supervision. This reduces the attention required from operators, letting

them maintain situational awareness while monitoring the robot. The robot dimensions are 7.14in (181.4mm) high, 16in (406.4mm) wide and 34.5in (876.3mm) long, with flippers fully extended. It weighs 40 pounds (18.1kg) and is waterproof up to 3 meters depth. Its nominal speed is 2.2m/s. Three DC motors are used to drive the robot and two pack batteries mounted on the robot are used as its power supply. Its self-righting mobility platform is equipped with tracked flippers that allow the robot to climb hills and stairs. The robot was equipped with cameras, microphones, sonar, infrared sensors and laser scanners to enable it to respond to environmental stimuli.

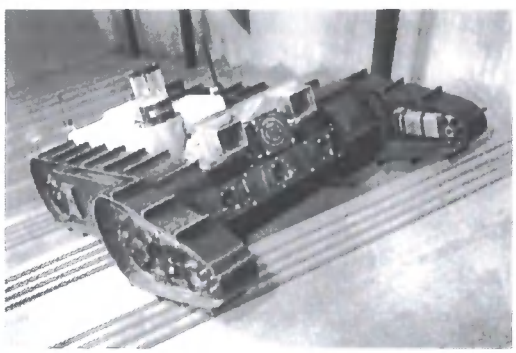

Figure 2.2: A miniature robot produced by IS Robotics

2.1.2.3 Rovver 900

Figure 2.3 shows a miniature robot called Rovver 900 made by Everest VIT. The Everest VIT Rovver 900 is a high-powered crawler that can inspect pipes with diameters from 9in to 60in (228.6mm to 1524.9mm) at distances up to 600 feet (182.9m). Using a hand-held remote pendant, the operator can steer the crawler over debris and around multiple elbows. The remote pendant also controls the crawler's focus, lighting and speed. The crawler is equipped with a high resolution colour CCD camera to carry out the inspection. The crawler's pendant-controlled lift platform

provides sweeping inspections by raising and lowering the camera as the crawler moves through the pipe. A remotely operated clutch can release the crawler's wheels allowing the operator to pull the crawler back in a freewheeling mode. The system's automatic motorized cable reel senses the crawler's movement and automatically reels it in or out of pipes. The Rovver 900 carries a pan-and-tilt, forward-viewing colour camera as well as sensing or sampling equipment. The Rovver 900 weighs 23 kg and is portable and light enough for one person to conduct inspections. It is waterproof for humid, damp and underwater environments. It has the dimensions 21in (533.4mm) long, 8in (203.2mm) wide and 6.5in (165.1mm) high. The Rovver 900 is driven by two 20W DC motors and is connected with a 200m long cable.

Figure 2.3: A miniature robot Rovver 900

2.1.3 A CUL robot

In a paper by Tokuda (Tokuda K. et al, 1999), a prototype robot known as CUL (Carry and power assist robot for Unspecified Landform) has been described, see Figure 2.4. The robot was developed for earthquake rescue missions and takes the form of a walking robot, which can carry rescue tools and assist a rescue team. The robot consists of a stereo-vision system, two legs and two wheels. The robot watches

the human who goes ahead in the damaged environment. The robot can follow the human and, in this manner, the robot learns the safe places and routes. When the robot arrives at the rescue area, it can be used as a master-slave or power-assist system. To realize a system with such functions, Tokuda has proposed a method for creating a safe environmental map. The method has been given the name Mold Tube Method. A Mold Tube is generated by watching the operator walking just in front of the CUL robot using the robot's stereo-vision system. More detail of the Mold Tube Method is described in the paper (Tokuda K. et al, 1999). A feasibility study has been carried out and results of experiments are discussed in the paper. The experimental results show the effectiveness of the CUL rescue robot.

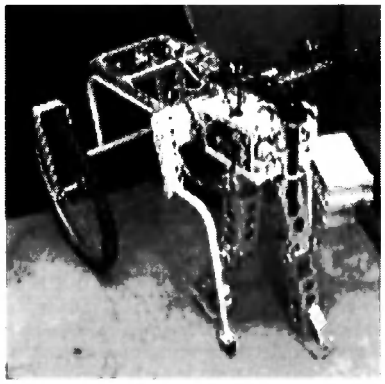

Figure 2.4: A CUL robot

2.1.4 A rescue robot with multi-sensor control system

As illustrated in Figure 2.5, a rescue robot model with a multi-sensor control system has been built by Masuda, et al in Tokai University (Masuda et al, 1996). The robot is controlled by a human operator but it is designed to be able to grasp the human arm and pull the body. The paper indicates that the functions of the rescue robot can be divided into three tasks:

(1) Find a victim and move adjacent to it.

(2) Eliminate obstacles and excavate the victim.

(3) Directly grasp a part of the victim's body and carry the victim to safety.

Among these three functions, the most difficult one to realise is the "direct grasping" of a human body. Thus, the paper focuses on point (3). For rescue work, direct contact with a human body is an objective operation. When a robot grasps any part of a human body it is absolutely necessary that it should work without causing any harm, pain or discomfort. So, there are many problems in the control of the "helping hand", such as, how and where to grasp and what force is necessary. To grasp a part of the human body in a proper manner but not cause any harm, flexibility of the hand mechanism and a multi-sensor system are necessary. The trial rescue robot model, described in the paper, provides a transport mechanism, an arm and a hand mechanism. The multi-sensor system is used to recognize the position of the human body to decide how and where to grasp the body without hurting it. The hand of the robot is equipped with distributed tactile sensors for detecting the state of the grasped object. A force sensor is used for detecting the force or torque on the wrist and a slip sensor for detecting relative motion of the grasped object in the hand. A multi-sensor processing system for fusing this sensor information is built into this robot model. In the experiments, using a dummy, this robot model worked effectively. This is only one step towards realising the direct grasping of a real human arm. For the use of this robot in the real world, the power of the actuators, the assurance of absolute safety and protection from the hazardous environment need to be considered. The system also needs to provide adaptability to the environment and be able to withstand the harsh physical conditions.

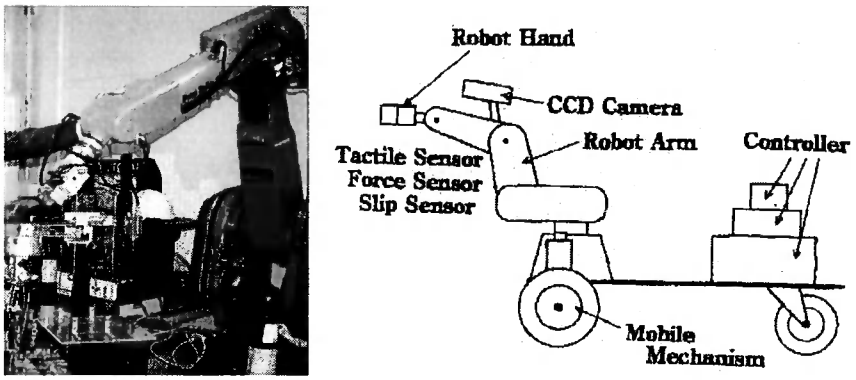

Figure 2.5: A rescue robot with multi-sensor control system

2.1.5 Gap creeping robot

A gap creeping robot was built and described by Tonoike etc. (Tonoike A., 1998). It can move through gaps in a collapsed building caused by an earthquake. It uses an air-pressure drive and a multiple-segment body-movement mechanism. The device combines air jacks and solenoid valves. A computer controls the solenoid valves to regulate the air pressure of the air jacks and to make the robot move. Figure 2.6 shows a schematic illustration of the robot.

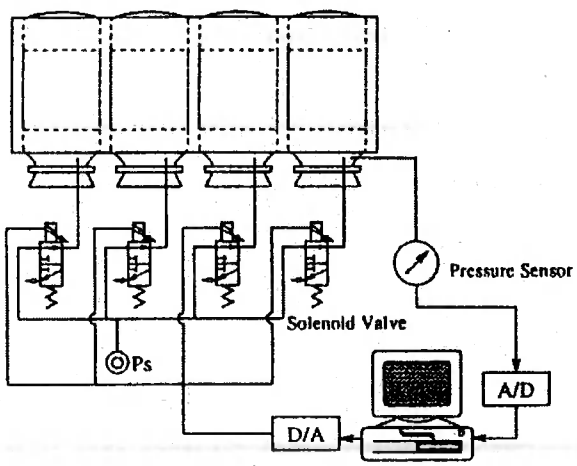

Figure 2.6: Schematic illustration of a gap creeping robot

Figure 2.7 shows the working principle of an air jack. In the figure, the left part shows the plan view of the air jack and the right part shows the cross section view of air jack. The air jack shape is flat when it is deflated. When the air jack is filled with air and becomes inflated, the height of air jack will increase. However, the width of air jack will decrease. The gap creeping robot utilizes this working principle to move through gap.

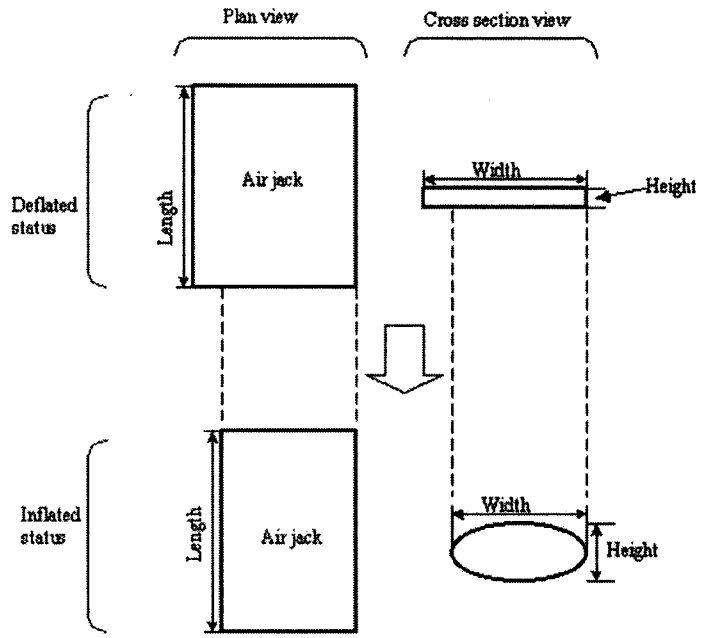

Figure 2.7: The working principle of air jack

Figure 2.8 illustrates how the robot controls the air pressure of the air jacks and conducts one working cycle. The figure shows the cross section view of a gap creeping robot, which is composed of four numbered (1-4) air jacks. The figure also indicates how the robot moves through a gap formed by two parallel coarse surfaces. The robot moves in a direction towards the right in the figure. The whole working cycle includes seven stages, which is expressed as a sequence a, b, c,…, g.

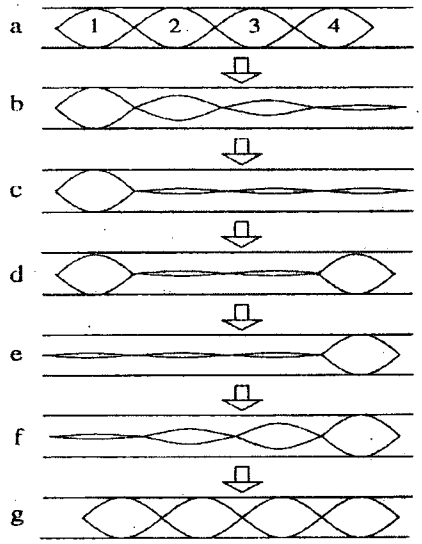

Figure 2.8: A conception diagram of a gap creeping robot

Stage a is the start of the cycle and the gap creeping robot is positioned between two coarse surfaces. All four air jacks are inflated. In the following stages b and c, the air in jacks 2, 3 and 4 is vented and the three jacks become deflated. Air jack 1 remains inflated but motionless because of the friction force between the air jack skin and the gap surfaces. Consequently, the widths of the jacks 2, 3 and 4 increase. Thus, the whole robot's width becomes wider compared to stage a. At stage d, air jack 4 is refilled with air and becomes inflated again. Thus, both air jack 1 and air jack 4 are motionless because of the friction force. In the following stage e, air jack 1 is vented but jack 4 still remains inflated and motionless. So, the combined width of air jacks 1, 2 and 3 become wider and thus these three air jacks have moved forward incrementally. Now air jack 4 is further to the right than it was at stage a. In stages f and g, all of the air jacks are progressively refilled with air, progressively moving air jacks 3, 2 and 1 along the gap. The robot is now ready for the next working cycle. A gap creeping robot with a length 675mm and a width 300mm can theoretically move 50mm in a single working cycle.

2.1.6 Snake robot for search and rescue

Choset (Choset H., 1996) made a serpentine robot, which can be used to search voids and locate victims, as illustrated in Figure 2.9. The serpentine mechanism used by this robot has many more degrees of freedom than conventional robots and rescue machinery. It also has the advantage of a small cross-sectional area. These many degrees of freedom enable the hyper-redundant mechanism to thread through tightly packed obstacles, reaching locations otherwise inaccessible to conventional robots, while not disturbing the surrounding areas. This is critical in search and rescue operations where large pieces of debris form fragile, makeshift support structures. A camera and a small mechanical hand are installed on the robot head. These can be used for observing environmental conditions at the rescue location and for handling some small items. The robot has several joints, which make it move freely and agilely. A video on web page:

(http://voronoi.sbp.ri.cmu.edu/projects/prj_search_rescue.html)

shows clearly how the robot works. However, this snake robot is actually a multi-degree of freedom mechanical arm, which cannot travel through the environment because its base is fixed. The control panel and monitor are connected to this base through cables, similar to a conventional fixed based robot.

Figure 2.9: A serpentine robot

2.1.7 Robug III rescue robot

Two scientists at Portsmouth University have been developing a versatile robot that was initially designed for rescue work (Luk, B., 1995). Following the nuclear disaster at Chernobyl the robotics research team was asked by the European Commission to build a rescue robot. The scientists, Prof. Gurvinder Virk and Dr. Bing Luk produced the robot, which was named Robug III. The robot was said to resemble a spider and could walk sideways like a crab and scale walls. Robug III was designed as a rescue robot to enter places that were too dangerous for humans. As illustrated in Figure 2.10, it weighs 100kg, and has eight legs with vacuum gripper feet that enable it to climb vertical, sheer walls. In addition, it is equipped with a laser scanner for measuring distances. Robug III can walk, climb over debris and even climb up sheer walls or other vertical or inclined surfaces. Whilst its primary design was for rescue, Prof. Virk and Dr Luk are also actively investigating other roles the robot can take. Several applications in industry have been suggested, including mining and scrubbing ships' hulls (Luk, B., 1995).

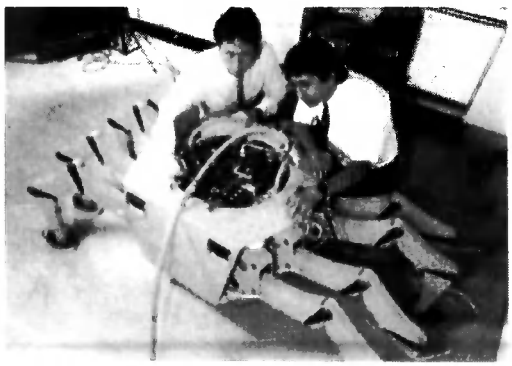

Figure 2.10: Robug III rescue robot

2.1.8 Shrimp robot

A high mobility wheeled rover named Shrimp was made by Estier (Estier T. et al, 2000). The Shrimp is a six-wheel rover. Using a rhombus configuration, the rover has a steering wheel in the front and the rear, and two wheels arranged on a bogie on each side. The front wheel has a spring suspension to guarantee optimal ground contact of all wheels at any time. The steering of the rover is realized by synchronizing the steering of the front and rear wheels and the speed difference of the bogie wheels. The use of parallel articulations for the front wheel and the bogies enables a virtual centre of rotation at the level of the wheel axis. This ensures maximum stability and climbing ability, even for very low friction coefficients between the wheel and the ground. A well functioning prototype has been designed and manufactured by Estier. The total weight of this first prototype was 3.1kg including 600g of batteries and a 1.75W DC motor powering each wheel. The overall dimensions were L 60cm × W 35cm × H 23cm and the ground clearance was 15cm. The advantage of its high mobility lies in the parallel architecture of the front fork and of the bogies. This rover is able to passively overcome unstructured obstacles of up to twice its wheel diameter and can climb stairs with steps of over 200mm. Shrimp robot shows excellent off road abilities, overcoming rocks even with a single bogie. The robot is also able to overcome obstacles with a frontal inclination of 40 degrees. Figure 2.11 shows a picture of the Shrimp robot.

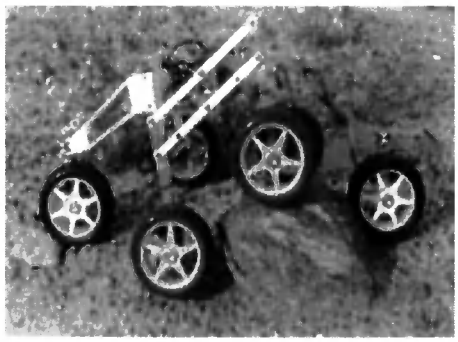

Figure 2.11: Shrimp robot

2.2 DISCUSSION OF CURRENT RESCUE ROBOTS

From the descriptions of different kinds of rescue robots above, it is obvious that they are vulnerable in a number of ways, are designed for special purposes or can only work in restricted environments. Miniature robots are attractively simple but unable to carry heavy rescue materials because of their small size and limited power. These miniature robots can usually work on the surface of debris. However, it is not practical for them to work in voids under the debris. The CUL robot cannot work in small voids under the debris and is not even suitable for working on rugged debris because of its wheel mechanism. At this stage, it is only a laboratory prototype and needs an operator walking ahead of the robot in order to obtain a mold tube, which is actually a non-obstacle path explored by the operator. Such a prerequisite puts the operator directly in the danger, which is undesirable. So, it is hard to understand how this approach can reduce the dangers faced by a rescue team and work in a practical rescue site.

A gap creeping robot is intended to be used to move obstacles blocking the path to victims. After buildings collapse in an earthquake, collapsed debris piles

together and forms narrow voids. Victims are often buried in these voids. These voids can be located under the ground or inside the piles of debris. The gap creeping robot may need to go through a very complicated path to reach the victim. However, it is unable to move further once its path is blocked. Gap creeping robots move much slower than other robots because of its working mechanism. Although in his paper Tonoike claims that the gap creeping robot may work in some environments with dangerous explosive gas and without electric power supply, he did not give an explanation. The moving energy of the gap creeping robot is from compressed air and the switching of gas power needs a controller, which normally is electrical. So, it needs to be external to the site or sealed to make it safe. In addition, the gap creeping robot can only move through a gap of limited size but not a large gap or voids of other shapes.

The snake robot made by Choset is good at transporting items to a point of need but basically, in practice, it is only an articulated machine arm. One end of the arm is fixed on a base and so this limits its working range. The maximum working range, which can be reached by the robot, is limited by the length of the arm. The robot also requires necessary space to conduct operations such as withdrawing the arm.

It seems that most robots described above cannot, as yet, carry out any rescue work in a practical environment, particularly when it is required to rescue victims buried in voids. Rescue robot design is a newly developing field and there are few developed robots to fit the practical requirement. As a result, this thesis focuses on the research of a new rescue robot based on previous pipe tractor research work at the

University of Durham. Research in this area has given the author some insight and experience. Thus, it is useful to review the development of this branch of robotics at this point.

2.3 PIPELINE ROBOTS

The international pipeline population is growing in age and some installations have already been in operation beyond the service life for which they had originally been designed. Inspection of pipes is an important task faced by many industries. The deterioration of the inner surface of pipes is especially common in refineries and steam plant. It is therefore of increasing importance that pipeline operators are provided with the means to accurately and reliably inspect their pipelines and obtain the information needed for decision-making regarding safe operation, rehabilitation and repair (Beller, M. et al, 1998). The concept of automatic pipe inspection could reduce the downtime and manpower required for pipe inspection processes. As a consequence of these demanding applications, many kinds of pipeline robots have been developed.

2.3.1 A cleaning pig

Adachi, Y. et al developed a cleaning robot shown in Figure 2.12 in order to reduce underwater pipe cleaning work, which is carried out by a diver (Adachi, Y. et al, 1998). This robot consists of a main body, a rotational arm and a driving arm, which is used to move the robot in a pipe. At the end of the rotational arm, a cleaning head is mounted, and the cleaning of a pipe is carried out by means of rotating the

rotational arm pushing this head to the pipe wall. The rotational and driving arm is able to expand and contact the internal pipe wall by using an air cylinder. The maximum travel speed of the robot is 1m/minute. The robot can work under the water up to 30m deep. The cleaning performance of this robot is about $100m^2/hr$, which is about five times faster than a diver. Furthermore, the cleaning robot is not influenced by the biology of material adhering to the pipe wall. The paper gives the results of experiments on cleaning work on an actual inlet pipe of a power plant.

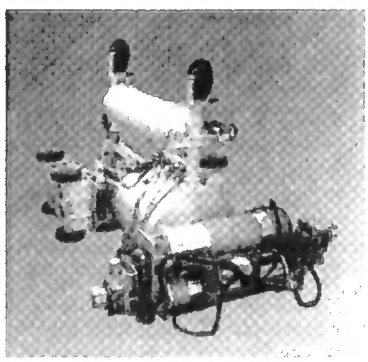

Figure 2.12: A cleaning pig (Adachi, Y. et al, 1998)

2.3.2 Inspection and measurement pipe robots

2.3.2.1 An automatic pipe inspection robot

Glen and Devon (Glen, B. et al, 1997) describe a robot that is used for automated pipe inspection. The propulsion of the mobile robot was achieved by two tractor drives mounted on separate limbs located at 180 degrees with respect to each other. The aluminium limbs were attached to the tractor drives by means of flexible couplings. The robot communication and control was achieved by an IBM compatible off-board computer through a standard parallel port. Pipe surface defects are detected by means of sensors mounted on spring-loaded fingers. These sensors consist of a mechanical lever and an electronic micro-switch. The micro-switch is spring-loaded

and pushes outwards against the inner surface of the pipe. Should the robot encounter a defect, the lever activates the micro-switch and, by means of necessary signal conditioning, indicates to the off-board computer that a defect has been encountered. Three defect sensors were mounted on three separate fingers at 120 degrees to each other. The advantage of this system is that it utilizes established mechatronic principles to produce a low-cost device capable of detecting inner pipe defects such as the deterioration of the inner surface of pipes. Once the robot located the defect, the extent or depth of the defect could then be determined using more advanced detection techniques. The paper stated that the robot proved to be reliable and accurate over short sections of pipe and provided adequate information on the location of the defect.

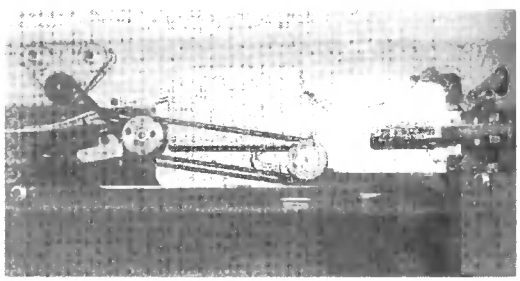

Figure 2.13: An automatic pipe inspection robot (Glen, B. et al, 1997)

2.3.2.2 An internal pipe inspection robot

An internal pipe inspection robot is described in a paper by Kawaguchi (Kawaguchi, Y. et al, 1995). The inspection robot can overcome limitations placed on normal inspection robots, which cannot turn in a T-shaped pipe or move through a plug valve. The new mechanism proposed in the paper is based on dual magnetic wheels, which not only overcomes the limitations mentioned above but also enables the robot to climb over sharp obstacles like sleeves joints. The research described in the paper focuses on discussing another drawback of earlier robots, that is, the friction

between the pipe and umbilical cables used for communication and power supply, which may extend over long distances. A fibre optic communication system was designed to reduce the friction. A compact visual inspection system to inspect welded sections of the pipe was developed and mounted on the head of the robot.

2.3.2.3 KARO pipe inspection robot

Kuntze and Haffner (Kuntze H. et al, 1998) developed a robot system named KARO (Entwicklung eines flexible einsetzbaren Robots zur intelligenten sensor-basierten Kanalinspektion), which is equipped with intelligent sensors. These allow automatic and reliable detection of damage location, type, size and give superior performance compared with the majority of CCTV-based (Closed Circuit Tele Vision) systems. It was developed for the protection of ground water and soil against contaminating materials and liquids. The concept of the KARO system consists of a mobile control and surveillance station and a mobile robot. The robot motion and sensor functional units are controlled and monitored by the operator within the mobile control and surveillance station. The KARO robot has a length of 800mm and a diameter size, which is suitable for sewer pipes with an internal diameter of 200mm. The range of travel is approximately 400 meters. For the automatic detection and classification of damage, the robot is equipped with several sensors. It consists of an optical sensor in a pan-and-tilt head and ultrasonic sensors in the head and in the belly of the vehicle. The optical sensor is mainly used for the detection and measurement of deformation, obstacles and cracks inside the pipe. Two air ultrasonic sensors within the pan-and-tilt head provide early information on obstacles that lie ahead. They also provide data on pipe deformation as well as coarse cracks.

2.3.2.4 An underwater pipe inspection robot

An underwater robot for pipe inspection was proposed by Bradbeer (Bradbeer R. et al, 1997). It is a submersible autonomous and intelligent remote operating robot that consists of a variable buoyancy body shell fitted with both propellers and legs to provide mobility within the confined space of water filled tunnels, drain pipes, and sewage outfalls having a diameter of 900mm or greater. The robot is aimed at the inspection and maintenance service industry. Initially, the pipe robot will carry a video camera with lighting. It is proposed that communication could be achieved via an ultrasonic link, eliminating the need for a cable. In situations where such a link is not feasible, fibre optic communications is proposed as a backup communication method. The robot is capable of propelling itself, along the pipe to reach the inspection point. It can either walk along the bottom of the pipe, or, if there is debris and residue on the bottom, float up above the obstacles. Meanwhile, cameras transmit real-time images of the tunnel surface. An optional ultrasonic scanner can provide a 360 degrees profile of the pipe surface. This combination of sensors enables an operator to inspect the pipe's condition and also immediately know the robot's location. As the pipe robot is intelligent, with multiple back-up systems, it can automatically recover from potentially terminal situations, such as power loss or communications breakdown.

2.3.2.5 A micro inspection pipe robot

Miyagawa et al (Miyagawa, T., et al, 1999) developed a micro-inspection robot for 1-inch diameter pipe. It can undertake visual inspection inside pipes and also retrieve small objects. The robot is only 110mm long, has an external diameter of

23mm, and weighs 16g. It is equipped with a high-quality micro CCD camera. It also has a two-digit hand for manipulating small objects. The robot is propelled by micro electro magnetic motors. The wheels, which are driven by a system of planetary reduction gears and worm gears, press against the pipe wall and enable the robot to travel, even within vertical and curved pipes. The robot travels at a speed of about 6mm/s and the pulling force is approximately 1N. The development of this micro robot used various micro technologies, including micro actuators, micro reduction gears, micro robotic hands, and a micro CCD camera. The camera mounted on the robot provides high-resolution images to an external monitor and is only 7mm in diameter and 12mm in length. Using the camera, an operator can observe down to 25μm on the pipe inner surface.

2.4 DISCUSSION OF PIPELINE ROBOT RESEARCH

Most of the robots described above are in fact tele-operated mobile robots. For example, KARO is controlled and communicates with a surveillance station through a cable. The robot made by Miyagawa is operated by a control unit, which communicates through optical fibres, which are used to reduce the friction force between the cable and the pipe wall. Autonomous robots are normally equipped with a microprocessor, which can process the robot control, collect data, and deal with signal processing and communication. These robots have limited automatic functions including automatic positioning, sensing, etc. Operators operate the robot through the communication between the robot and operator. The environment where the robot will work decides the communication media and the communication could be by wire or wireless. Wireless communication is usually realized by infrared, ultrasonic or radio.

For some inspection tasks, the robot may need a mechanical hand. For example, the micro robot mentioned above is equipped with a small mechanical hand to retrieve a tiny object in the pipe. A vision system is an important part of a mobile robot system and usually takes the form of a CCD camera. All the robots discussed above have a camera to supply an image from the inside of the pipe. In addition to a vision system, mobile robots need to be equipped with other sensors to carry out various inspection tasks. To allow automatic and reliable detection of damage location, type, and size, KARO is equipped with several intelligent sensors including an optical sensor and several ultrasonic sensors. The robots included in the review all use a wheel mechanism for their traction, although they are intend to be used in different fields and have different structures. The wheel mechanism is at a distinct disadvantage if the wall of the pipe is broken, badly damaged or the pipe is partially blocked. These robots are designed to work in a fixed diameter pipe of a sound quality.

2.5 A BRUSH-BASED ROBOT FOR EARTHQUAKE RESCUE AND PIPELINE MAINTENANCE

A pipe crawling robot has been developed in the Centre for Industrial Automation and Manufacturing (CIAM), School of Engineering, University of Durham. The robot utilises a unique, innovative and patented traction system. The principle of the drive system is simple. That is, if a brush is inserted into a pipe and its bristles are swept back at an angle, then, it is easier to push the brush forwards though the pipe than it is to pull it backwards. Thus, if two brushes are interconnected by a reciprocating cylinder, then, by cycling the cylinder, it is possible for the robot to crawl through the pipe. Aspects of the drive system have been awarded patents on a

near worldwide basis. More details about the drive system are illustrated by Stutchbury (Stutchbury, N., 1999) and Han (Han, C., 1999). Most of the robots developed in Durham are powered by pneumatics and grip the wall of the pipe by means of many bristle clusters, hence the name "brush" robot. Just like other pipeline robots mentioned earlier, a brush robot could only work in pipes within a limited diameter range although, unlike many of the other traction systems, the bristle mechanism is capable of dealing with broken or partially collapsed pipes.

2.6 SUMMARY

This thesis proposes some improvements on the developed brush robot principle and adapts the principle to work for the purpose of earthquake rescue and in severely damaged or broken pipelines. This study should also apply to traversing pipes with non-circular cross-section and varied diameters. In this work the robot is designed to be able to alter its body shape to fit the varied void shapes in a collapsed building or in different diameter pipes whose walls might be broken or in a bad condition. For the purpose of earthquake rescue, the robot could be equipped with, for example, a CO_2 detector, a microphone, a speaker, a camera and an oxygen hose, etc. In addition, a sensor system for detecting the void shape and a control system for changing the robot body shape will be necessary. The next chapter will describe the robot body shape change in detail.

CHAPTER 3

ROBOT BODY SHAPE CHANGE

This chapter focuses on robot body shape change, its control algorithm and an enabling simulation. The first part of the chapter illustrates the working principle of a brush based robot and how the bristle mechanism influences its function. The robot body shape change mechanism is described and the shape change control algorithm is illustrated. The operation to acquire the robot body shape information database is also described. Simulation has been used to investigate the feasibility of the algorithm.

3.1. INTRODUCTION

The key design characteristic for a brush robot is its ability to grip the wall surface to produce the required traction. For the purpose of earthquake rescue, the robot should be able to pass through irregular voids in the ruins made by the earthquake. So, it is desirable that the robot is able to alter its body shape to fit the void shape and produce sufficient traction force. Earlier experiments by Stutchbury (Stutchbury, N., 1999) have shown that optimum traction can be obtained if the brush bristles approach the pipe wall at a specific angle. Deviation from this angle leads to reduced traction. To realize the requirement of optimum bristle shape, it is

necessary to know the void shape and the relative position of the robot's brush core in the void. Thus, to achieve the required traction force, the robot needs to alter its body shape to match the void shape as closely as possible. The concept used in this work is to mount four linear stepper motors on a base box and join the ends of the screw rods by means of a spring steel strip, as illustrated in Figure 3.1. The stepper motors are used as actuators. The figure shows a 3D view of a robot body module. The whole robot body can be created by assembling four or more of these parts together on a single base. A steel strip was used to carry the bristles because it gave a flexible structural component that could be easily flexed to the required shapes. For this reason, the spring steel strip used to make the robot body hoop needed to be thin, elastic and provide the required stiffness but be easily deformed by the stepper motor. To detect the void shape, it is proposed to install a sensor system on the robot. The sensor provides the void shape information to a PC and after processing the information the PC makes a control command, which changes the shape of the robot body by means of the actuators. As has been indicated, the actuators are installed around the robot body. Each group of actuators is composed of four stepper motors. These actuators can change the robot body by deflecting the robot's flexible structure components. In this manner, optimum bristle shape can be realized and the required traction force may be produced.

In this procedure, a control system recognises the signals from the sensor system and responds by sending appropriate commands to the actuators. A manual control function may also be required when the robot cannot automatically recognise the void shape. To operate the robot manually and effectively see the void condition, a CCD camera can be mounted on the robot. A software system running on a PC is

also required to run data communication, signal processing, data acquisition and affect the control. More specifically, the software will be able to record the robot's travel route and the void shapes at different stages. This information will be useful to a rescue team when making a rescue plan.

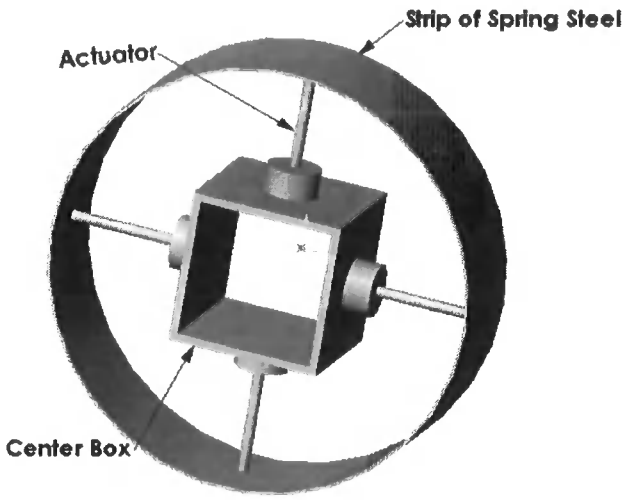

Figure 3.1: A robot body module

3.2 INVESTIGATION OF A BRUSH BASED ROBOT

The Centre for Industrial Automation and Manufacture in the University of Durham has been researching brush based tractors for many years. This research is focused on traction force for brush based tractors, bristle buckling theory and mechanical design of a brush based tractor. Some useful results have been produced giving an insight into the effect of bristle number, bristle layout, optimal angle between bristle tip and pipe wall, etc. The working principle of the brush robot is described in the work of Stutchbury (Stutchbury, N., 1999) and Han (Han, C., 1999). The following gives a brief introduction to the work.

Movement of a brush robot is achieved by the utilisation of curved bristles as the means of propulsion and support, as illustrated in Figure 3.2 (Han, C., 1999). The figure shows that two brushes are mounted at opposite ends of a reciprocating cylinder. When the cylinder opens, the leading brush, offering lower resistance because of the bristle curvature, moves forward easily. The trailing brush, because of its higher resistance to backward forces, remains stationary. However, when the reverse happens, that is, the cylinder closes, the leading brush remains stationary, whereas the trailing brush, now offering low resistance, is pulled forward.

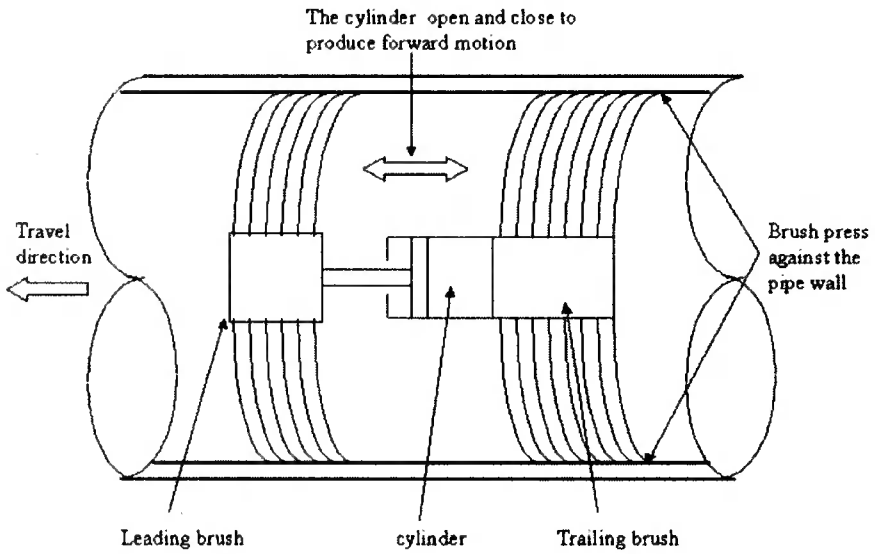

Figure 3.2: Robot brush units travel in the pipe (Han, C., 1999)

The resultant traction depends entirely on the bristle deflection mechanism, and can be illustrated in the following way. For the purpose of simplicity consider a single bristle. When a bristle is put into a pipe, its effective lateral dimension will cause the bristle to be bent by the pipe wall. This creates a normal force F_n acting at the tip of the bristle, as shown in Figure 3.3. When moving the bristle in the direction of travel, the friction force F_μ will be equal to μF_n. The projection of a bristle in the

direction of the X-axis is shown as h, the clearance between the brush core and the pipe internal surface.

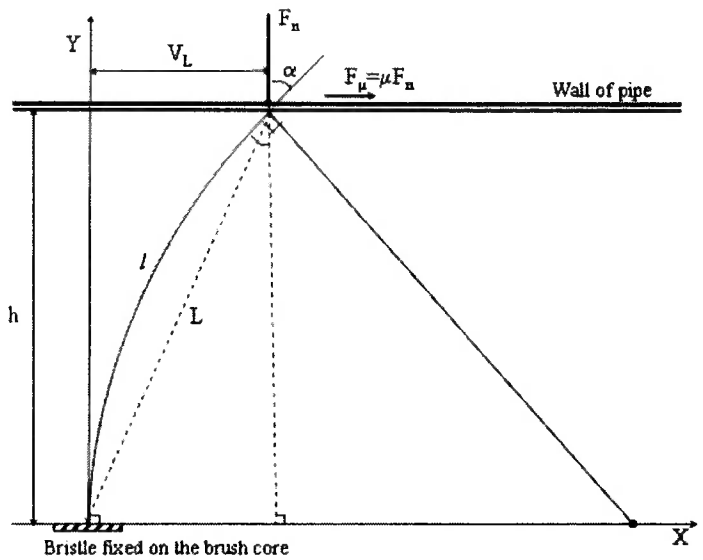

Figure 3.3: A bristle in the pipe (based on (Stutchbury, N., 1999))

Stutchbury (Stutchbury, N., 1999) gives a conclusion that the angle between the bristle and pipe wall should be between 50 and 60 degrees although this angle will vary depending upon a number of factors, for example, lubrication. Stutchbury also gives a formula (3.1) for calculating the normal force F_n at the tip of the bristle. In Figure 3.3, the bristle mounted on the brush core is assumed to have flexural stiffness EI and length l. If the friction coefficient between the bristle tip and the pipe wall is assumed to be μ, the friction force at the bristle tip will be μF_n.

$$F_n = \frac{3EIV_L^2}{l^3(l-h)} \tag{3.1}$$

Note: (h and V_L can be solved by using formula (3.2) and (3.3), which is based upon the geometry shown in Figure 3.3.

$$h = \frac{l}{\alpha} Sin(\alpha) \tag{3.2}$$

$$V_L = \frac{l}{\alpha}[1 - Cos(\alpha)] \tag{3.3}$$

V_L can also be approximately calculated by triangular geometry if the bristle is relatively straight and the chord length L can be approximate to the bristle length l.)

From the conclusion of Stutchbury, it can be shown that a bristle is able to achieve the highest friction force with an optimum angle between the bristle and pipe wall. When the bristle forms an optimum angle with the pipe wall, the projection h of the bristle in the direction of the X-axis will have an optimum value. The optimum value can be calculated by using formula (3.2) if the optimum angle and the bristle length are known. In this work, to achieve the best traction, the brush robot needs to change its body shape and try to make every bristle around its body form an optimum angle with the void wall and have an optimum projection h when the robot travels in the voids.

3.3 THE APPROACH TO ROBOT BODY SHAPE CHANGE

Figure 3.4 is a diagram of the cross section view of one robot body module. The screw rods of the four actuators are aligned along the X-axis and Y-axis, two drives to each axis. The points where the actuator screw and strip hoop are joined are numbered a, b, c, d. Points a and c can only move along the Y-axis as the actuator screw rod moves in and out. Similarly, points b and d can only move along the X-axis. By moving the actuators to different positions, the flexible body hoop can be formed to different shapes. For example, when all four actuator screw rods move in,

the strip circle can be squeezed into an approximate square illustrated in Figure 3.5. Point S_i $(i = 1,2,...,n)$ on the circle moves to its new coordinates as a result of this movement. In another arrangement, if the actuator screw rods at the X-axis are moved out and actuator screw rods at the Y-axis are moved in, the strip circle can be deflected into an ellipse (Figure 3.6(a)). If all four actuator screw rods are moved out, the strip circle can be stretched into a square (Figure 3.6(d)). If all actuator screw rods are moved in, the strip circle can be squeezed into an approximate square (Figure 3.6(c)). If all actuator screw rods are moved in but actuator screw rods at the Y-axis are moved in further than the actuator screw rods at the X-axis, the strip circle can be squeezed into an approximate rectangle (Figure 3.6(b)). The strip circle remains as a circle (Figure 3.6(e)) if the distance between two actuator screw ends in each axis is equal to the diameter of the strip circle. So, the strip circle can achieve several basic shapes with different actuator screw rod displacements. These shapes include square, approximate square, approximate rectangle, ellipse and circle as shown in Figure 3.6.

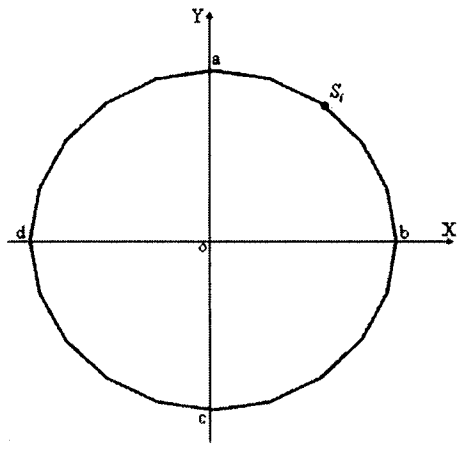

Figure 3.4: A strip hoop in an original shape

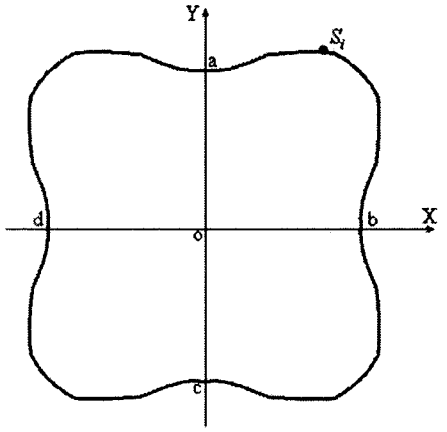

Figure 3.5: A changed strip hoop

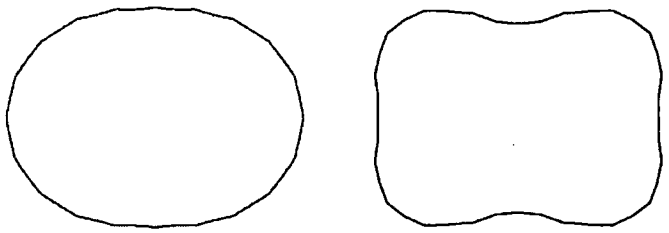

(a) Ellipse (b) Approximate rectangle

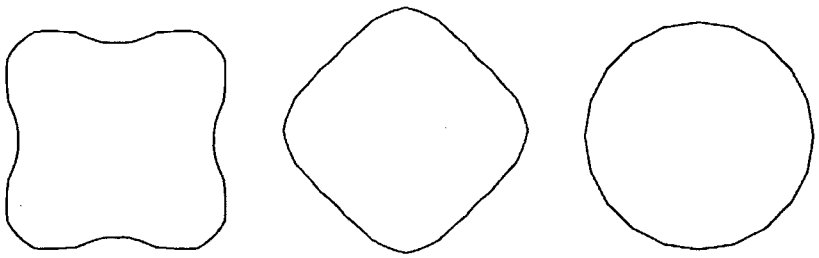

(c) Approximate square (d) Square (e) Circle

Figure 3.6: The changed hoops in different shapes

In addition to the four points defined by the actuators, other points on the strip circle can be defined as point S_i ($i = 1,2,...,n$). With the movement of the actuator screw rods, the strip circle shape is altered and correspondingly the coordinates of point S_i ($i = 1,2,...,n$) on the circle are changed. These point coordinates can be found using finite element calculation and the shape of the strip

hoop can be determined by predicting these points and connecting them to form the hoop shape. A data file can be used to store these coordinates in a specific format. Thus, a range of shapes which the strip hoop can achieve, can be expressed in such a data file. In this way data files form a database, which includes the shapes the strip hoop can achieve. To make the robot body correspond to a void, the most appropriate data file can be chosen from this database. In this work, a least square algorithm with a look-up table approach was used to search the most appropriate data file from this database and will be described in detail as follows.

3.3.1 Algorithms for robot body shape change

The coordinates of the points on the strip circle are listed, as in Table 3.1. These coordinates express a prescribed shape, as stored in the data file. A $POINT_i$ ($i = 1,2,....,n$) means the coordinates of a point on the prescribed strip hoop. $POINT_i$ is expressed by the coordinates (X_i, Y_i) ($i = 1,2,....,n$).

	$POINT_1$	$POINT_2$	...	$POINT_n$
X_i	X_1	X_2	...	X_n
Y_i	Y_1	Y_2	...	Y_n

Table 3.1: A data file expresses a prescribed strip hoop shape

Figure 3.7 shows that the prescribed strip hoop is used to correspond to a void shape. For the purpose of simplicity, using symmetry, only a quarter of the void is considered and the points on the hoop are numbered. Also, these point coordinates are listed, by way of example, in the format of Table 3.1 but in practice a data file may include coordinates of more points. For point S_1 on the hoop, a dash line starts

from the origin O and passes through point S_1 and intersects the void wall at the point P_1. Similarly, other dash lines pass through other points on the hoop and intersect the void wall at the corresponding points P_2, P_3, ... , P_n. To keep the illustration simple and clear, only three dash lines are drawn in Figure 3.7. The coordinate (x_i, y_i) is the coordinate of the point P_i $(i = 1,2,...,n)$ on the void wall.

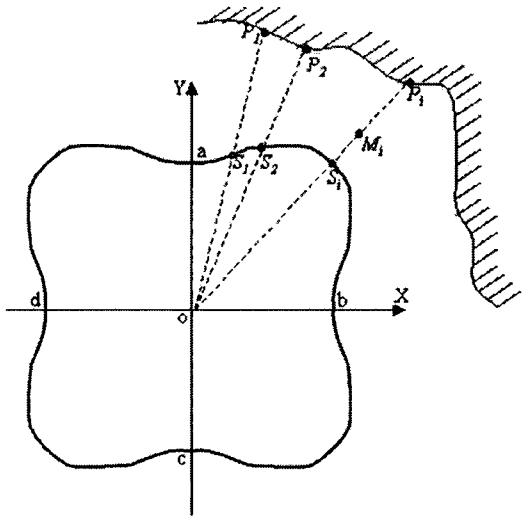

Figure 3.7: The difference between the void wall and the strip hoop

The expression $\sqrt{x_i^2 + y_i^2} - \sqrt{X_i^2 + Y_i^2}$ is the distance between a point S_i $(i = 1,2,...,n)$ on the strip hoop and its corresponding target point P_i $(i = 1,2,...,n)$ on the void wall in the same direction.

$$S_i P_i = \sqrt{x_i^2 + y_i^2} - \sqrt{X_i^2 + Y_i^2} \quad (i = 1,2,...,n) \tag{3.4}$$

The distance $S_i M_i$ $(i = 1,2,\Lambda\ ,n)$ is equal to l_{opt}, which is the optimum projection of a bristle in this direction, that is, the bristle should reach the void wall at an optimum angle and have a length l.

$$S_i M_i = l_{opt} \quad (i = 1,2,...,n) \tag{3.5}$$

The distance between point P_i $(i = 1,2,...,n)$ and the end of the bristle projection l_{opt} is $M_i P_i$ $(i = 1,2,...,n)$.

$$M_iP_i = \sqrt{x_i^2 + y_i^2} - \sqrt{X_i^2 + Y_i^2} - l_{opt} \quad (i = 1,2,...,n) \tag{3.6}$$

To make the strip hoop fit the void wall, the distance M_iP_i $(i = 1,2,...,n)$ needs to be as small as possible. That means that the sum D of squared distance M_iP_i $(i = 1,2,...,n)$ needs to be as small as possible. Thus, what is needed is to search a coordinate data file that minimizes D by the use of a Least Square algorithm. The formula (3.7) is used to calculate D.

$$D = \sum_{i=1}^{n} [M_iP_i]^2 = \sum_{i=1}^{n} [\sqrt{x_i^2 + y_i^2} - \sqrt{X_i^2 + Y_i^2} - l_{opt}]^2 \tag{3.7}$$

Thus, the data file that minimizes D is the most appropriate file. The data file represents the desired strip hoop shape, which is the most similar to the void shape among all the data files. In this way the data file gives information on how to move the actuator screw rods to achieve the desired shape of the strip hoop. For example, when the strip hoop shape is changed from Figure 3.4 to Figure 3.5, displacements of the four points a, b, c, d along the X-axis and Y-axis, equal the displacements that the four actuator screw rods need to move in the direction of the X-axis and Y-axis. If these four screw rods move the same displacements as the data file suggests, other points on the strip hoop will also suffer a displacement following the data file. Thus, the strip hoop becomes the most appropriate shape, as suggested by the data file.

3.3.2 Acquisition of coordinate data

A prerequisite for the above algorithm is to set up the data file database, which includes a group of coordinate data files in the format of Table 3.1. In each data file, the coordinates of those points on the strip hoop are recorded corresponding to actuator screw rod displacements. To acquire the coordinates of these points, a

finite element method was used. To create a database composed of such data files, many finite element calculation runs needed to be completed. This procedure involved considerable work and time. ABAQUS was chosen to do the finite element calculation. The following section introduces how this calculation was carried out.

(1) Introduction to the use of beam element

Beam element is the one-dimensional approximation of a three-dimensional continuum. The reduction in dimensionality is a direct result of slenderness assumptions. That is, the dimensions of the cross-section are small compared to typical dimensions along the axis of the beam. In ABAQUS, a beam element is a one-dimensional line element in three-dimensional space.

The main advantage of beam elements is that they are geometrically simple and have few degrees of freedom. To make the problem simple, a beam element was chosen to conduct the finite element analysis in this work. The details of how to choose an appropriate element can be found in the ABAQUS manual. (ABAQUS/Standard User's Manual, Version 5.6, 1996)

(2) Finite element calculation using ABAQUS

As shown in Figure 3.1, the robot body module is a spring steel strip hoop. If the four actuator screw rods move in and out along the X-axis and Y-axis, it is equivalent to four forces acting on the strip hoop independently as shown in Figure 3.8. Four forces F_x, F_y, F_z and F_w are applied to the spring steel strip hoop in the direction of positive X-axis, negative X-axis, positive Y-axis and negative Y-axis.

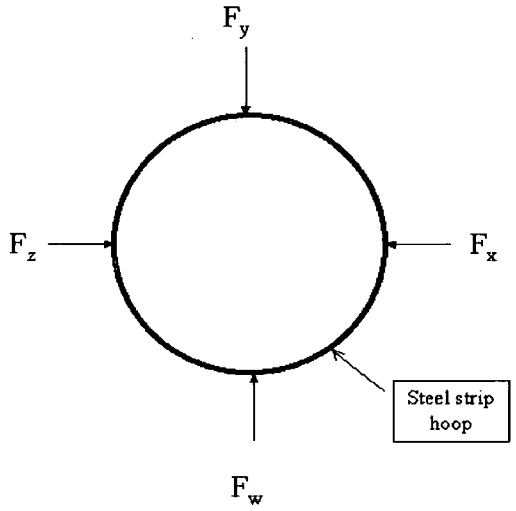

Figure 3.8: Forces acting on the strip hoop

As described earlier, these forces can change the strip hoop shape to form approximate square, rectangle, circle and ellipse shapes. The shape produced is determined by different values of the applied forces. The spring steel strip is thin and its cross section is small, so a beam element was chosen to build the finite element model. In this analysis, a quarter of strip hoop was used to conduct the finite element calculation because of the symmetry of the hoop. When the strip hoop alters its shape, nodes on the hoop move correspondingly and the node coordinates change. To record the altered strip hoop shape, these node coordinates were recorded and stored in a data file. ABAQUS post processing can deal with this task. Using different forces causes the strip hoop to change to different shapes and each shape corresponds to a unique data file. In this work, about two hundred computations needed to be done and the equivalent number of data files were created. After every computation, the values of the loading forces were reset by an increment and a new input file was created for the computation. ABAQUS/Standard and ABAQUS post processing needed to be rerun with each new input file. These operations involve considerable work, because for every analysis a new input file was manually created and the

ABAQUS post processing was run to record node coordinates in a data file and to output the file. Programs were written in C, ABAQUS commands, and Unix commands to execute these operations automatically and reduce the work involved. These programs are listed in the appendix and include *beginnew*, *new*, *myd.c*, *tempforce.dat*, *mylast*, *myunix, myrpt, origin.inp, w1.jnl* and *mydata1.c.* The diagram in Figure 3.9 helps to illustrate how these programs use ABAQUS to do the finite element analysis automatically. A group of coordinate data files of changed strip hoop shapes under different loading forces can be acquired, using these programs.

The programs *beginnew* and *new* start a new analysis session. Program *myd.c* resets the value of loading forces and creates a new ABAQUS data input file. File *tempforce.dat* stores all the values of loading forces, which will be used by program *myd.c.* Program *mylast* and *myunix* can detect whether the ABAQUS/Standard session is completed or not. Program *myrpt* can detect whether the ABAQUS post processing session is finished or not. File *origin.inp* is a template for ABAQUS input files and is used to produce a new data input file for each new computation session. In this data input file, the value of loading force is changed according to records in the file *tempforce.dat.* File *w1.jnl* is composed of ABAQUS commands, which acquire node coordinates after the strip hoop shape is changed. File *mydata1.c* processes the node coordinates data file format after all ABAQUS computation sessions are completed. All analysis sessions can be run automatically and node coordinates data files can be automatically created and converted into a specific format, which can be understood by the robot control software system.

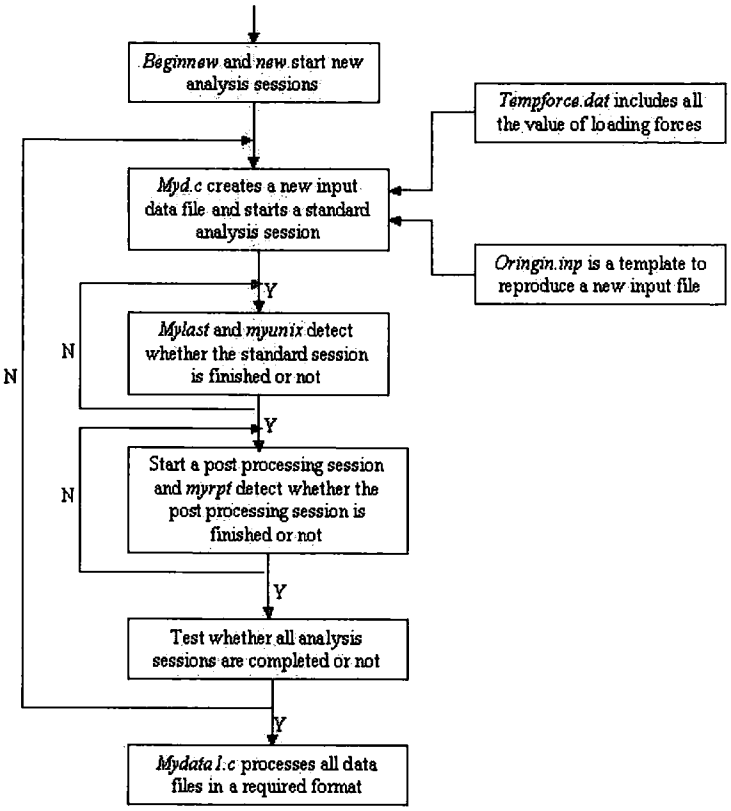

Figure 3.9: A general flow diagram for automatically running finite element calculation by ABAQUS

3.4 SIMULATION AND ANALYSIS

To test the feasibility of the algorithm described above, a computer simulation has been performed, using MATLAB software. In the simulation, the shape change algorithm described previously was programmed in MATLAB. Figure 3.10 shows a general flow diagram of the simulation algorithm. The coordinate data files calculated by using ABAQUS were compared with given void shapes. The algorithm searches the robot body shape data files generated by ABAQUS and finds the most approximate body shape corresponding to the given void shapes. The void shapes used in the simulation were a representative rectangle, ellipse and irregular shape and the approach and results are found in the following pages.

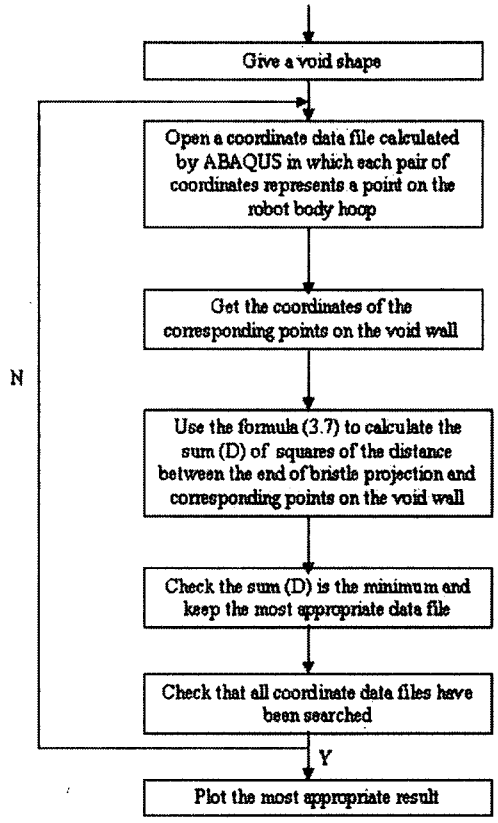

Figure 3.10: Flow diagram for the robot body shape change algorithm simulation

The current concept and embodiment of the body shape change mechanism has several constraints that limit its ability to mimic the void shapes that may occur in practice. One such limitation is the use of a symmetrical arrangement of the shape change actuators. Another limitation is the use of four actuators. In the future it may be necessary to use different arrangements but at this point of the investigation the limitations are as described above. These limitations result in a limited range of body shapes from which the rectangle, ellipse and irregular shapes investigated here were considered representative.

In order to plot the graphs simply and clearly, the simulation assumed that the body unit was not equipped with bristles. Thus, the bristle length (l) and the optimum projection of the bristle (l_{opt}) were set to equal zero in the simulation. The

simulation results show that the robot body shape change algorithm worked effectively. The following figures are taken from the simulation results and for comparison purpose bristle length has been set to zero in these figures. In Figure 3.11, the void shape is assumed to be a rectangle and the robot body is squeezed into an approximate rectangle to geometrically match the void. Similarly, the void shape in Figure 3.12 is an ellipse and the robot body changes to an ellipse to geometrically match the void. Figure 3.13 shows an irregular shape. In this case, the robot body curve fits some parts of the void but improvement could be gained from further work on non-symmetrical body shapes. In the work so far the simulation assumes that the robot body is changed into a symmetrical shape. The reason for this constraint is to make the problem as simple as possible at the current stage and also because of the physical limits of the actuators in the experimental robot body prototype. Actuators used in the prototype were linear stepper motors and they were not strong enough to withstand the side loads required to alter the spring steel strip hoop to non-symmetrical shapes because of non-symmetrical bending moments. In Figure 3.14, the steel strip hoop is a symmetrical shape, thus the bending moment AM of part A and the bending moment BM of part B are equal. The resultant moment M_o acting on the screw is thus zero. In Figure 3.15, the steel strip hoop is in a non-symmetrical shape. The bending moments AM and BM are not equal so the moment M_o acting on the screw is not zero but is the difference between AM and BM. It was found that the screw could not move in the direction of the Y-axis because of this non-zero moment M_o. Hence, for non-symmetrical cases the screw rods may become jammed and the steel strip hoop could not be changed to the non-symmetrical shape. In order to deal with non-symmetrical shapes, further work needs to be carried out using much stronger actuators.

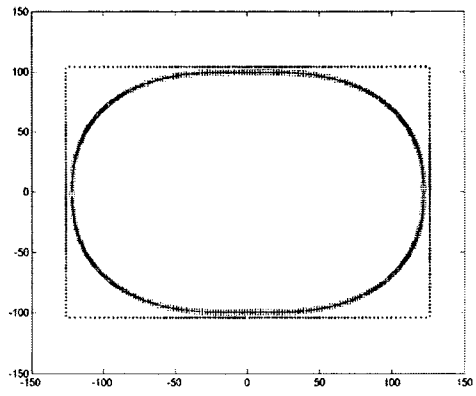

Figure 3.11: Plot of simulation results for a rectangular shape

'+' indicates a point of the robot body '.' indicates a point of the void wall

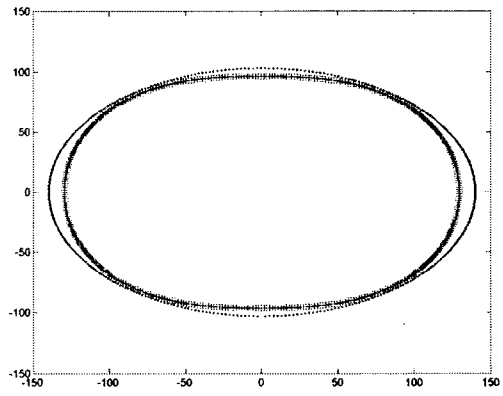

Figure 3.12: Plot of simulation results for an elliptical shape

'+' indicates a point of the robot body '.' indicates a point of the void wall

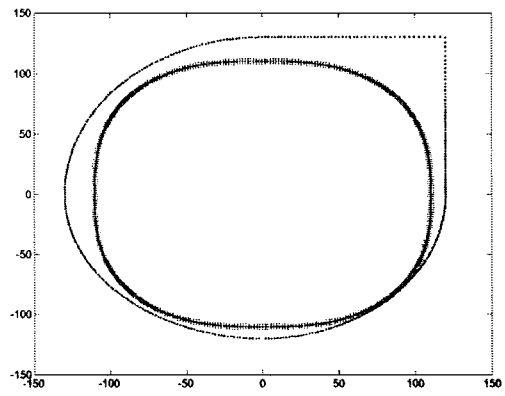

Figure 3.13: Plot of simulation results for an irregular shape

'+' indicates a point of the robot body '.' indicates a point of the void wall

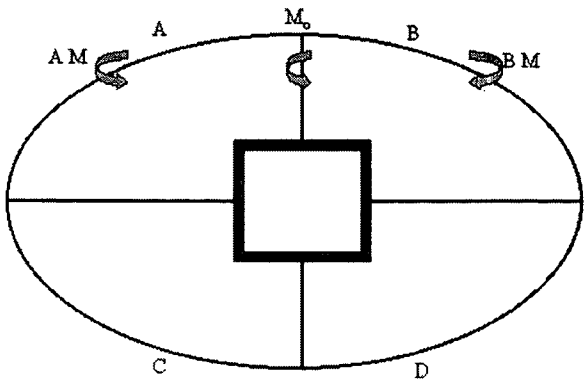

Figure 3.14: Steel strip hoop in a symmetrical shape (BM=AM)

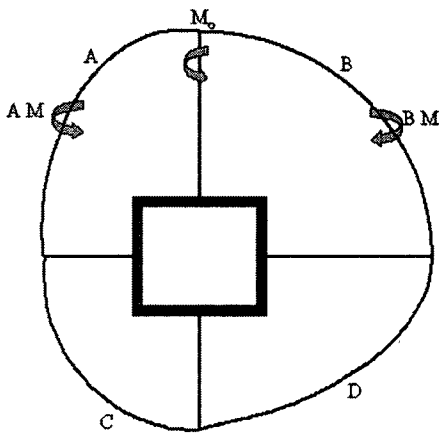

Figure 3.15: Steel strip hoop in a non-symmetrical shape (BM ≠ AM)

The above algorithm simulation assumes that the optimum condition is achieved by providing a hoop shape that corresponds geometrically to the void shape. As an approximation, this is valid if the curvature of the hoop is gentle and the bristles are short. However, if the curvature of parts of the hoop is greater and the bristles are relatively long, the external shape of the brush will deviate from the shape of the hoop, as illustrated in Figure 3.16. However, even in serious cases of such difference, the influence of the difference will be small compared to the influence of a mismatch between hoop shape and void shape. Thus, although the above difference in shape has been recognized, it was considered less important

compared with other issues of bristle hoop shape and void shape interaction, such as in the case of a circular brush in a triangular void.

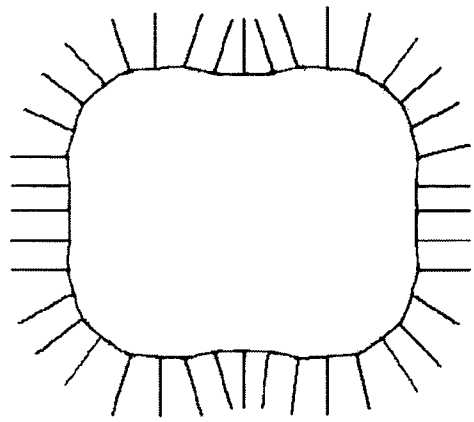

Figure 3.16: A robot body hoop with bristles

3.5 SUMMARY

Based on the description of the original brush robot working principle, the newly developed robot shape change mechanism has been described. A control algorithm for the shape change mechanism was illustrated and computer simulations have been used to test the effectiveness of the algorithm. The simulation results indicate that the algorithm works correctly and can deal with symmetrical shape change with the current robot working mechanism. Further work is needed on both the robot shape change mechanism and the shape change algorithm to allow the robot to deal with non-symmetrical shape change. Several programs written in C were used to reduce the work involved because the acquisition of the robot shape information database involves considerable keyboard input. These programs helped to simplify the data collection of robot shape information in the lab experiments. The following chapter introduces a robot void shape sensor, which is based on a strain gauge system.

CHAPTER 4

DESIGN OF ROBOT VOID SHAPE SENSOR

This chapter gives the outline of the void shape sensor structure and its working principle. The earlier part of this chapter focuses on the working principle of the robot sensor. The working principle is to use strain gauges to detect the deflections of sensor fingers. The void shape sensor consists of 12 fingers around its circular base. The coordinates of the tips of the fingers, contacting points on the void wall, can be determined by detecting the deflections of these fingers. A spline interpolation algorithm uses these coordinates to work out an approximate shape of the detected void. A detailed introduction to the spline algorithm can be found in the textbook (Ahlberg J. et al, 1967). In addition, an interpolation method used to calibrate the strain gauges is illustrated.

4.1 THE STRUCTURE AND PRINCIPLE

The literature described in Chapter 1 gives an overview of rescue robots including some discussion of sensor systems. In that review it was found that shape sensor systems were limited to those that were used for pipe and sewer inspection. There was a noticeable absence of literature relating to determination of voids in earthquake or collapsed structures. This is understandable because of the lack of

vehicles able to negotiate such voids. In the absence of a suitable vehicle, the need for a void shape sensor is not obvious. In the case of this work a vehicle is being developed which is capable of exploring complex voids. As a consequence a void shape sensor is not only useful but becomes essential to provide the data needed to reconfigure the robot body shape. However, some of technologies applied to pipe profiling are of interest and may have the capability of dealing with complex voids. Thus, a short review of these technologies is given here.

Clarke (Clarke, T., 1995) developed a laser pipe profiler based on an optical triangulation system, which used a laser light source, a lens and a linear light sensitive sensor. More details about optical triangulation can be found in Clarke's paper (Clarke, T., 1995) and Loughlin's book (Loughlin, C., 1992). The profiler was designed for the purpose of sewer pipe inspection. The profiler could detect the overall shape of the sewer pipe, whose diameter ranged from 225mm-1600mm. The profiler had a dimension 460mm long, 103mm diameter, weighed 6kg and could perform 200 measurements per second with a distance accuracy of 1mm. The profiler also used specially designed software working in Windows 95.

CleanFlow System (CleanFlow, 2001) produced a laser profiler named ClearLine Profiler, which used machine vision technology. The profiler provides the user with the ability to determine the amount of damage sustained by a pipe. The laser profiler attachment shows the actual shape of the pipe and the software can predetermine the correct pipe shape and calculate the difference between the two. The profiler can work in 6 in.– 24 in. pipes and has an accuracy of up to 1mm. A long laser probe is provided at the front of the profiler and it projects a bright line on the internal pipe wall. The aim of projecting a bright line onto the internal pipe wall is to

define a plane on the video image where measurements on the image can be translated into the real dimensions of objects observed through the camera.

It seems that a laser profiler may be used to detect a void shape but the environmental condition in voids is far different from normal pipes. There are a few challenges to the current laser profiler approach. Firstly, voids in a rescue site have more complicated shapes than normal pipes. Voids do not have a continuous straight axis as a pipe does. Thus, the long laser probe of the ClearLine profiler could be easily thrust into void walls and become damaged. The constrained void space also makes the ClearLine profiler difficult to turn (pitch or yaw). Clarke's profiler works on the optical triangulation principle, for which occlusion is a major drawback. That is, if an object occludes the view of the laser spot, then measurement will not be possible. CleanLine profiler also faces the occlusion problem. Both Clarke (Clarke, T., 1995) and Loughlin (Loughlin, C., 1992) give more detailed information about occlusion. The cross section shape of a void is so varied that deep crevices could be easily formed. This will block the return laser beam and the laser sensor cannot receive the return laser signal. If the laser light source impinges on an uneven surface texture or colour, measurement accuracy will be degraded. The void surface and its colour are uneven and varied, so measurement accuracy of Clarke's laser profiler may be degraded. Also, if the operating configuration of an optical triangulation laser sensor is altered, through changes of temperature or shock, which are very likely to happen in a rescue site, then the laser profiler will give erroneous results. In addition, the environment in voids is complicated, possibly including smoke, dirty water and other liquids. Smoke may scatter the laser beam and the laser beam may not work because the dust, debris or dirty water will deflect the laser beam. The shape reconfigurable

brush robot in this thesis was proposed to work for both earthquake rescue and oil industrial applications. In terms of industrial applications, the laser profiler will not be able to work, for example in a pipe filled with oil.

Ultrasonic distance sensors are popularly used in distance detection but a literature review did not show its application in pipe profiling. Ultrasonic sensors require that the targeting surface should be centrally located in the ultrasonic beam and within 5 degree of the beam axis. In other words, the targeting surface needs to be nearly perpendicular to the beam axis. The void shape is varied so the ultrasonic sensor may not be able to receive the reflected ultrasonic beam because the surface being detected will rarely be perpendicular to the beam. So, it will be difficult to use an ultrasonic distance sensor to detect the void shape, which has varied internal surfaces. Also, a given ultrasonic distance sensor will generally operate under certain specified operating conditions, such as temperature, air pressure and humidity, all of which can influence the sensor performance. If the actual operating environment differs from those specified, errors will result. A rescue robot working in a rescue site may experience changes of temperature, air pressure and humidity along its travel path, since major fires and flooding are likely to happen in the rescue site. More details about ultrasonic distance sensor can be found in Loughlin's book. (Loughlin, C. 1992)

The main focus of the present work relates to the reconfigurable traction system based upon bristles. At the present time, further design work on a practical sensing system for detecting the shape of complex voids is needed but is beyond the scope of this work. However, to illustrate the principle of the reconfigurable system a

strain gauge void shape sensor has been developed. The principle of the strain gauge system used in this sensor is introduced in many books, e.g. (Carvill, J., 1997), and hence details of the strain gauge application have been omitted.

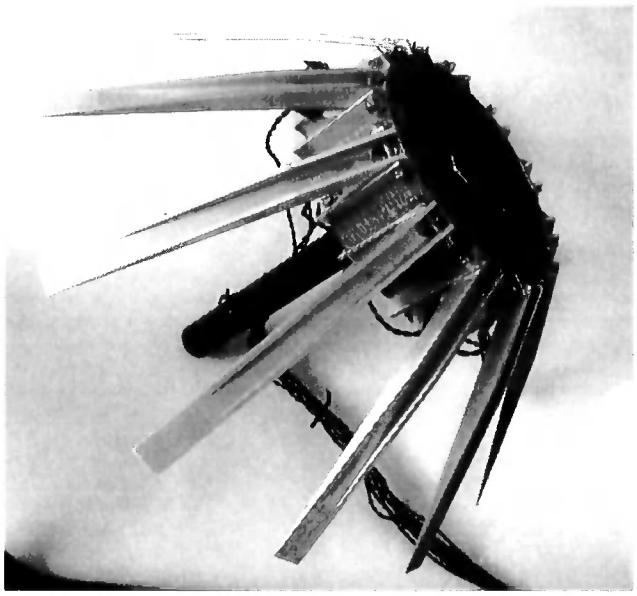

Figure 4.1: A void shape sensor based upon a strain gauge system

The void shape sensor is shown in Figure 4.1. Its working principle is very simple; a strain gauge is used to detect deflection as describe below.

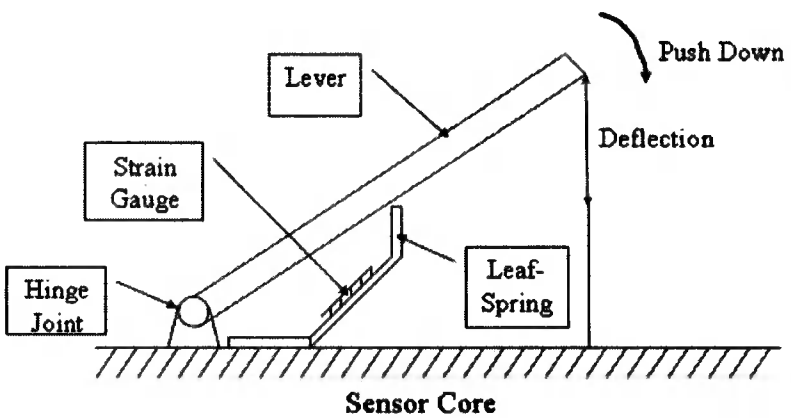

Figure 4.2: Void shape sensor working principle

In Figure 4.2, a strain gauge is mounted on a flat steel leaf-spring. One end of the leaf-spring is fixed on the sensor core and the other end is in contact with a lever. The lever rotates in the plane of the diagram. If the lever is pressed down, the leaf-spring will be bent. As a result, the strain gauge on the spring will also be deformed. The deformation of the strain gauge will change its electrical resistance. The small change of strain gauge resistance can be detected if the strain gauge is connected as an arm of a Wheatstone bridge and bridge output voltage across the middle of the bridge is amplified and measured. In this way, the relationship between the bridge output voltage and the deflection can be set up and the deflection can be obtained if the bridge output voltage is known.

By way of illustration, the graph in Figure 4.3 expresses this type of relationship. Prior to point C the output voltage rises with the increase of deflection. In the region between point A and point B, the curve is approximately linear and the deflection can be acquired by detecting the bridge output voltage signal. If the curve between A and B is divided into many small curve segments, each small curve can be considered to be linear. The relationship between the leaf-spring deflection and the bridge output voltage can be expressed as shown in Table 4.1. In the region between A and B the bridge output voltage is $V_i(i = 1,2,...,n-1,n)$, which uniquely corresponds to the leaf-spring deflection $L_i(i = 1,2,...,n-1,n)$. That means that the leaf-spring deflection can be determined by reference to Table 4.1, if the bridge output voltage is known.

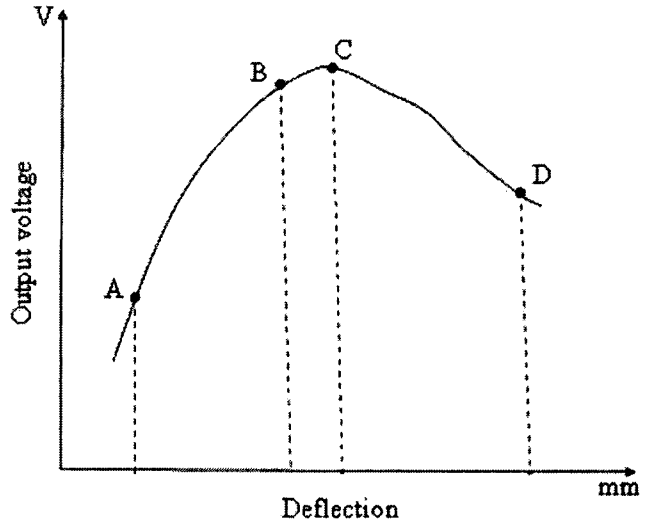

Figure 4.3: The curve of output voltage and deflection

In this application, a calibration table is used to express the relationship.

Output Voltage (v)	V_1	V_2	...	V_{n-1}	V_n
Deflection (mm)	L_1	L_2	...	L_{n-1}	L_n

Table 4.1: The calibration table of output voltage and deflection

In the table, the deflection L_1 corresponds to the unique output voltage V_1. If an output voltage V_1 is known, the deflection L_1 can be found by looking up the table. In practical application, the detected output voltage might not be exactly equivalent to V_1. For a known output voltage V, a formula based on an interpolation method is given to calculate the deflection L corresponding to V. If V is located in the span $[V_{i-1}, V_i]$ $(i = 2,3,...,n-1,n)$, L can be determined by the equation (4.1).

$$L = \left(\frac{L_i - L_{i-1}}{V_i - V_{i-1}}\right)(V - V_{i-1}) + L_{i-1} \qquad (i = 2,3,...,n-1,n). \qquad (4.1)$$

From the description above, it can be seen that one strain gauge is used to sense the deflection of a lever. Several levers are needed to detect a void shape. The structure of the sensor consists of levers mounted on a circular base, as shown in the diagram in Figure 4.4. Figure 4.4 displays a robot void shape sensor detecting a void shape, and Figure 4.1 is the photograph of the robot void shape sensor used in this work. The sensor detects the distance between the point $a_i (i = 1,2,...,11,12)$ on the void wall and the corresponding point on the circular base. Knowing these distances, an approximate void shape can be acquired by using a spline interpolation algorithm. The spline interpolation algorithm is a simple and popular curve fitting method, which has the advantage of fitting a smooth and continuous curve through given points. The algorithm uses the information from a limited number of points on the void wall to estimate the whole void shape. If a more accurate void shape is needed, more points on the void wall need to be measured, so that the spline interpolation algorithm will have more information and hence make a more accurate estimation of the void shape. However, the bristle system can deal with the small detail of the shape and hence only a general description of the shape is required.

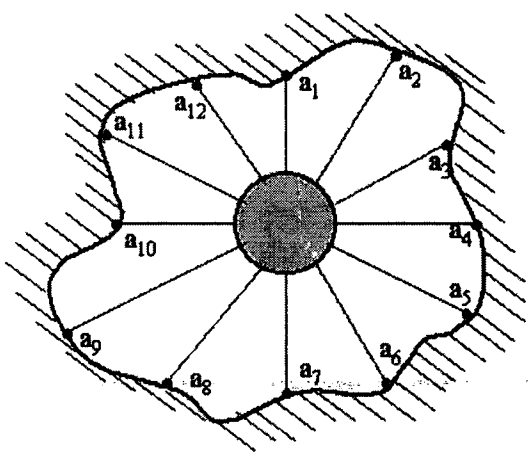

Figure 4.4: Robot void shape sensor detecting the void shape

4.2 Strain gauge system design

4.2.1 Strain gauge and its choice

Strain gauges are used to determine strains in a component or structure. The commonest type of strain gauge is the electrical resistance strain gauge. These are devices which produce an electrical signal proportional to the mechanical strain of the surface to which they are bonded. They can be made extremely small and can be attached to components.

For general strain measurement, the choice of strain gauge is made according to several criteria. These include anticipated strain level, operational temperature, installation and test environmental conditions, material being tested, specimen and strain gauge carrier compatibility with chosen adhesive, and gauge length. Specimen materials formed from compacted or bound materials (cement, concrete, chipboards, etc.) require gauge lengths to be at least three times that of the maximum particle size but, apart from this consideration, space availability and adequate performance will suggest a foil gauge of between 3mm and 10mm for use on metals.

In this work, the deflection of the lever causes the strain gauge mounted on the leaf spring to be bent and leads to a large strain. So, the strain gauge used in this work needs to be able to measure large strains. The strain gauge used to make the robot void shape sensor in this work was a YEFLA-5 strain gauge produced by Tokyo Sokki Kenkyujo Co. Ltd. The gauge size was 5mm long, 2mm wide and the backing size was 12mm long, 4mm wide. The resistance of the strain gauge was 120Ω.

4.2.2 Measurement and formulae

The mechanical strain experienced by the test specimen, and thus also by the strain gauge, gives rise to resistive strain of the gauge element. The special alloys used in strain gauges exhibit a near-linear ratio between their resistive and mechanical strains. This ratio is known as the Gauge Factor and is approximately equal to 2.0. The value is usually printed on each pack of strain gauges.

i.e. Gauge Factor $= k = \dfrac{resistive \quad strain}{mechanical \quad strain} = \dfrac{\Delta R / R}{\Delta L / L} \approx 2.0$

Using a conventional resistance-measuring meter, it would be difficult to detect, let alone accurately measure, the small change of 0.12 Ω (=0.1%) caused by 0.05% mechanical strain of a 120 Ω gauge. The Wheatstone bridge circuit, shown in its basic form in Figure 4.5, is a network of four resistances, one of which is an active strain gauge. When the ratio of resistance $\dfrac{G_1}{R_2}$ is equal to that of $\dfrac{R_4}{R_3}$, the bridge is said to be balanced and the voltage output is zero. When the resistance of the strain gauge changes, the bridge becomes unbalanced and a voltage output is created. Even though this may be small, it is a change from zero and can be amplified and measured using appropriate instrumentation.

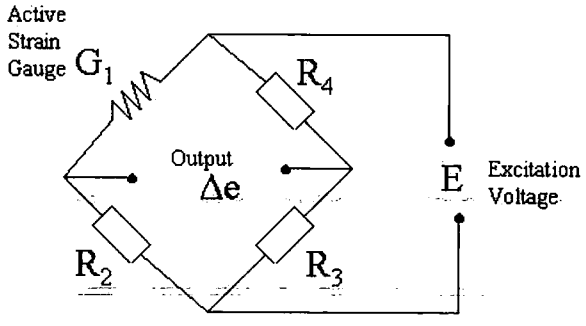

Figure 4.5: Wheatstone bridge with one strain gauge arm

It can be shown that the bridge output voltage Δe is equal to the input voltage E multiplied by the factor $\frac{G_1R_3 - R_2R_4}{(G_1 + R_2)(R_3 + R_4)}$ and so, when $G_1R_3 = R_2R_4$, $\Delta e = 0$. For the convenient case where $R = G_1 = R_2 = R_3 = R_4$, if G_1 changes to $R + \Delta R$ due to strain, Δe becomes $\frac{\Delta RE}{4R + 2\Delta R}$. If $2\Delta R$ is ignored since it is very small compared to $4R$, Δe becomes $\frac{\Delta RE}{4R}$. Since $\frac{\Delta R}{R} = \frac{k\Delta L}{L}$ and $\frac{\Delta L}{L} = Strain = \varepsilon$, Δe becomes $\frac{\varepsilon kE}{4}$.

4.3 SUMMARY

This chapter describes the working principle and design of a strain gauge sensor used to detect the void shape. The strain gauge sensor is able to detect the positions of a group of points on the void wall. According to this position information, the spline interpolation algorithm can estimate the approximate void shape. Although the estimated void shape is not exactly the same as the real void shape, it is sufficient for the current robot shape change experiment in the lab. Further design work on a practical sensing system for detecting the shape of complex voids is needed. It is noted that the resistance change of a strain gauge is small. So, a Wheatstone bridge and an amplifier are used to detect the small resistance change.

The strain gauge void shape sensor described above presents some application difficultly relating to its operation if the robot is being withdrawn. A simple solution is the retraction of the sensor in the manner of closing an umbrella. If it is necessary to

monitor void shape during withdraw, it may be necessary to install two void shape sensors operating in opposite directions and deployed or retracted, depending on the direction of trail of the robot.

CHAPTER 5

SENSOR BASED ROBOT BODY SHAPE CHANGE

To verify that the robot body shape change concept is feasible, a robot variable geometry component prototype has been developed to both illustrate the concept and for testing. If this component prototype is successful, it should be possible to assembly further components to build a whole robot. In the experimental work described in this chapter, the robot prototype includes a sensor system, a robot variable geometry component and a control system.

5.1 ROBOT CONTROL SYSTEM

5.1.1 Control module

It was envisaged that a control program would run on a PC (personal computer) and that a sensor system would collect the information of void shape and send this information to the PC. After processing the sensor signals, the control program sends appropriate control commands to each actuator control module. The control modules control the movements of the actuators, following those control commands. Figure 5.1 shows that the robot control system includes two layers. One layer is the control from the PC to each control module; the other layer is the control from the control module

to the actuator. In the robot prototype experimental work, four linear stepper motors were chosen as actuators and two stepper motor control boards were used as control modules. The stepper motor control board was a two-axis controller and consequently could control two stepper motors simultaneously. Each stepper motor needed an individual drive board. The sensor system is composed of a void shape sensor, as described in the previous chapter. In addition, the sensor system includes an amplifier system, a DC power supply and an A/D acquisition card.

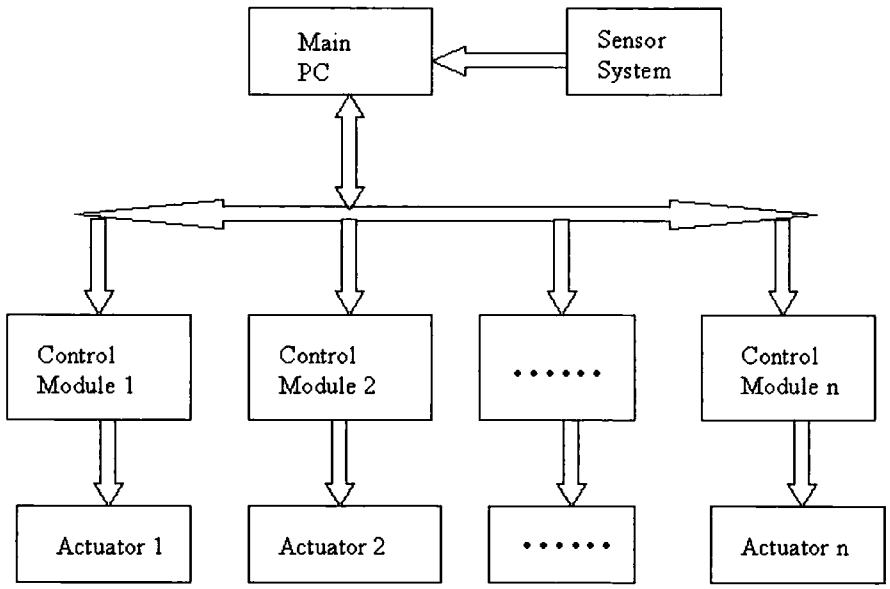

Figure 5.1: Robot control module diagram

5.1.2 Control board

The variable geometry component was controlled by means of two stepper motor control boards, four stepper motor drive boards, four stepper motors and one personal computer. In Figure 5.2, a schematic diagram is drawn to explain the connections between these components.

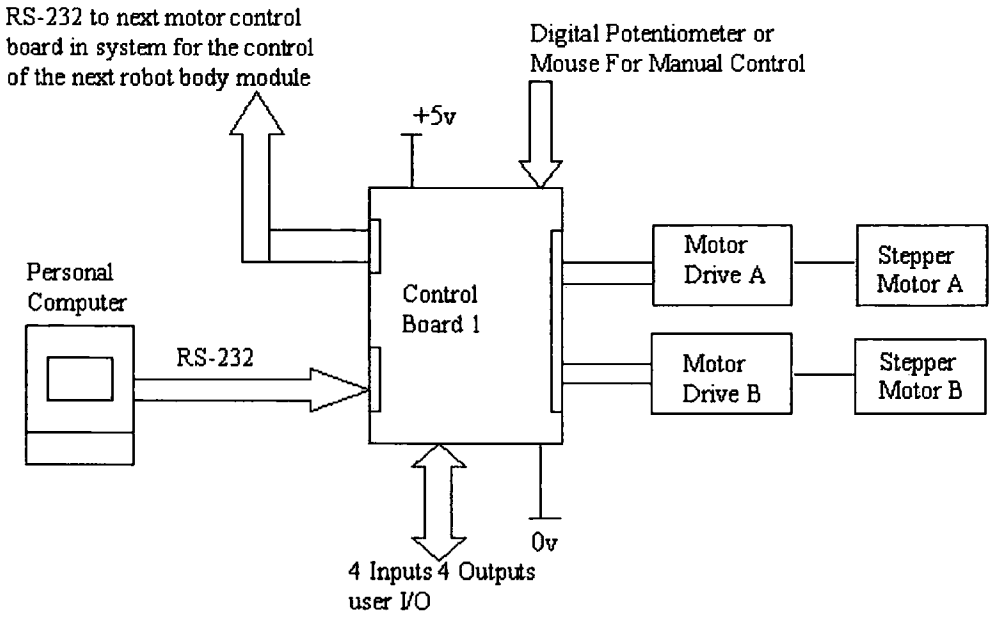

Figure 5.2: Control board diagram

5.1.3 Introduction to the Swift 200 control board

The control board used in the robot component prototype experiment was a Swift 200 two axes stepper motor controller as shown in Figure 5.3. The Swift 200 controller was a control board specially designed for the stepper motor used and was supplied by the motor manufacturer.

The Swift 200 is supplied on a standard Eurocard (160mm x 100mm) with a 64 way connector and is suitable for an existing racking system. The Swift 200 allows monitoring of drive conditions (moving or not) and can detect limit switches connected to the board. The board controls one or two stepper motors via stepper motor drive boards. Moreover, it could be programmed using a RS232 serial link from a PC. Its simple programming language is a derivative of C; example programs are

shown in the control board manual. Communication with additional Swift 200 control boards is easily achieved by daisy chaining which allows control of many stepper motor drive boards. Both axes can be moved individually or simultaneously. The axes can also be moved manually by hand encoders. More details of the Swift 200 control board can be found in its manual.

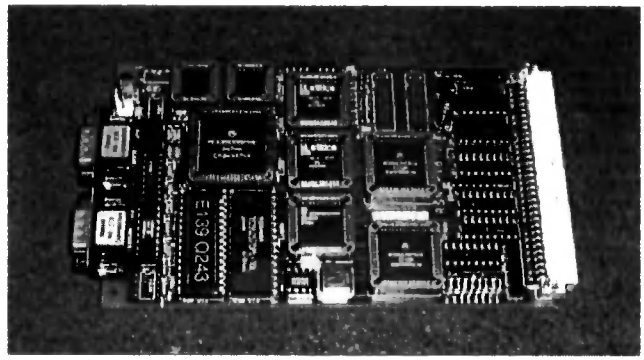

Figure 5.3: Swift 200 stepper motor controller

5.2 ROBOT VOID SHAPE SENSOR SYSTEM

The robot void shape sensor system includes a strain gauge sensor, a group of amplifier boards, an A/D acquisition card and a DC power supply. The output voltage signal from a strain gauge is small and hence an amplifier board is needed to amplify the small output voltage signal to the volt level for each strain gauge. The input signal for the A/D acquisition card needs to be set to a [-5V, +5V] span. In the experimental work, a standard strain gauge amplifier, incorporating a Wheatstone bridge was chosen. Twelve amplifier modules are needed for the sensor system since the sensor system includes 12 channel strain gauges. Also a power supply is needed to drive the amplifiers.

5.2.1 Introduction to PCI-30G-32 data acquisition card

The PCI-30G-32 data acquisition card comprises 12-bit analog input and is a multifunction board. It can be supplied as a 32 channel device with a conversion rate of 100KS/s. The board supports 16 differential or 32 single-ended A/D inputs and has flexible digital I/O capabilities in three ports. Each port can be configured as inputs or outputs. Analog output and input signals are made available on the 50-way connector. The data acquisition card has other additional functions, which are not used in this work. More details about these functions can be found in its manual. The PCI-30G-32 data acquisition card was chosen to conduct the data acquisition work because twelve channels of strain gauge signals needed to be sampled and the card was able to support up to 16 differential inputs.

5.2.2 Calibration of robot void shape sensor

The strain gauge sensor needed to be calibrated and the data was integrated into a calibration table, as described in the last chapter. In Figure 5.4, a toothed ruler was used to calibrate the sensor. The strain gauge output signal changed in proportion to the displacement of the sensor finger. Displacement was controlled by a toothed ruler, giving increment of the distance between the centre line of the sensor handle and the finger end point. When calibrating, a sensor finger was used to detect the output signal three times for each ruler location and calculate the mean value. So, a calibration table was created for the sensor finger for all ruler locations. This calibration procedure needed to be repeated for each sensor finger.

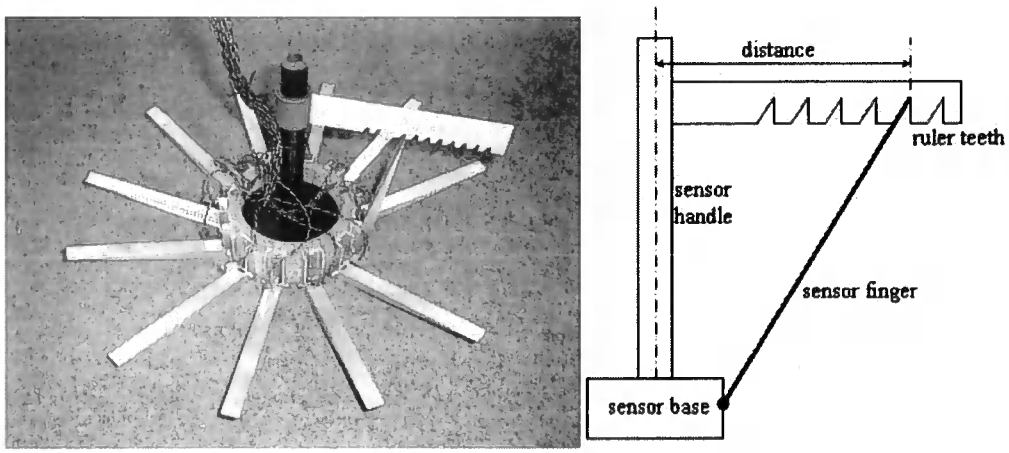

Figure 5.4: Strain gauge sensor in the calibration

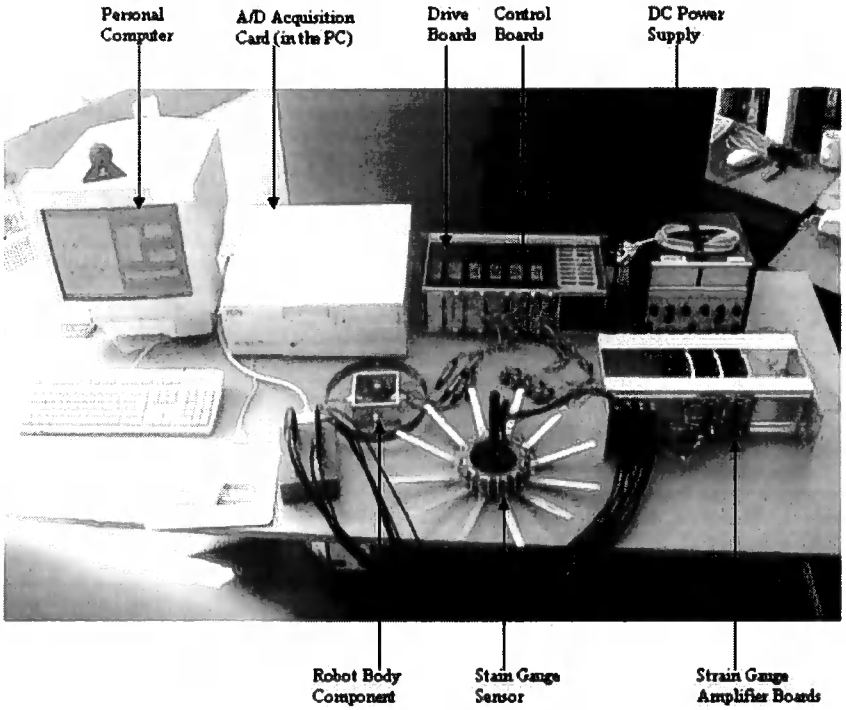

Figure 5.5: Robot experiment devices

5.3 ROBOT SOFTWARE SYSTEM

A computer program written in Visual C++ was developed for the robot prototype experiment to collect sensor signals and control actuators to realize the robot body shape change algorithm. Figure 5.8 illustrates the program interface. The

figure in the left window shows how the robot body component will alter its body shape to fit the void. The black line expresses the outline of the robot body component and the grey line expresses the outline of the void wall. The right window displays the communication working status, serial port configuration and the stepper motor working status. Figure 5.6 shows the interface of the data acquisition program, which displays the data acquisition card information including 16 analog input channels in differential mode. Only 12 channels in differential mode are used in this experiment since there are only 12 strain gauge output signals to be converted.

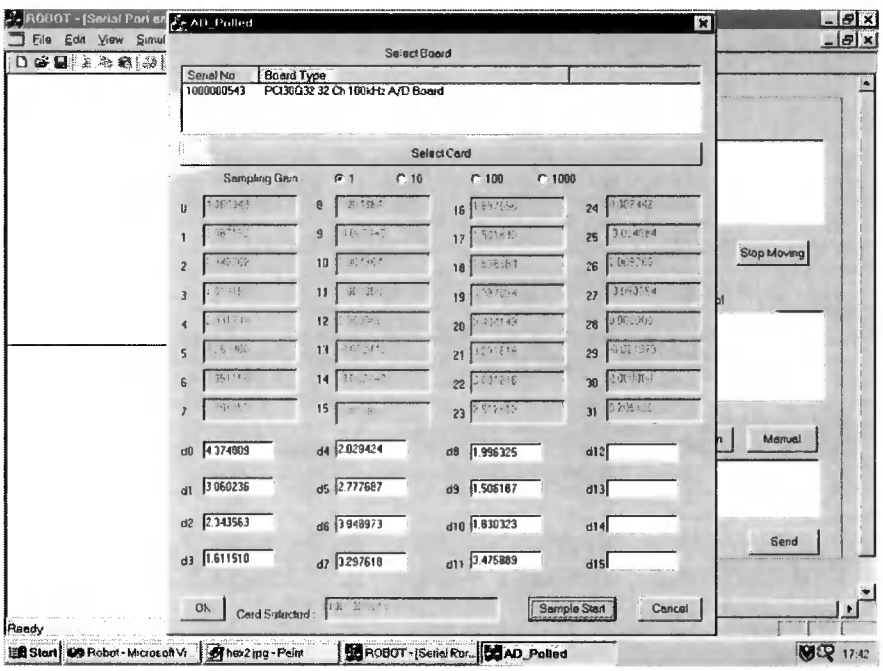

Figure 5.6: Data acquisition interface

5.4 ROBOT BODY SHAPE CHANGE EXPERIMENTS

5.4.1 Experimental procedure

Figure 5.5 shows the robot body component experimental device, which includes a robot void shape sensor, a control system, a robot body component and a

PC. To simulate the void shape and test the robot shape change mechanism, several wooden boxes were made in basic regular geometrical shapes and one irregular geometrical shape. As the robot void shape sensor was only a prototype to test the effectiveness of robot shape change algorithm, the more complicated void shapes that may be encountered in a real environment were not considered in this experiment. The regular geometrical boxes in the experiment include a square, a rectangle, a triangle and a hexagon.

The following procedure was used in all of the experiments. Firstly, the robot void shape sensor was inserted into the relevant box, simulating a void shape. Then the data acquisition card collected the box shape information from the sensor and sent it to the PC. The robot body shape control program running on the PC calculated an approximate shape of the box and decided how the stepper motors should move in order to change the robot body component shape to match the box as closely as possible. Then, the program sent the control command to the control module via the serial communication and the control module controlled the stepper motors to move as much as the program indicated. The robot body component was then put into the box to see how well the robot body component fitted the box shape. The experimental procedure was repeated for each different shape of box.

To verify that the robot body component behaved in the manner predicted by the ABAQUS analysis described in Chapter 3, a practical measurement and verification experiment was carried out in which a Mitutoyo coordinate measuring machine was used to measure the actual shape of the robot body component. The robot body component was assumed always to be symmetrical, so it was only

necessary to measure a quarter of the robot body component. The coordinate measuring machine measured 23 points on the quarter of the robot body component. These measurements were made at two heights, which were two positions across the width of the hoop. The coordinates were recorded and a mean value of the two measurements was used to plot a shape graph. A mean of two readings was used because the robot body hoop was a thin spring steel strip and the strip might be twisted when the robot body hoop was deformed. The theoretical coordinate data file corresponding to the most appropriate robot body shape calculated by the robot body shape change algorithm, using ABAQUS, was compared with the measurements taken using the coordinate measuring machine. The shape measurement process was repeated for a number of robot body shapes. Data obtained from the coordinate measuring machine is appended in the appendix. This data has been plotted in Figures 5.10, 5.14, 5.18, 5.22 and 5.26. In these figures, the theoretical robot body shape suggested by ABAQUS is indicated by the symbol '•' and the actual measured result is shown by the symbol '+'. The following sections describe and discuss robot body component experiments for the different box shapes.

5.4.2 Robot body shape change experiment in a square box

Figure 5.7 shows the robot void shape sensor in a square box simulating a square void shape. The sensor fingers were in contact with the box wall and were able to detect the box shape. The robot body shape control program collected the sensor output signals and calculated an approximate shape for the square box. The shape was approximately square, as indicated by the grey line in Figure 5.8. After acquiring the approximate shape, the robot body shape control program used the robot body shape

change algorithm described in section 3.1.3 of Chapter 3 to search the robot body shape database and find the most appropriate shape to fit the square box. In this case, the most appropriate shape found by the robot body shape control program was the approximate square indicated by the black line in Figure 5.8. After comparing this approximate square shape with the original circular shape of the robot body component, the robot body shape control program decided the required movement of the stepper motors and sent a control command to change the robot body component shape to the new shape. The right-hand window in Figure 5.8 shows the communication between the robot body shape control program and the control module. All of the stepper motors moved accordingly and the robot body component changed to an approximate square shape to match the square box. Figure 5.9 shows how well the changed robot body component matched the square box.

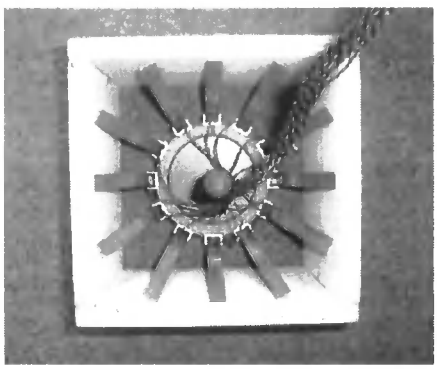

Figure 5.7: Robot void shape sensor detects the square box

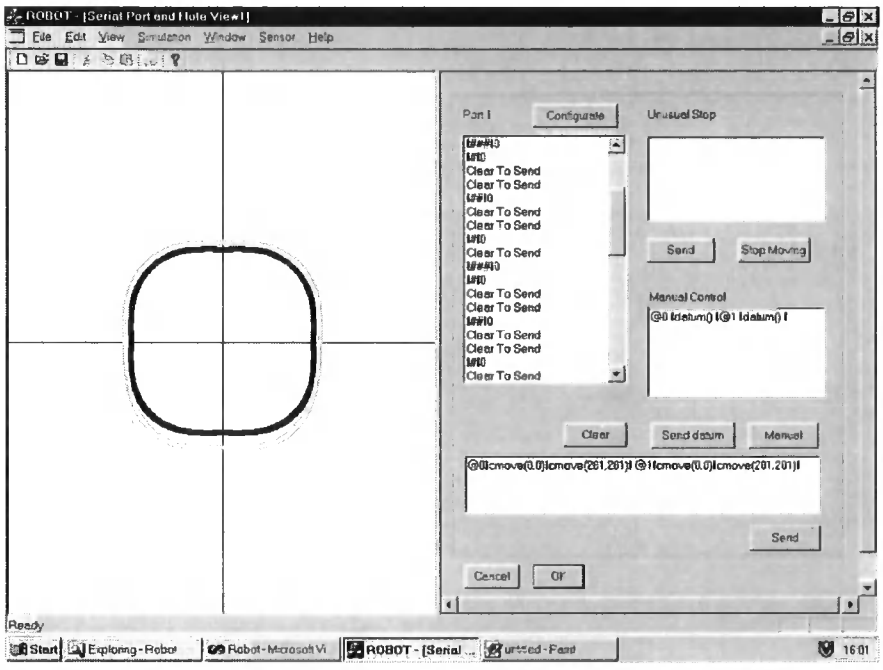

Figure 5.8: Robot control software interface of the square box case

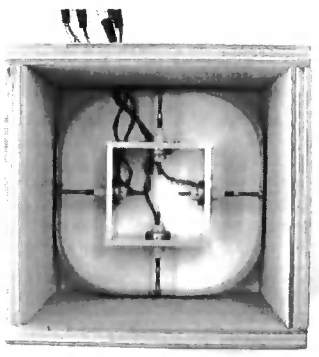

Figure 5.9: Robot body component in the square box

To see whether the robot body component changed to the approximate square suggested by the theoretical ABAQUS calculation, a coordinate measurement and verification experiment was conducted, as described in section 5.4.1. The results of this experiment are plotted in Figure 5.10. An error calculation of the coordinate measurement result and theoretical robot body shape suggested by ABAQUS was conducted. The sum of squared deviation, mean deviation, maximum deviation and

minimum deviation between the coordinate measurement and the theoretical robot body shape suggested by ABAQUS were calculated and the results are listed in Table 5.1.

	Δd_{sum}^2	$\Delta \bar{d}$	$\Delta d_{\max}$	$\Delta d_{\min}$
Square box case	212.140	2.932	4.262	1.820
Rectangular box case	123.830	1.133	4.192	0.076
Hexagonal box case	190.771	1.421	4.657	0.066
Triangular box case	12.421	0.661	1.243	0.032
Irregular shape box case	36.382	0.909	2.166	0.056
Note:				
The sum of squared deviation: Δd_{sum}^2		Mean deviation: $\Delta \bar{d}$		
Maximum deviation: $\Delta d_{\max}$		Minimum deviation: $\Delta d_{\min}$		

Table 5.1: An error calculation of coordinate measurements and theoretical shapes suggested by ABAQUS

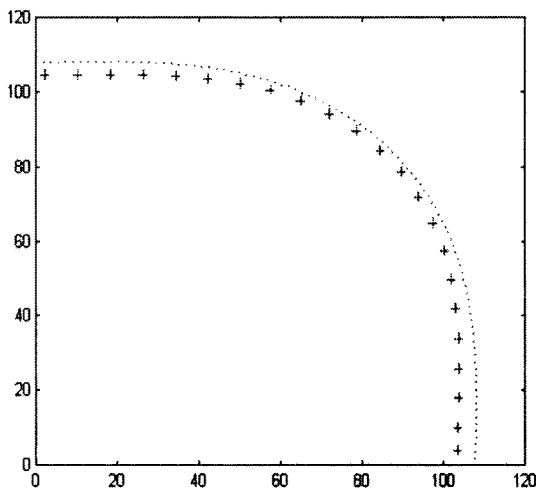

Figure 5.10: The verification plot of the square box case
Note: '•' the theoretical robot body shape suggested by ABAQUS
'+' the actual robot body shape measured by coordinate measuring machine

The experiments showed that the robot sensor could detect the square box shape and the robot body shape control program could find an approximate square shape from the robot body shape database to match the detected box shape. The changed robot body component shape matched the square box well. Although there is

a small mean deviation of 2.932mm, Figure 5.10 shows that the actual robot body component shape has a similar curvature shape to the theoretical shape suggested by ABAQUS. The deviation between the actual robot body component shape and the theoretical shape suggested by ABAQUS was also found in other cases described in the following sections. The reasons for this deviation are discussed in section 5.4.7.

5.4.3 Robot body shape change experiment in a rectangular box

Figure 5.11 shows the robot void shape sensor in a rectangular box. The sensor fingers were in contact with the box wall and were able to detect the box shape. The robot body shape control program collected the sensor output signals and calculated an approximate shape for the rectangular box. The shape was approximately rectangular as indicated by the grey line in Figure 5.12. Using the robot body shape control algorithm and search process as mentioned in the square box case of section 5.4.2, the robot body shape control program found the most appropriate shape to fit the rectangular box. In this case, the shape found by the robot body shape control program was an approximate rectangle as indicated by the black line in Figure 5.12 and the robot body component changed to this shape. After comparing the approximate rectangle with the original shape of the robot body component, the robot body shape control program decided the required movement of the stepper motors and sent a control command to change the robot body component shape to the approximate rectangle. Following the control command, the stepper motors in the Y-axis were moved in and the stepper motors in the X-axis were moved out slightly. Figure 5.13 shows how the changed robot body component matched the rectangular box.

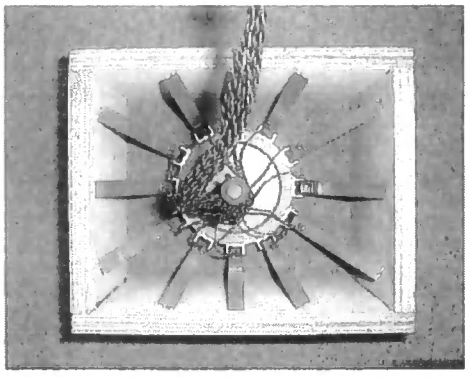

Figure 5.11: Robot void shape sensor detects the rectangular box

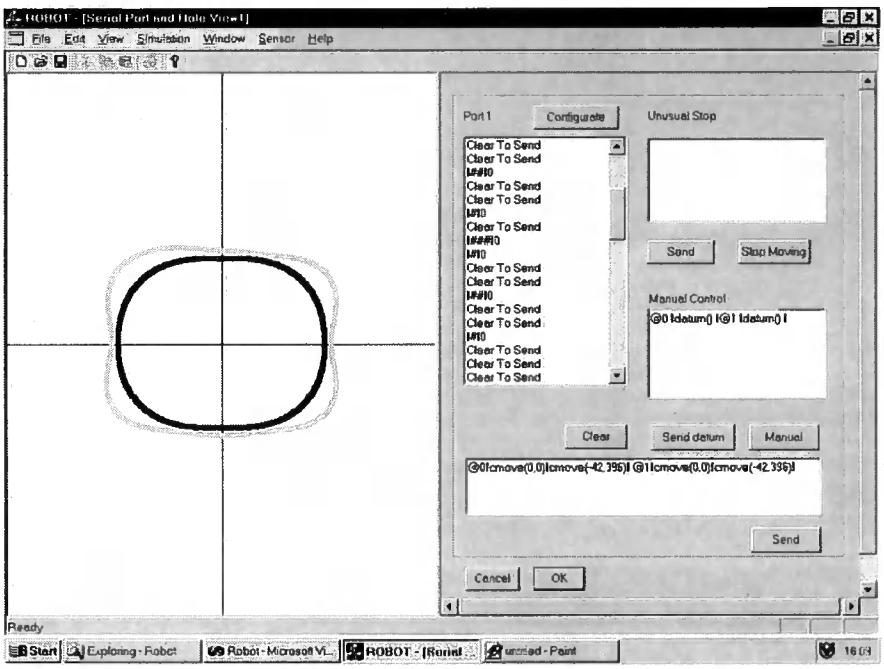

Figure 5.12: Robot control software interface of the rectangular box case

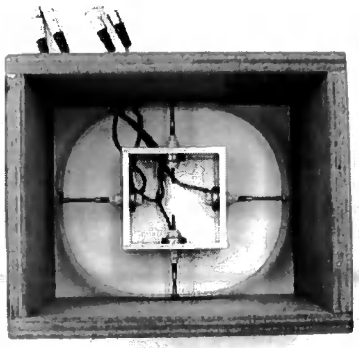

Figure 5.13: Robot body component in a rectangular box

To see whether the robot body component changed to the approximate rectangular shape suggested by the theoretical ABAQUS calculation, the coordinate measurement and verification experiment conducted in section 5.4.2 was repeated. The results of this experiment are plotted in Figure 5.14. It can be seen that nearly half of the measured points on the actual robot body component overlap the curve of the theoretical shape. An error calculation of the coordinate measurement result and theoretical rectangular shape suggested by ABAQUS was conducted. The sum of squared deviation, mean deviation, maximum deviation and minimum deviation between the coordinate measurement and the theoretical shape suggested by ABAQUS were calculated and the results are listed in Table 5.1. The mean deviation, minimum deviation and sum of squared deviation were relatively smaller than in the case of the square box.

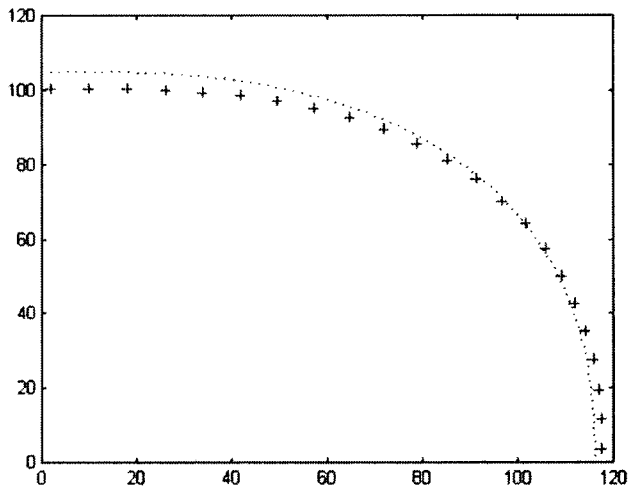

Figure 5.14: The verification plot of the rectangular box case
Note: '•' the theoretical robot body shape suggested by ABAQUS
'+' the actual robot body shape measured by coordinate measuring machine

The experiments showed that the robot sensor could detect the rectangular box shape and the robot body shape control program could find an approximate rectangular shape from the robot body shape database to match the box shape. The

robot body component changed to the approximate rectangle and matched the box shape. The deviation between the actual robot body component shape and theoretical shape was caused by several reasons, which will be discussed in section 5.4.7.

5.4.4 Robot body shape change experiment in a hexagonal box

Figure 5.15 shows the robot void shape sensor in a hexagonal box. The sensor fingers were in contact with the box wall and were able to detect the box shape. The robot body shape control program collected the sensor output signals and calculated an approximate shape for the hexagonal box. The shape was approximately hexagonal as indicated by the grey line in Figure 5.16. Using the robot body shape control algorithm and search process as described in section 5.4.2, the robot body shape control program found the most appropriate shape to fit the hexagonal box. In this case, the shape found by the robot body shape control program was an ellipse as indicated by the black line in Figure 5.16. After comparing the ellipse with the original shape of the robot body component, the robot body shape control program decided the required movement of the stepper motors and sent a control command to change the robot body component shape to the ellipse. Following the control command, the stepper motors in the Y-axis were moved in and the stepper motors in the X-axis were moved out. The right-hand window in Figure 5.16 shows the communication between the robot body shape control program and the control module. Figure 5.17 shows how the changed robot body component matched the hexagonal box.

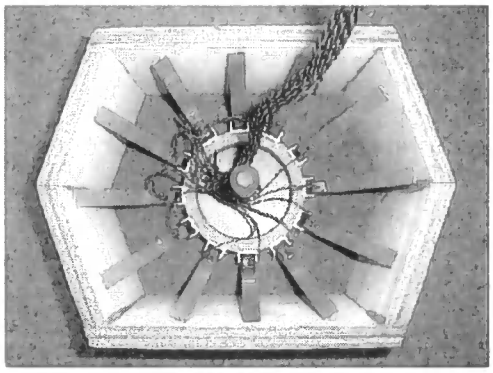

Figure 5.15: Robot void shape sensor detects the hexagonal box

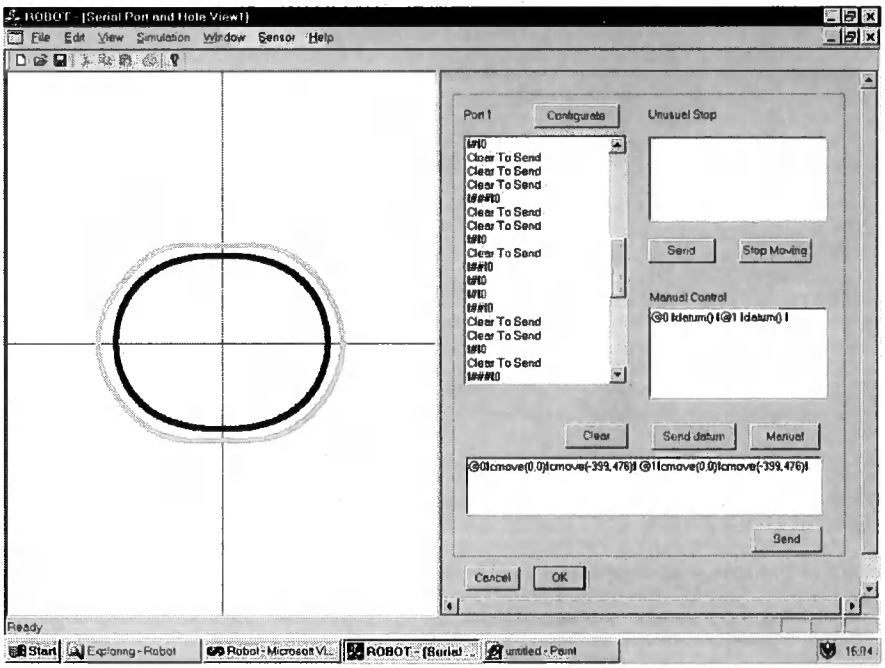

Figure 5.16: Robot control software interface of the hexagonal box case

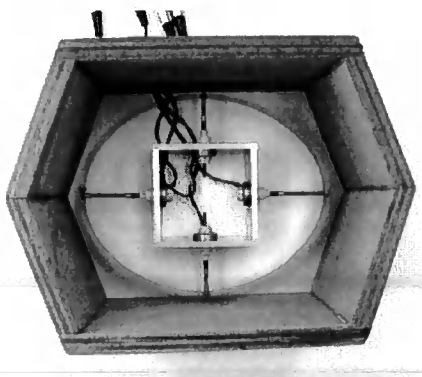

Figure 5.17: Robot body component in the hexagonal box

To see whether the robot body component changed to the elliptical shape suggested by the theoretical ABAQUS calculation, the coordinate measurement and verification experiment conducted in section 5.4.2 was repeated. The experimental result was plotted in Figure 5.18. An error calculation of the coordinate measurement result and theoretical elliptical shape suggested by ABAQUS was conducted. The sum of squared deviation, mean deviation, maximum deviation and minimum deviation between the coordinate measurement and the theoretical robot body shape suggested by ABAQUS were calculated and the results are listed in Table 5.1. The hexagonal box case had the biggest maximum deviation.

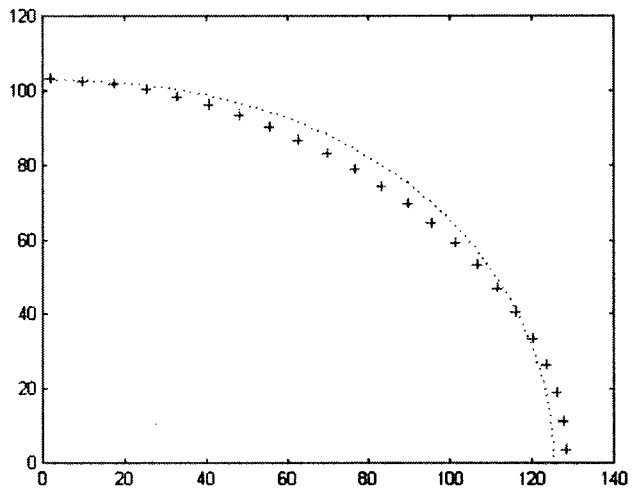

Figure 5.18: The verification plot of the hexagonal box case
Note: '•' the theoretical robot body shape suggested by ABAQUS
'+' the actual robot body shape measured by coordinate measuring machine

The experiments showed that the robot sensor could detect the hexagonal box shape and the robot body shape control program could find an ellipse from the robot body shape database to best match the detected box shape.

5.4.5 Robot body shape change experiment in a triangular box

Figure 5.19 shows the robot void shape sensor in a triangular box. The sensor fingers were in contact with the box wall and were able to detect the box shape. The robot body shape control program collected the sensor output signals and calculated an approximate shape for the triangular box. The shape was approximately triangular as indicated by the grey line in Figure 5.20. Using the robot body shape control algorithm and search process as described in section 5.4.2, the robot body shape control program found the most appropriate shape to fit the triangular box. In this case, the shape found by the robot body shape control program was a circle, as indicated by the black line in Figure 5.20. Thus, the robot body shape control program decided to keep the robot body component shape as a circle and sent a control command to the control modules to keep the circular shape. Figure 5.21 shows the circular shape of the actual robot body component.

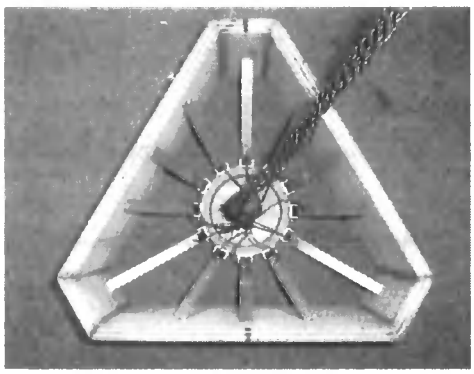

Figure 5.19: Robot void shape sensor detects the triangular box

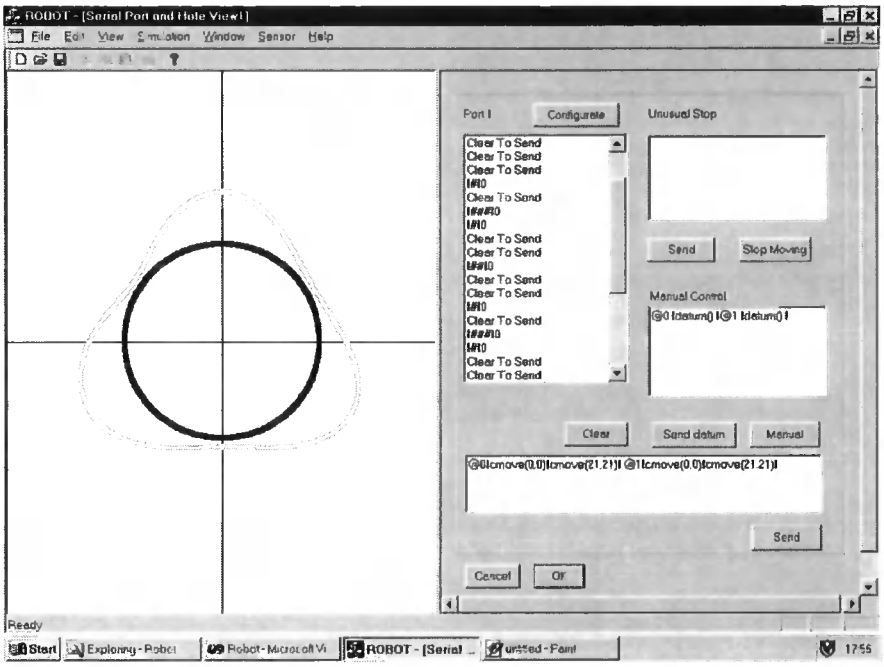

Figure 5.20: Robot control software interface of the triangular box case

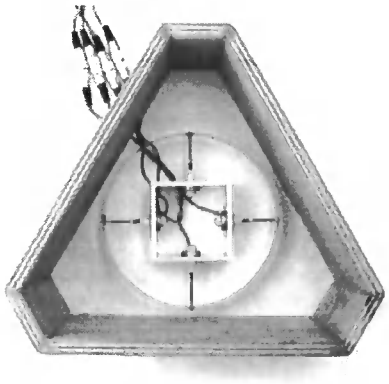

Figure 5.21: Robot body component in the triangular box

To study the difference between the actual robot body component shape and the theoretical shape suggested by the ABAQUS calculation, the coordinate measurement and verification experiment conducted in section 5.4.2 was repeated. The results of this experiment are plotted in Figure 5.22. It can be seen that the actual robot body component shape matched the theoretical shape. An error calculation of the coordinate measurement result and the theoretical shape suggested by ABAQUS was conducted. The sum of squared deviation, mean deviation, maximum deviation

and minimum deviation between the coordinate measurement and theoretical robot body shape suggested by ABAQUS were calculated and the results are listed in Table 5.1. As might be expected, keeping the flexible hoop as a circle meant that the triangular box case had the smallest mean deviation, maximum deviation, minimum deviation and sum of squared deviation among all the cases.

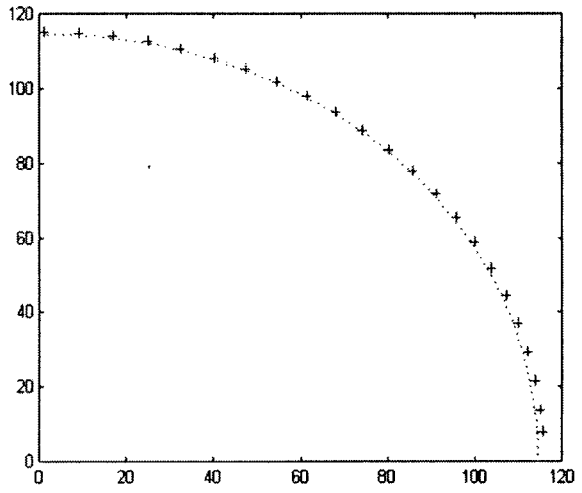

Figure 5.22: The verification plot of the triangular box case
Note: '•' the theoretical robot body shape suggested by ABAQUS
'+' the actual robot body shape measured by coordinate measuring machine

The experiments showed that the robot sensor could detect the triangular box shape and the robot body shape control program found a circular shape from the robot body shape database to match the detected box shape. A triangular robot body shape was considered to be a more appropriate shape to match the triangular box than the circular shape. However, the current robot body component can only change its shape symmetrically in both X-axis and Y-axis because of the limitation of its physical structure. Further discussion is given in section 3.1.4 and at the conclusion of this chapter.

5.4.6 Robot body shape change experiment in a box of irregular shape

Figure 5.23 shows the robot void shape sensor in a box of irregular shape. The sensor fingers were in contact with the box wall and were able to detect the box shape. The robot body shape control program collected the sensor output signals and calculated an approximate shape for the box. The shape is indicated by the grey line in Figure 5.24. Using the robot body shape control algorithm and search process as described in section 5.4.2, the robot body shape control program found the most appropriate shape to fit the irregular shape box. In this case, the shape found by the robot body shape control program was an ellipse indicated by the black line in Figure 5.24. After comparing the ellipse with the original robot body component shape, the robot body shape control program decided the movement of the stepper motors and sent a control command to change the robot body component shape to the ellipse. Following the control commands, the stepper motors in the Y-axis were moved in and the stepper motors in the X-axis were moved out. The right-hand window in Figure 5.24 shows the communication between robot body shape control program and the control module. Figure 5.25 shows how the changed robot body component matched the box.

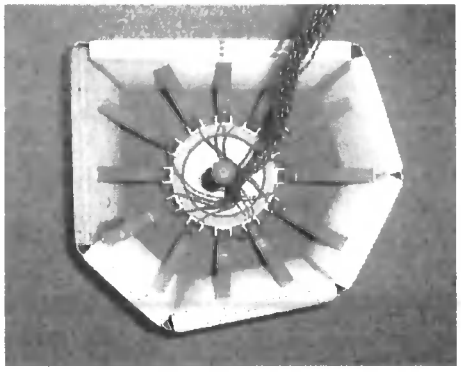

Figure 5.23: Robot void shape sensor detects an irregular shape box

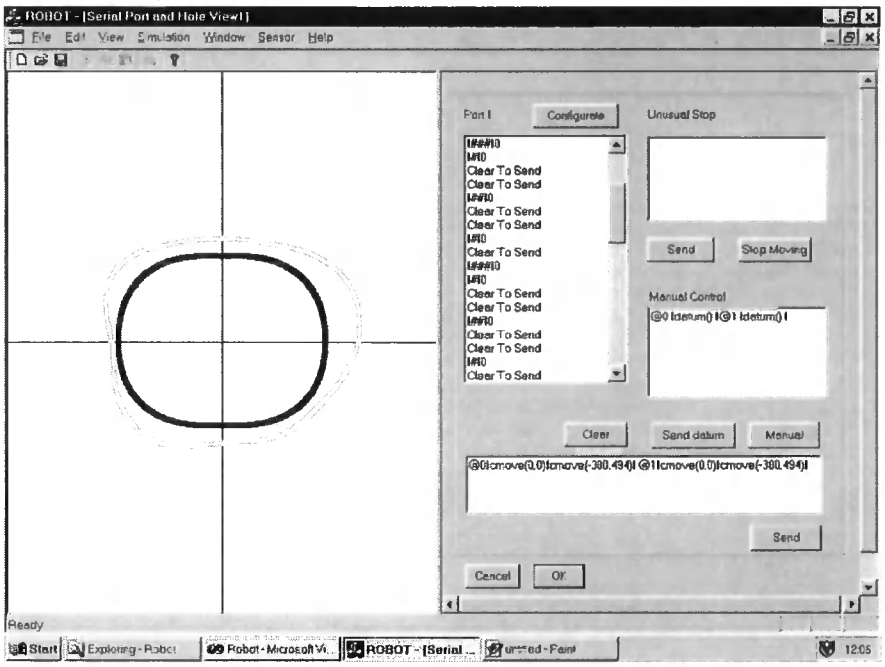

Figure 5.24: Robot control software interface of the irregular shape box case

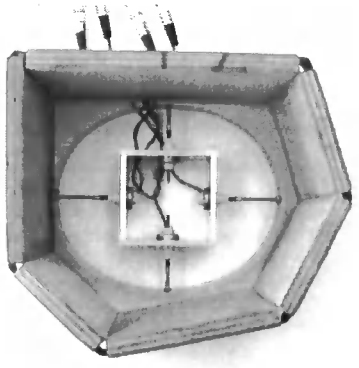

Figure 5.25: Robot body component in the box of irregular shape

To study the difference between the actual robot body component shape and the theoretical shape suggested by the ABAQUS calculation, the coordinate measurement and verification experiment as described in section 5.4.2 was repeated. The experimental results are plotted in Figure 5.26. It can be seen that most of the measured points on the actual robot body component coincide with the curve of the theoretical shape. An error calculation of the coordinate measurement result and the

theoretical elliptical shape suggested by ABAQUS was conducted and the results are listed in Table 5.1. The irregular shape box case has the second smallest mean deviation, maximum deviation, minimum deviation and sum of squared deviation among all the cases.

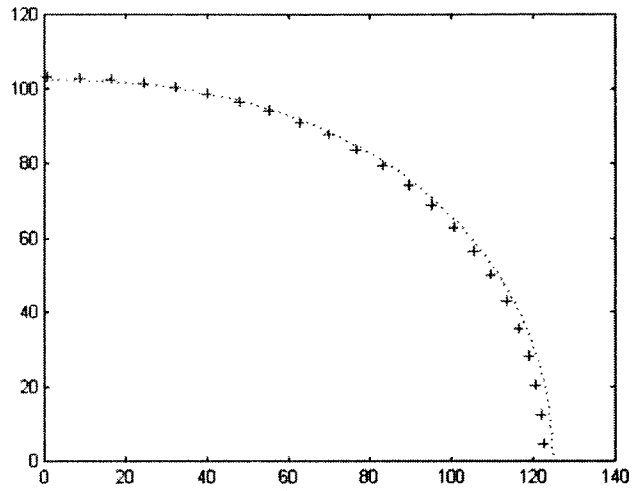

Figure 5.26: The verification plot of the irregular shape box case
Note: '•' the theoretical robot body shape suggested by ABAQUS
'+' the actual robot body shape measured by coordinate measuring machine

The experiments showed that the robot sensor could approximately detect the irregular shape box and the robot body shape control program found an elliptical shape from the robot body shape database to best match the detected box shape. The robot body shape database did not include an irregular shape because the current robot body component can only change its shape symmetrically in both X-axis and Y-axis due to the limitations of its physical structure. So, the robot body component did not change to an irregular shape to match the irregular shape box closely. Further hardware and software work is needed to enable the robot to change its body shape non-symmetrically.

5.4.7 Discussion of robot body shape change experiments

In the robot body component experiments, the robot body component could change its shape to correspond to the box shape. Among the five cases studied in the verification experiment of robot body shape change, two cases for Figure 5.22 and Figure 5.26 show that the actual shapes of the robot body component were well matched to the theoretical robot body shapes suggested by the ABAQUS analysis. They have smaller deviations than the other cases. The other three cases studied in the verification experiment of robot body shape change, Figure 5.10, 5.14 and 5.18, show that the actual robot body component shapes basically match the theoretical robot body shapes suggested by ABAQUS. For these cases, the mean deviations between the actual robot body component shapes and the theoretical shapes suggested by ABAQUS are in the range of 1-3mm. The small differences between the actual robot body component shapes and the theoretical shapes in these figures are caused by several factors. For example, the stepper motor of the robot body component may have a positioning error, causing its movement away from the suggested position assumed by the robot body shape change algorithm. The steel strip of the robot body component may be twisted during deformation since it is thin and elastic. This may cause a small error of the coordinate measurement and subsequently lead to the difference between the coordinate measurement of the actual robot body component shape and the theoretical shape suggested by ABAQUS. To minimize the measurement error, the measurements were made at two heights, which were two positions across the width of the strip. The coordinates were recorded and a mean value of the two measurements was used to plot the verification graph. In the coordinate measurement of the actual robot body component shape, the coordinate

measuring machine needed to assume a central point for the robot body component and take this point as the origin for the coordinate measuring system. The actual robot body component may not be a perfectly symmetrical shape, so the origin assumed by the coordinate measuring machine may not be the same as the origin assumed in the ABAQUS analysis. This error may have caused the minor differences shown in Figure 5.10, 5.14 and 5.18. The coordinate measuring machine has its own system measurement error and this can also contribute to the minor differences although this system measurement error is relatively small.

The robot body component used in the experiment could only change its shape symmetrically in both the X-axis and the Y-axis because of the limitations of its physical structure. For example, in Figure 5.21, the robot body component should have changed to a triangular shape to match the triangular box but this could not happen in the experiment. The robot body component changed its shape symmetrically and made the shape of a circle. The robot shape change algorithm found the best shape to correspond to a "difficult" shape within the physical limitations of the robot shape change unit. The problem of dealing with difficult shapes, particularly non-symmetrical shapes, can be solved by use of a more powerful actuator and revision of the shape change mechanism itself.

It was found that the robot void shape sensor could approximately detect the box shapes. The difference between the approximate shape of the box and the actual box shape influenced the robot body shape control program to find the most appropriate shape to fit the box. Further work should be conducted to enable the robot

sensor to detect the shape of the box more accurately. For example, more sensor fingers may be installed to acquire more information on the box shape.

5.5 SUMMARY

The experimental results in this chapter show that the robot shape change system can detect the general box shape and the robot body component can change its shape symmetrically to correspond to the box as closely as practically possible. This experiment demonstrated that the robot body shape change algorithm was feasible and the control program worked correctly. For most of box shapes studied in the experiment, the robot shape change system could find the most appropriate shape from the robot body shape database to match them. The flexibility of the robot bristle may be able to deal with some mismatched areas between the box and the robot body hoop. The actual robot body component shape was measured by a Mitutoyo coordinate measuring machine and the results matched the ABAQUS calculation.

Although the current brush robot concept primarily deals with void shape, there will also be a need to accommodate void size changes. The present concept is able to deal, to some extent, with both shape change and size change by virtue of the use of long flexible bristles. Investigating traction in constricted sewer pipes shows that the long bristle approach is able to deal with constrictions up to 40% of the pipe area. The use of a multi brush, multi cylinder design is also able to deal with large voids by bridging across open spaces. Future work should include a more active system that can change both brush shape and size but at the present time the focus has been on shape change. As a look to potential future work, Figure 5.27 shows a concept

of an expandable robot body hoop, which can be used to substitute for the continuous body hoop shown in Figure 3.1 and serve as the start point of an expandable body change design study. Another concept considered is based upon a Jubilee pipe clip, which is a screw to feed additional strip metal into the robot body hoop. Another alternative is to abandon the hoop concept completely and use independent brush carriers positioned by means of servo-controlled actuators. This last idea, although attractive in many ways, would probably be too complicated and expensive for such risky operations.

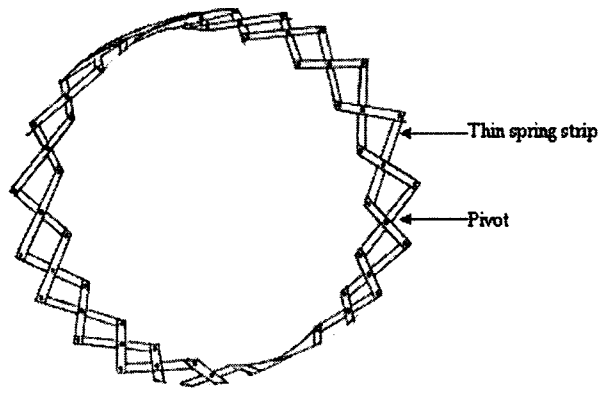

Figure 5.27: The concept of an expendable robot body hoop

CHAPTER 6

TRACTION CHANGE AFTER ROBOT BODY SHAPE CHANGE

This chapter describes an experimental investigation into bristle traction in different void shapes. Simple experiments were used to measure traction force and the results were collected, plotted and analysed. The experimental results of bristle traction force were analyzed and discussed. A mathematic model of robot bristle traction was also investigated and discussed.

6.1 ROBOT BRUSH TRACTION INVESTIGATION

6.1.1 The research strategy of traction experiments

This section of experimental work seeks to gain some understanding of the interaction of brush shape and void shape. In practice void shape will be complex and will change along the robot travel path. However, it was decided that the use of idealized representative void and brush shapes would be a useful start point for gaining this understanding.

The brush shapes investigated were based upon the potential shapes that could be generated by the robot body shape change prototype. As such the shapes of an ellipse, square, approximate square, rectangle and circle were considered. In Figure 6.1 voids in rubble were considered to approximate to six idealized geometrical shapes such as triangle, hexagon, rectangle, square and parallel boards. Correspondingly, as shown in Figure 6.2, wooden boxes of these geometrical shapes were made to simulate voids in a real environment and carry out the brush traction experiments. Voids in the real environment have more complicated shapes than the idealized geometrical shapes used here, however, these simple boxes, using regular geometrical shape, were the first approach to the problem and a useful tool to discover how the traction force changes with various shape interactions. Research of the robot body component shape change was still at the initial stage and such a simulation made the laboratory research of the interaction between brush shape and void shape possible and practical.

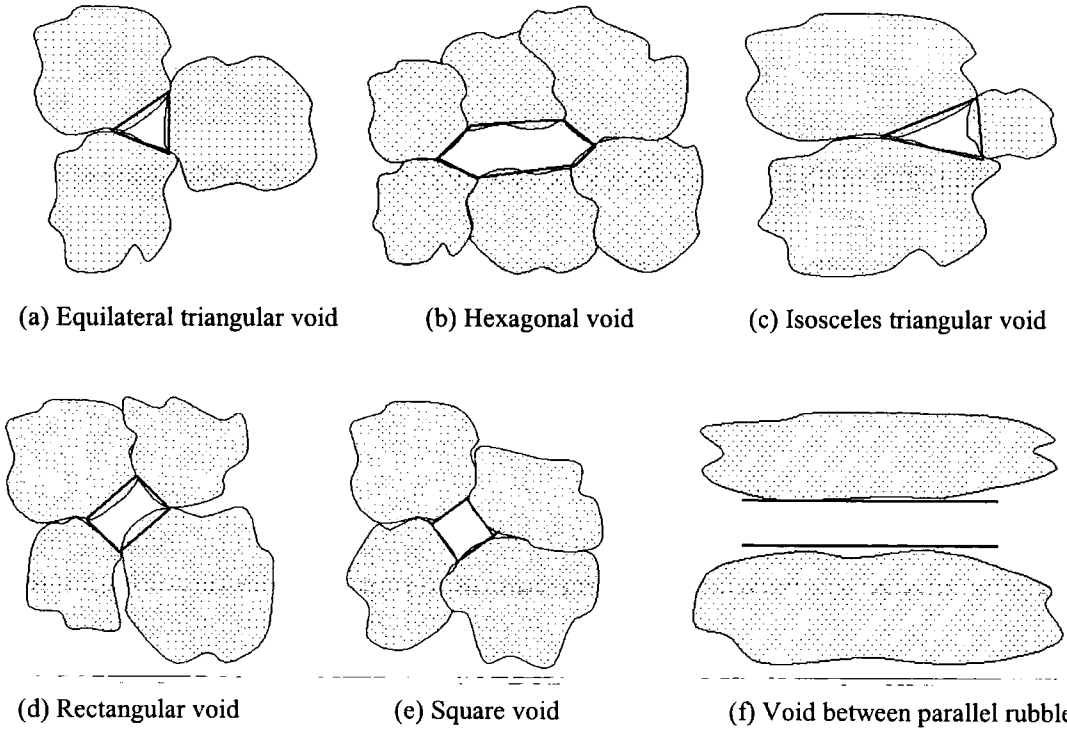

(a) Equilateral triangular void (b) Hexagonal void (c) Isosceles triangular void

(d) Rectangular void (e) Square void (f) Void between parallel rubbles

Figure 6.1: Different void shapes

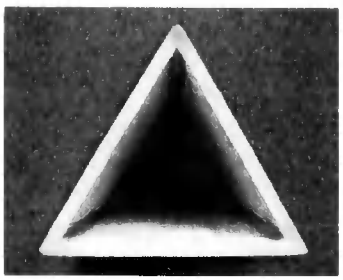

(a) Equilateral triangular box

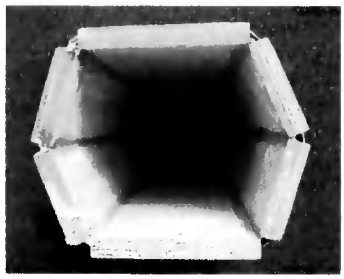

(b) Hexagonal box

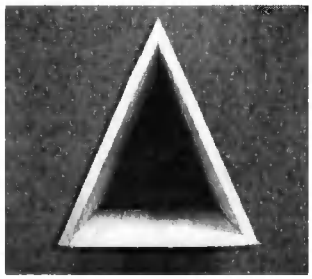

(c) Isosceles triangular box

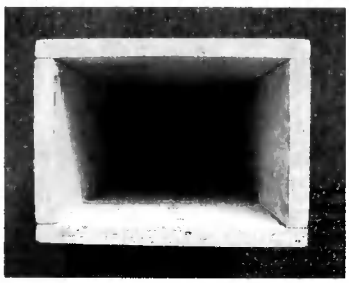

(d) Rectangular box

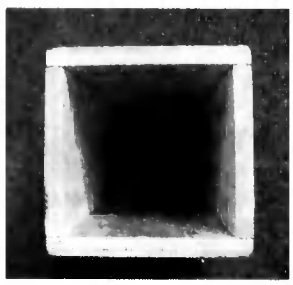

(e) Square box

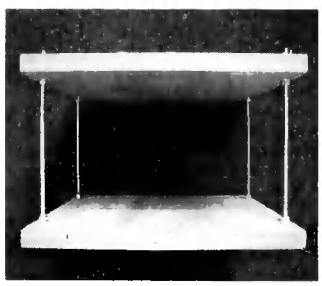

(f) Two parallel boards

Figure 6.2: Boxes of different geometrical shapes

As the robot body shape change methodology in section 3.1.3 illustrated, the robot body unit could change its shape by moving actuators inwards and outwards. Such a mechanism allowed the robot body to change to the geometrical shapes shown in Figure 6.3. Thus, fixed brush units of these geometrical shapes were made to allow the traction experiments to be carried out in the boxes shown in Figure 6.2. Brush units used in the test have the shapes shown in Figure 6.4, including (a) circular brush, (b) elliptical brush, (c) rectangular brush, (d) approximately square brush and (e) square brush. These brush units have geometrical shapes corresponding to shapes that the current robot body module could change to. In this experiment, all brush units have bristles of 8 rows, 32 holes per circumference, giving a total of 256 holes for each brush unit.

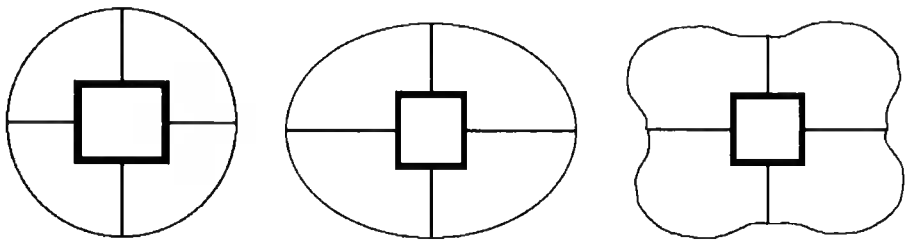

(a) Circular body (b) Elliptical body (c) Rectangular body

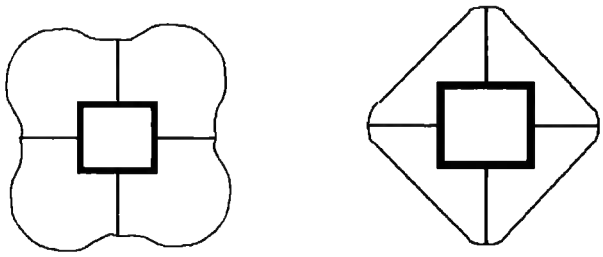

(d) Approximately square body (e) Square body

Figure 6.3: Deformed robot body in different shapes

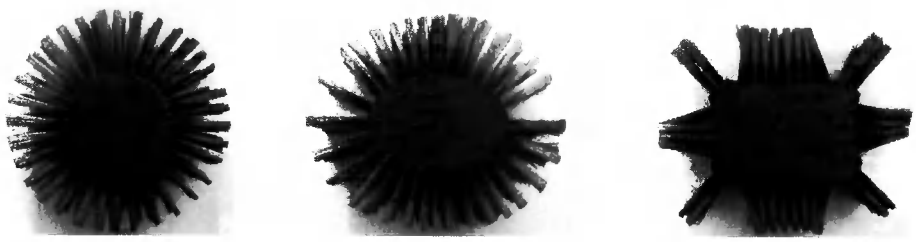

(a) Circular brush (b) Elliptical brush (c) Rectangular brush

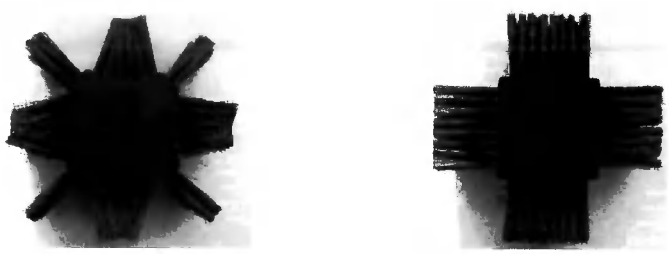

(d) Approximately square brush (e) Square brush

Figure 6.4: Brush units of different geometrical shapes

6.1.2 Introduction to traction experiment equipment

The photograph in Figure 6.5 shows the traction experiment rig layout. A "Clockhouse" compression-testing machine was used as the "platform" for the tests. As brush units were to be "pushed" through the boxes, a compression-testing machine provided an ideal platform on which tests were conducted. All tests were carried out with the machine operating at its fastest speed, 0.174 mm/s.

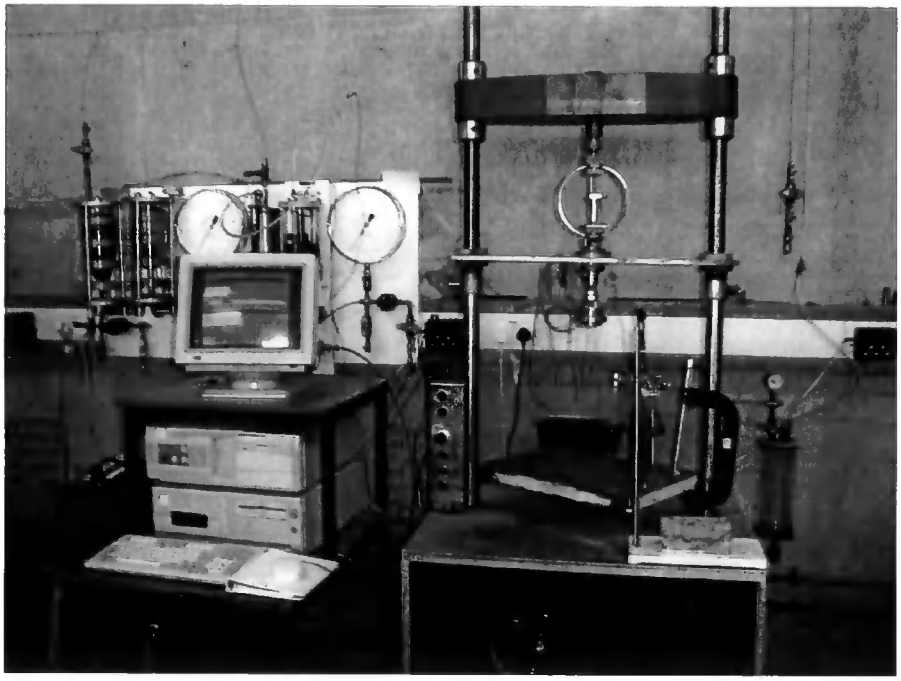

Figure 6.5: A "Clockhouse" compression-testing machine

In these tests boxes were used to simulate different shapes of voids (see Figure 6.2). In manufacture, the boxes were placed in a lathe and both ends faced off. This ensured that the axis of the box was maintained perpendicular to the loading plate of the testing machine.

Figure 6.6: A linear displacement transducer

The "Clockhouse" testing machine consisted of a machined loading plate, which was located above the lifting platform of the machine. Figure 6.6 shows the incorporation of a linear transducer with its displacement shaft contacting the loading plate. After calibration, the linear transducer provided an accurate measurement of lifting platform distance travelled. To ensure that the brush unit remained as central as possible within the box, a push plate with two pins was used, see Figure 6.7. The push plate was placed against the brush unit and two pins on the push plate located into two holes in the brush unit, which stopped the rotation of the brush unit. The distance between the two holes is the same as the distance between the two pins on the push plate and the holes are symmetrical about the central axis of the brush core. The two pins were also symmetrical about the central axis of the push plate. The push plate was attached to a steel shaft, which ran inside an axial bearing housing on the compression-testing machine. The bearing housing ensured that the push plate pushed the brush unit as centrally as possible but would allow rotation. However, no significant rotation was observed. The bearing housing was integrated into the cross-

brace support of the compression-testing machine. The diagram in Figure 6.8 illustrates the structure and use of the experimental equipment.

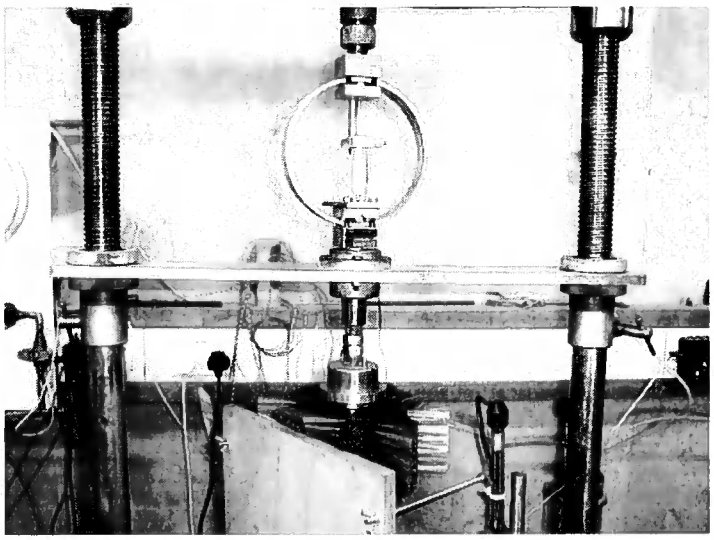

Figure 6.7: Test set up

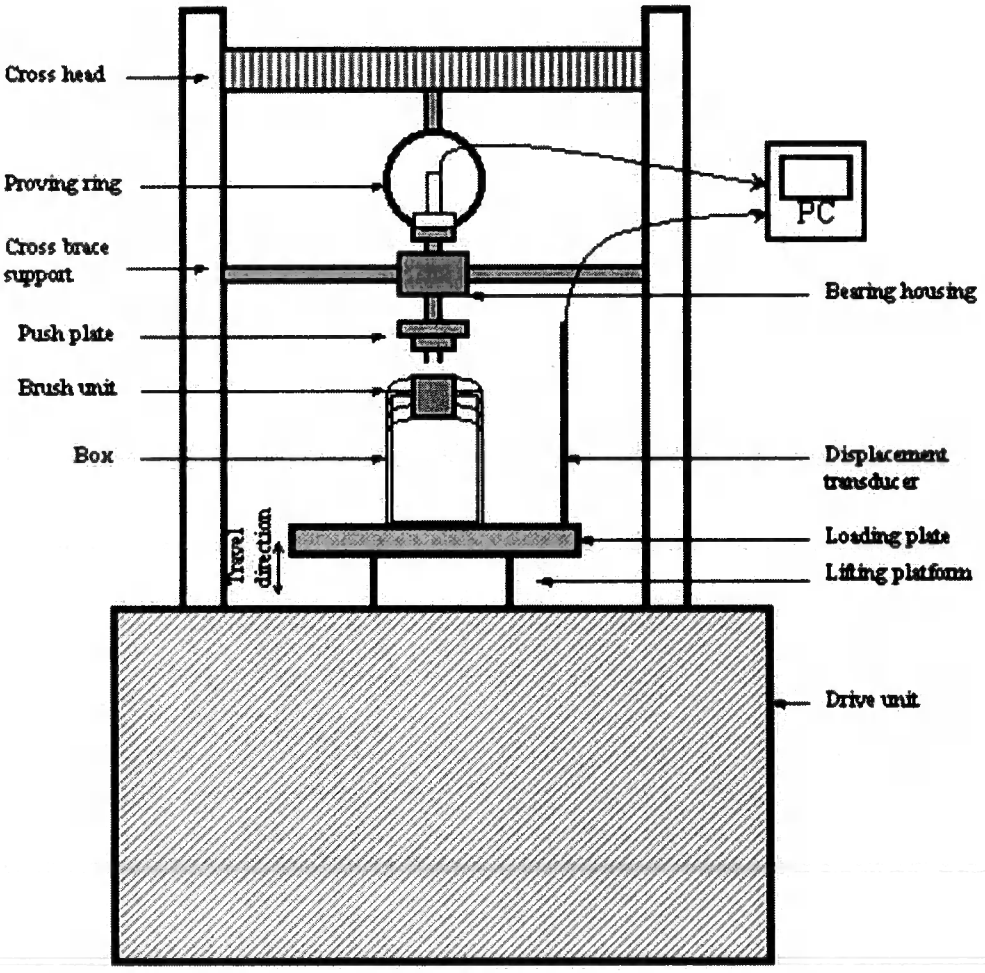

Figure 6.8: Bristle traction force experiment

Traction forces were measured by a proving ring. Prior to beginning the experiments, both the proving ring and displacement transducer were calibrated. The two rings used for testing were a 200kg (force, 1960N) ring (No.2667-transducer: 0.04645kg/mv) and a 1000kg (force, 9800N) ring (No.2380-transducer: 0.2209kg/mv). A PC was connected to the linear displacement transducer and the proving ring via cables. Software TRIAX (Toll, D., 1993) running on the PC collected and recorded signals from the transducers.

The operation of the experiments took the following steps:

After the brush unit had been located into position, the machine was switched on. The lifting platform was then raised; this consequently raised the box, which was located on the loading plate. The top of the proving ring contacted the large cast iron reaction support. As the brush unit touched the top of the box, the brush unit bristles deflected. This was the point at which the brush began to be inserted into the box. As the test continued and the brush unit became fully inserted into the box, the force required to push the brush unit forward and the travel displacement of the brush unit was recorded.

The lifting platform of the compression-testing machine was then lowered and the box was inverted, while the brush unit remained inside. The above experiment was then repeated, however, this time, the brush unit was forced to reverse. The transducer and proving ring signal were collected and recorded by using the software TRIAX. Subsequently, the force exerted was plotted against the vertical displacement of the brush unit.

6.1.3 Brush unit forward traction experiments

To investigate the interaction between the changed robot body component and void wall, brush units with different shapes were produced. In the test, wooden boxes of different geometrical shapes were made to simulate various voids in a real environment. In this work, comparisons are made between the performances of different shaped brushes in different shaped boxes. This work considers particular comparisons using brush shapes that are subjectively selected but obviously of interest. That is, a comparison is made of brush units tested in boxes, which have a reasonably similar shape to the brush unit, have reasonable contact surfaces with the brush unit and have reasonable active bristle numbers and relatively small annular gaps between the box and brush units. Table 6.1 was used to illustrate the decision process of selecting combinations of box shape and brush shape. Those combinations categorized as exact match, approximate match and less approximate match, were chosen to be used in the traction force experiments for the reasons described above.

The combination of box shape and brush shape		Box shape				
		Rectangular	Square	Two Parallel Boards	Isosceles Triangular	Equilateral Triangular
Brush shape	Rectangular	X	O	+	++	O
	Square	+	X	+	O	O
	Approximate Square	+	+	+	O	++
	Circular	++	+	++	O	+
	Elliptical	+	O	++	++	O
Note		X: Exact match +: Approximate match ++: Less approximate match O: Poor match				

Table 6.1: The combination of box shape and brush shape

Other combinations were not chosen for traction experiments. For example, a circular brush, a square brush and an approximately square brush are geometrically similar to a square box and thus have reasonable contact areas with the square box. However, an elliptical brush in a square box will not behave in a similar manner because it has a much smaller area contact. So, the elliptical brush in a square box was not chosen for the test program. After the main experimental program, an additional combination was considered by the introduction of a hexagonal box used in combination with an elliptical brush. This combination was selected because of the particular geometrical shape compatibility. Hence, a total of 18 combinations were selected for traction tests in this work. At this starting stage of the research, these combinations were considered to be representative of the interactions of brush units in different shape boxes. The following test combinations were investigated for this purpose:

- An elliptical brush unit tested between two parallel boards (Ein2b)
- An elliptical brush unit tested in a rectangular box (Einrect)
- An elliptical brush unit tested in a hexagonal box (Einhex)
- An elliptical brush unit tested in an isosceles triangular box (Einbigtri)
- A square brush unit tested in a square box (Sins)
- A square brush unit tested in a rectangular box (Sinrect)
- A square brush unit tested between two parallel boards (Sin2b)
- A circular brush unit tested in an equilateral triangular box (Cintri)
- A circular brush unit tested in a square box (Cins)
- A circular brush unit tested in a rectangular box (Cinrect)
- A circular brush unit tested between two parallel boards (Cin2b)
- A rectangular brush unit tested in a rectangular box (Rinrect)

- A rectangular brush unit tested in an isosceles triangular box (Rinbigtri)
- A rectangular brush unit tested between two parallel boards (Rin2b)
- An approximately square brush unit tested in a square box (ASins)
- An approximately square brush unit tested in a rectangular box (ASinrect)
- An approximately square brush unit tested in an equilateral triangular box (ASintri)
- An approximately square brush unit tested between two parallel boards (ASin2b)

All test results were recorded and plotted giving traction force against brush unit vertical displacement, as shown in Figure 6.9 (1)-(18). Each test was repeated three times; the points shown in the graph and the solid line is the average value curve. The test results of different brush units tested in the same box were plotted to compare their forward traction forces, as seen in Figure 6.10 (a)-(e).

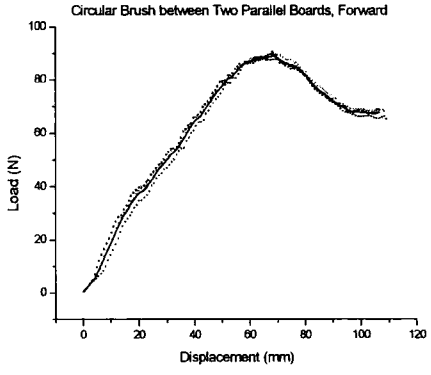

(1)

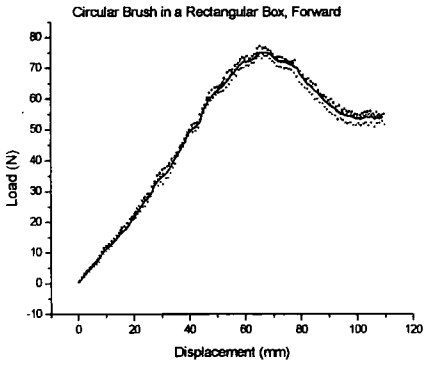

(2)

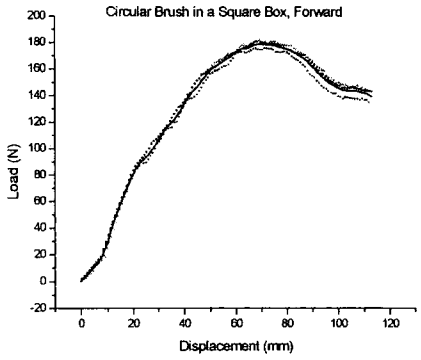
Circular Brush in a Square Box, Forward
Load (N)
Displacement (mm)

(3)

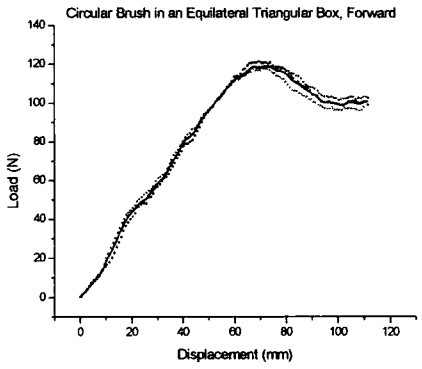
Circular Brush in an Equilateral Triangular Box, Forward
Load (N)
Displacement (mm)

(4)

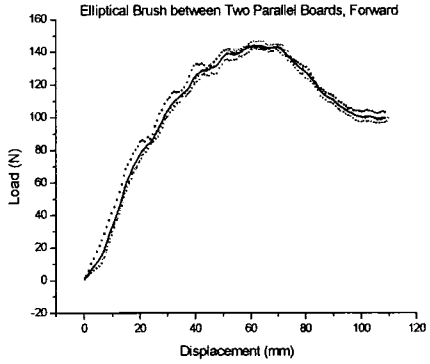
Elliptical Brush between Two Parallel Boards, Forward
Load (N)
Displacement (mm)

(5)

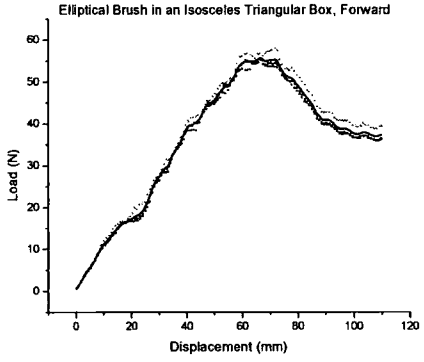
Elliptical Brush in an Isosceles Triangular Box, Forward
Load (N)
Displacement (mm)

(6)

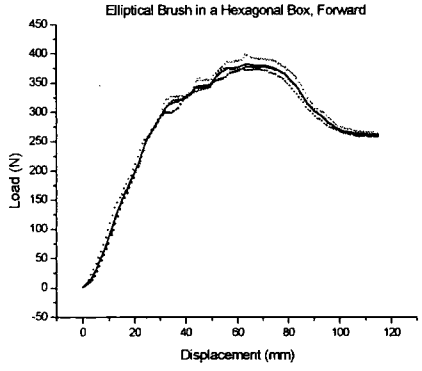
Elliptical Brush in a Hexagonal Box, Forward
Load (N)
Displacement (mm)

(7)

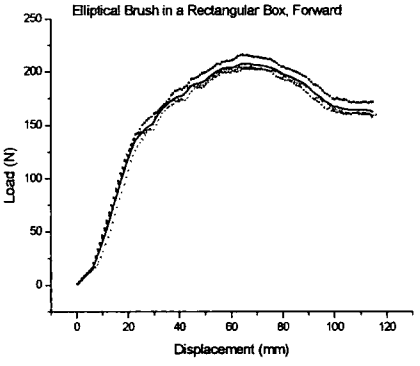
Elliptical Brush in a Rectangular Box, Forward
Load (N)
Displacement (mm)

(8)

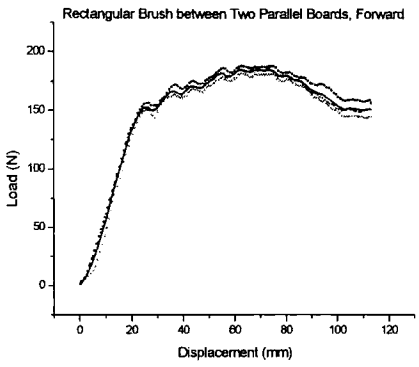

(9)

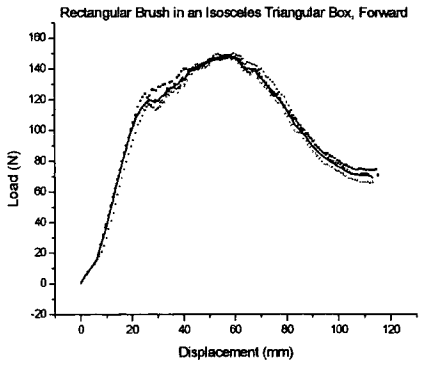

(10)

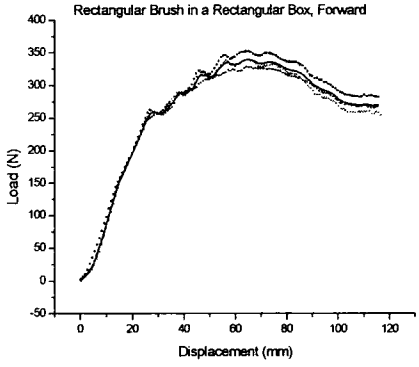

(11)

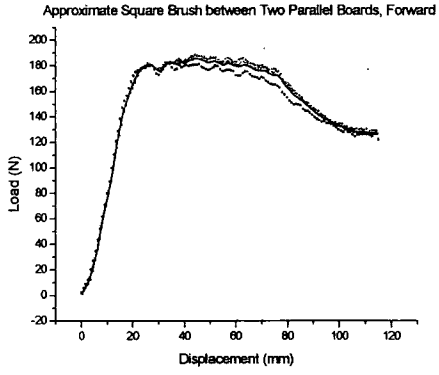

(12)

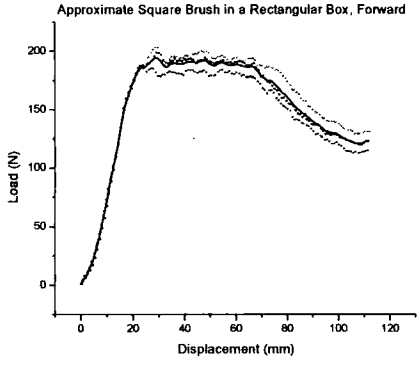

(13)

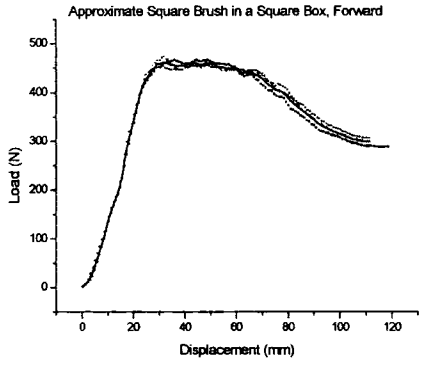

(14)

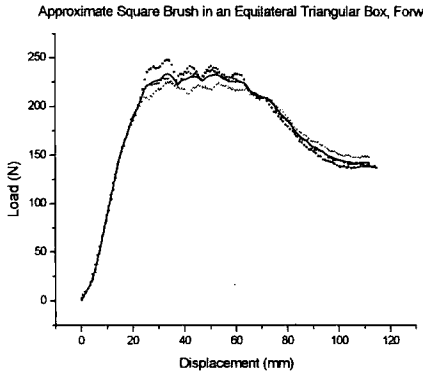

(15)

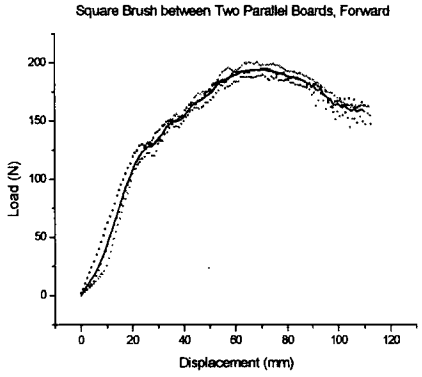

(16)

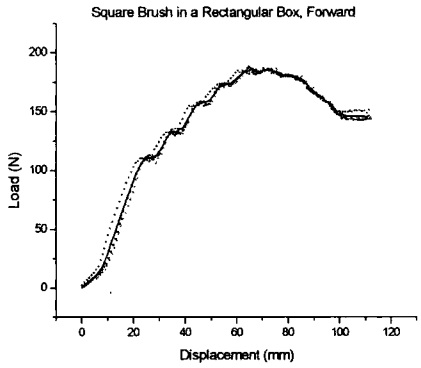

(17)

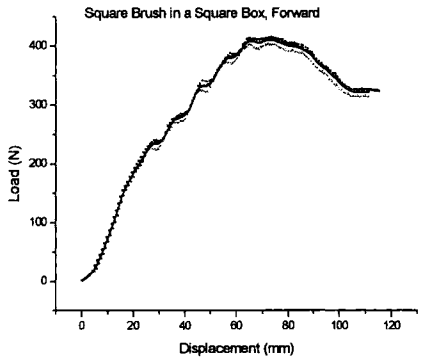

(18)

Figure 6.9: Brush unit forward traction experiment plots

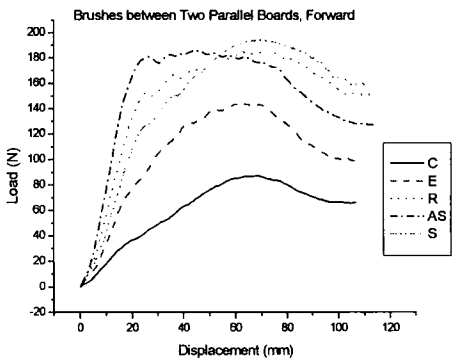

(a)

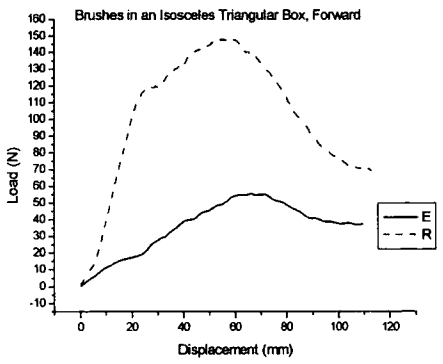

(b)

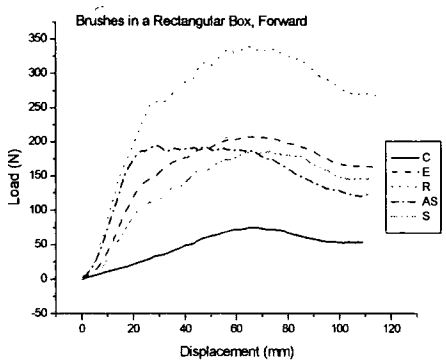

(c)

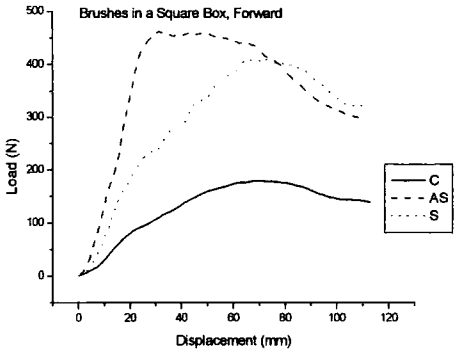

(d)

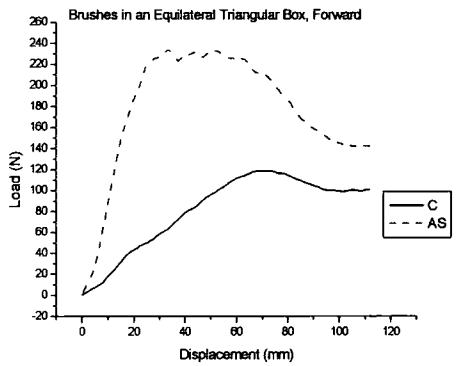

(e)

Figure 6.10: Comparison of brush unit forward traction experiment plots

(Note: C: circle, E: ellipse, R: rectangle, AS: approximate square, S: square)

6.1.4 Brush unit reverse traction experiments

Similar to the tests described in the section above, all brush units were also subjected to a reverse traction test. Due to the large forces involved in the reverse traction test, a 1000kg (force, 9800N) proving ring (No.2380-transducer: 0.2209kg/mv) was chosen for the reverse test. The test procedure was the same as the forward traction test; all signals from the linear displacement transducer and the proving ring were recorded and then plotted as traction force against brush unit vertical

displacement. Plots are shown in Figure 6.11 (1)-(18). The test results for different brush units tested in the same box were plotted in one graph to compare their reverse traction forces as shown in Figure 6.12 (a)-(e).

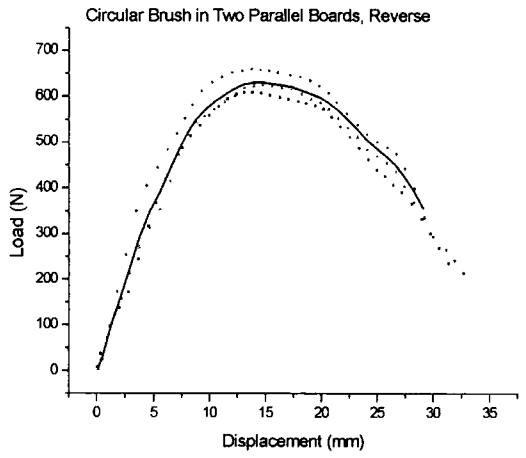

(1)

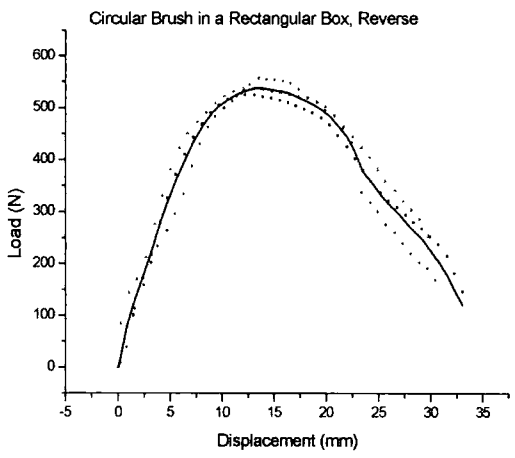

(2)

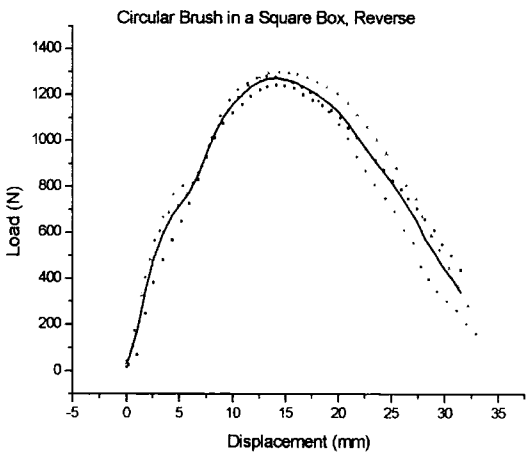

(3)

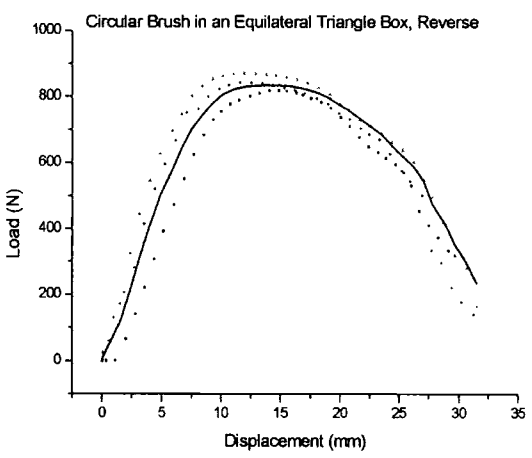

(4)

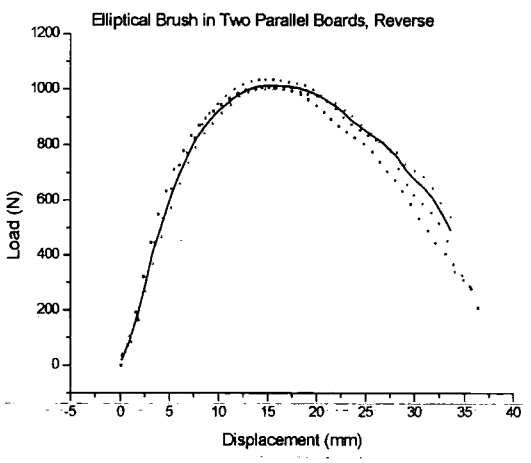

(5)

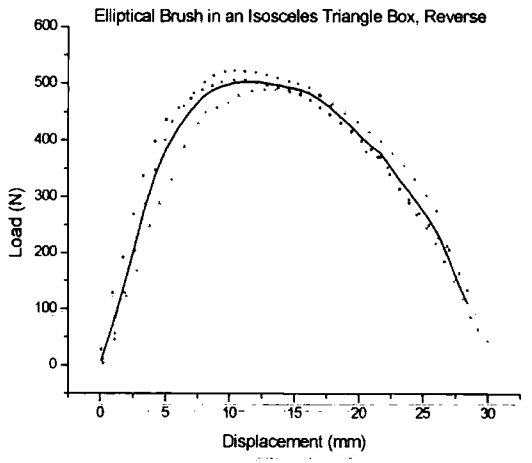

(6)

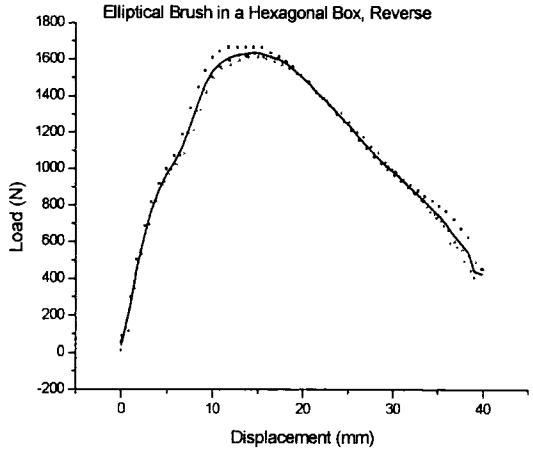
Elliptical Brush in a Hexagonal Box, Reverse
Load (N)
Displacement (mm)

(7)

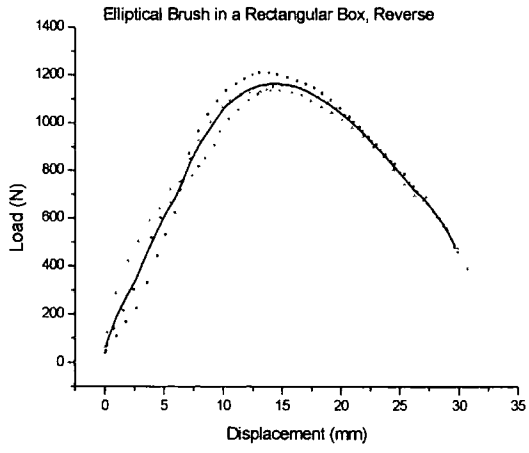
Elliptical Brush in a Rectangular Box, Reverse
Load (N)
Displacement (mm)

(8)

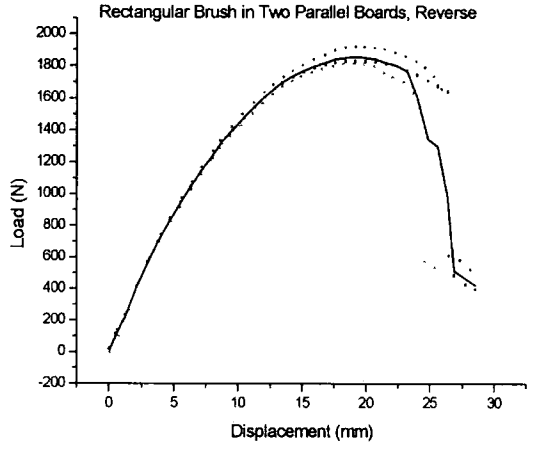
Rectangular Brush in Two Parallel Boards, Reverse
Load (N)
Displacement (mm)

(9)

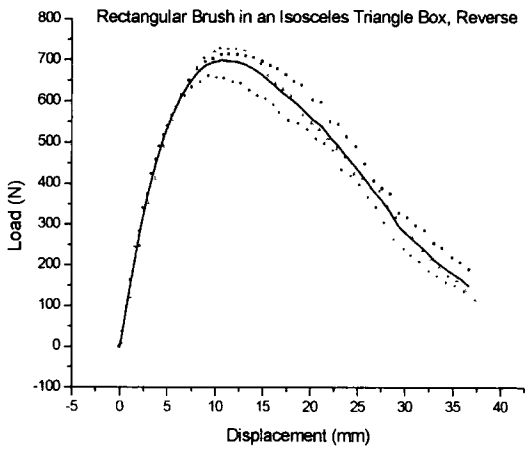
Rectangular Brush in an Isosceles Triangle Box, Reverse
Load (N)
Displacement (mm)

(10)

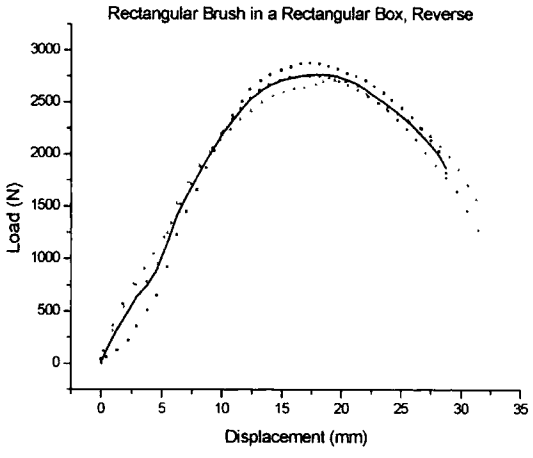
Rectangular Brush in a Rectangular Box, Reverse
Load (N)
Displacement (mm)

(11)

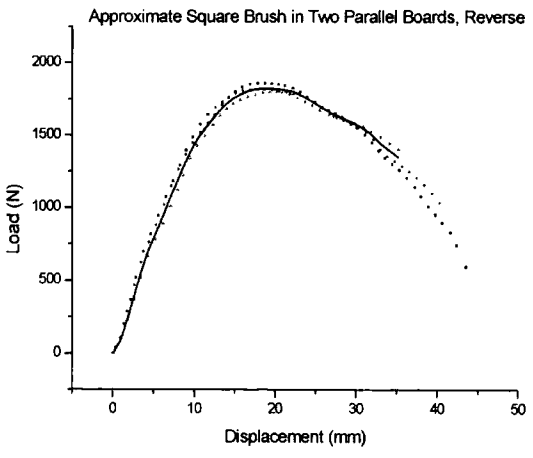
Approximate Square Brush in Two Parallel Boards, Reverse
Load (N)
Displacement (mm)

(12)

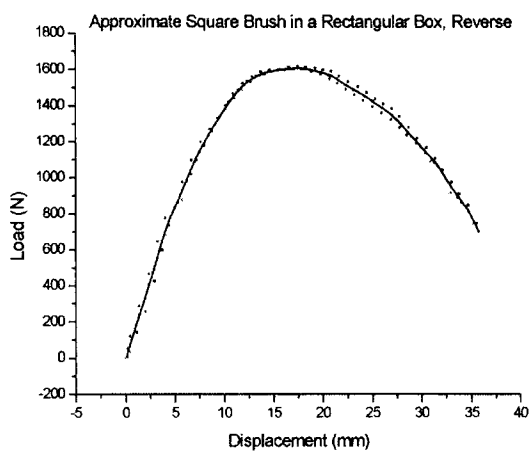

(13)

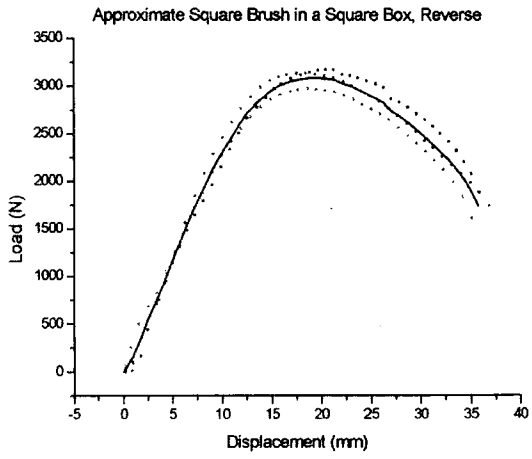

(14)

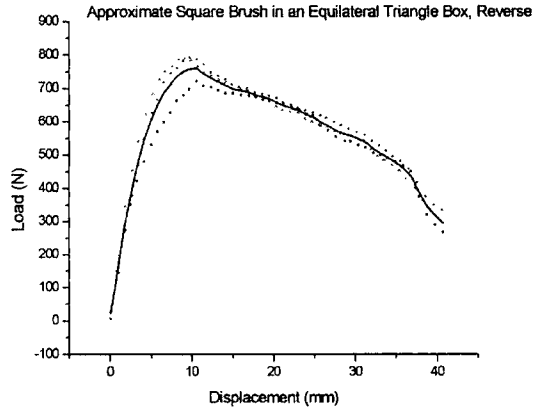

(15)

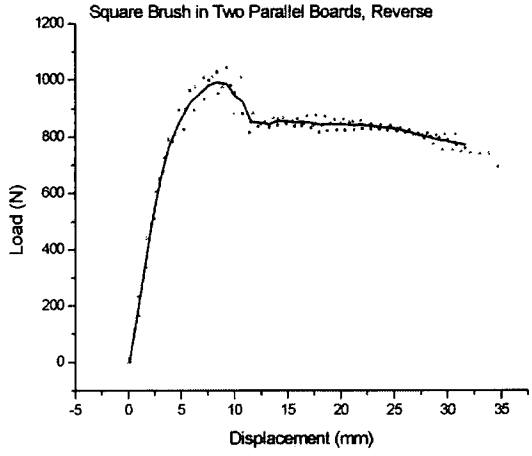

(16)

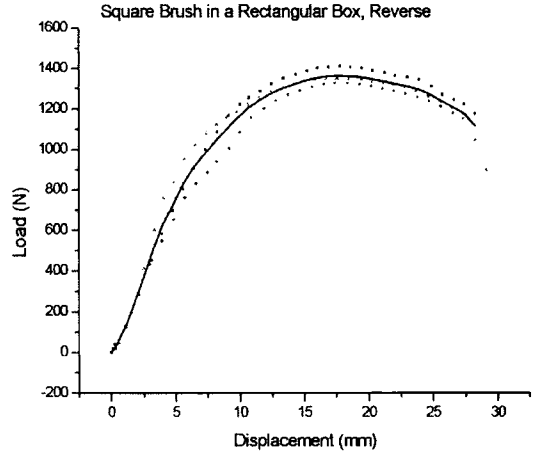

(17)

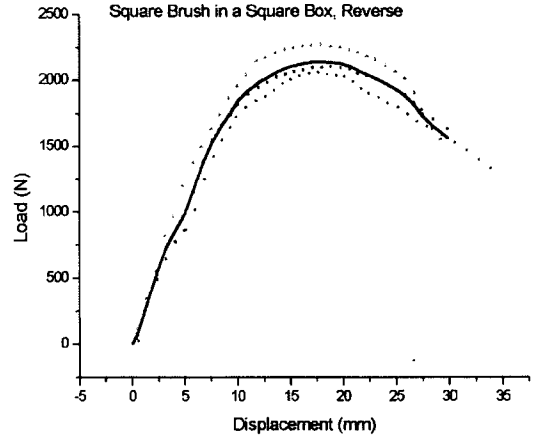

(18)

Figure 6.11: Brush unit reverse traction experiment plots

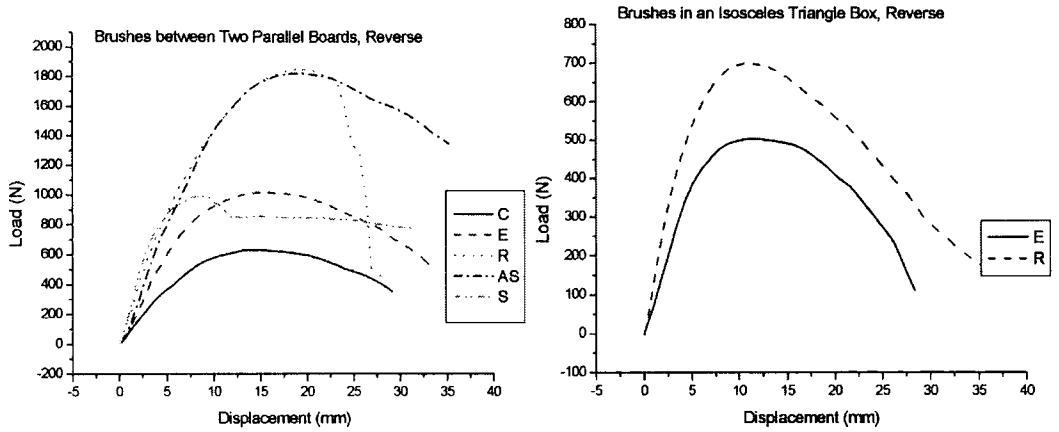

(a)

(b)

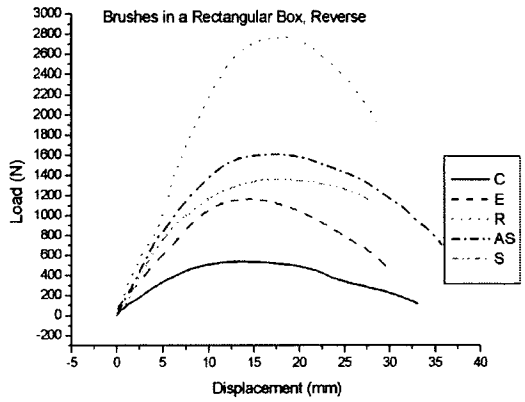

(c)

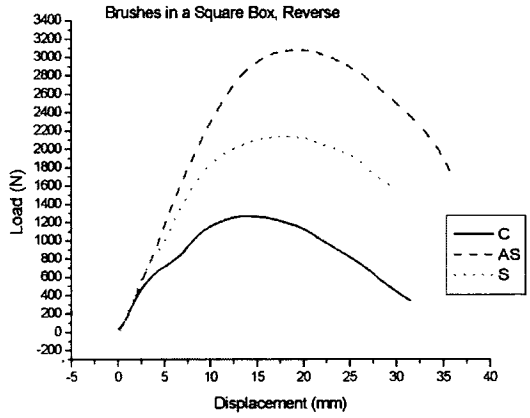

(d)

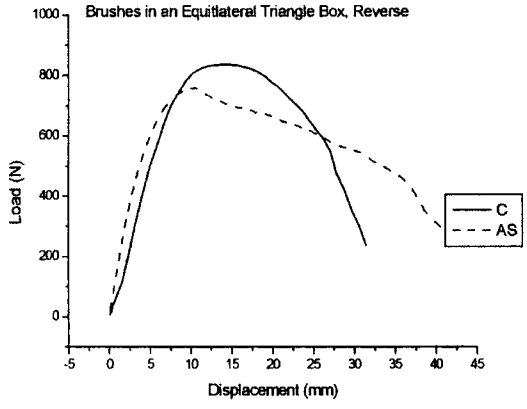

(e)

Figure 6.12: Comparison of brush unit reverse traction experiment plots

(Note: C: circle, E: ellipse, R: rectangle, AS: approximate square, S: square)

6.2 DISCUSSION OF BRUSH UNIT TRACTION EXPERIMENTS

For both forward traction experiments and reverse traction experiments, every experiment was repeated three times and the software ORIGIN was used to plot the results of each experiment. In each graph (Figure 6.9 and Figure 6.11), the individual experimental results were plotted using different line types. Then, the software carried out a curve fitting operation on each plot and then plotted the overall average curve. The average curve is shown as the solid black line in the graphs.

6.2.1 Observations for the brush unit forward traction experiments

The plots in Figure 6.9 show how the forward traction forces changed when the brush units were pushed through the boxes. All plots of the forward traction experiment results are of a similar shape, whatever the brush unit. That is, in a forward traction experiment the forward traction force curve rises up and gets to a maximum point, which is the peak loading force. The force then falls gradually to a stable value, which is the steady forward force. For a traction experiment in a box of any particular geometrical shape, a large forward traction force may be produced if a brush unit has a similar shape to that of the box and a large contact area with the box.

For all brush units tested between two parallel boards, from the plots in Figure 6.9 (1), (5), (9), (12), (16), it can be seen that a square brush unit, an approximately square brush unit and a rectangular brush unit achieved larger forward forces than a circular or elliptical brush unit because of their larger contact area with the board surface and therefore more bristles in operation. The square brush achieved a larger

forward force than the approximately square brush although they had the same amount of active bristles. This was because some bristles of the approximately square brush are inclined with the board surface and the degree of deformation of these bristles was smaller than that of the square brush.

For all brush units tested in a rectangular box, a rectangular brush unit achieved the largest forward force because the rectangular brush unit had a larger contact area with the rectangular box and more active bristles than other brush units. The plots are shown in Figure 6.9 (2), (8), (11), (13) and (17).

For brush units tested in a square box, an approximately square brush unit and a square brush unit achieved a larger forward force than a circular brush unit as shown in the plots in Figure 6.9 (3), (14) and (18). This was due to a larger contact area with the box wall and the subsequent increase in active bristles compared to the circular brush unit.

For brush units tested in an equilateral triangular box, an approximately square brush unit achieved a larger forward force than a circular brush unit, as shown in the plots in Figure 6.9 (4), (15). This is because the approximately square brush unit has a bigger contact area with the box and more active bristles than the circular brush.

For brush units tested in an isosceles triangular box, a rectangular brush unit achieved a larger forward force than an elliptical brush unit, because the rectangular brush unit has a bigger contact surface with the box and more active bristles than the elliptical brush unit. Plots are shown in Figure 6.9 (6), (10).

To conclude, it was found that forward traction force is influenced by brush unit contact area with the box wall, the number of active bristles and the degree of deformation of the bristles. A bigger contact area with the box wall and more active bristles lead to a larger forward force.

6.2.2 Observations for the brush unit reverse traction experiments

In the reverse traction experiments, the traction force curve rises up sharply to a maximum point, which is called the peak reverse force, and then falls quickly. The following section 6.2.3 gives an explanation for this observation in terms of strut buckling theory. Similar to the forward traction experiments, a large reverse traction force can be produced in a reverse traction experiment if a brush unit has a large contact area with the box and more active bristles.

For all brush units tested between two parallel boards, the approximately square brush unit and the rectangular brush unit achieved a large peak reverse force. The rectangular brush unit performed only slightly better than the approximately square brush unit as shown in Figure 6.11 (9) and (12). For the reverse traction experiments in a rectangular box, the plots show that the rectangular brush unit can achieve a much larger peak reverse force than the other brushes. For the reverse traction experiments in a square box, the approximately square brush unit can achieve a larger peak reverse force than the other brush units. For brush units in an equilateral triangular box, the circular brush unit and the approximately square brush unit produce a similar peak reverse force. For the reverse traction experiments in an

isosceles triangular box, it can be concluded from the plots that a rectangular brush unit produces a larger peak reverse force than an elliptical brush unit.

From all of the traction experiments, a brush unit, which can achieve the largest forward traction force and reverse traction force, normally has a similar outline shape to the box and hence a good contact with the box and more active bristles. There are other factors which also influence the traction force. These factors will be discussed in detail in section 6.2.4. Based on the traction experimental results, it was observed that the following combinations could produce both a large forward traction force and a large reverse traction force.

- A rectangular brush unit in a rectangular box
- An approximately square brush unit in a square box
- A rectangular brush unit in an isosceles triangular box
- A rectangular brush unit between two parallel boards
- An elliptical brush unit in a hexagonal box
- An approximately square brush in an equilateral triangular box

6.2.3 Analysis of traction force plots

This section gives an analysis of the reverse traction force plots. It is noted in all cases that reverse traction force curves rise up sharply to a peak point and then fall quickly. In a reverse traction experiment shown in Figure 6.13, one end of the bristle is fixed on the brush unit core and the other end of the bristle contacts the surface of the box wall. A bristle can be considered as a slender strut, that is, a compression member, which is long compared to its cross-sectional area. Buckling theory suggests

that such a member will fail due to buckling before the direct compressive stress reaches the yield point. Euler theory considers the axial load required to buckle a strut but the limitation to apply Euler is that the strut needs to be initially straight. Additionally, the load needs to be applied axially and the material needs to be homogenous. However, buckling theory does provide a useful insight into how a bristle behaves under different constraint conditions. Euler theory includes four different constraint modes (Ryder, G., 1965):

1. Strut with both ends pinned.
2. Strut with one end fixed and one end free.
3. Strut with both ends fixed.
4. Strut with one end fixed and one end pinned.

Two of these modes are applicable to the brush mechanism. Euler theory states that,

$$P = \frac{K\pi^2 EI}{l^2} \tag{6.1}$$

where P = Buckling load, E = Young's modulus, K = Constant dependent on the mode of buckling.

In the reverse traction experiment, the brush unit is subjected to a reverse force and is thus in its gripping mode. Two planes are defined for the following description as shown in Figure 6.13. Plane A is a transverse plane of the brush core and is along the axis of the brush core. Plane B is a perpendicular plane to the axis of the brush core. In the reverse traction experiments, the brush units tended to behave in two different ways, depending on the experimental conditions. One tendency is that the brush core rotates in plane B, perpendicular to the brush axis, and bristles rotate out of the transverse plane A. This happens to the circular brush unit and the elliptical brush

unit. The Euler theory mode corresponding to this case is mode 2, in which "Strut with one end fixed and one end free" and for this mode $K = 0.25$ in equation (6.1) (Ryder, G., 1965). The other tendency is that the bristles buckle in the transverse plane A of the brush core. The brush core does not rotate or translate in plane B. Buckling only in plane A happens to the rectangular brush in the rectangular box and square brushes in the square box. The Euler theory model corresponding to these cases is mode 4, in which "Strut with one end fixed and one end pinned" and for this mode $K = 2.05$ in equation (6.1) (Ryder, G., 1965). For these two different modes, it can be seen that a higher reversal load can be obtained when the brush unit is not allowed to rotate or translate in the box.

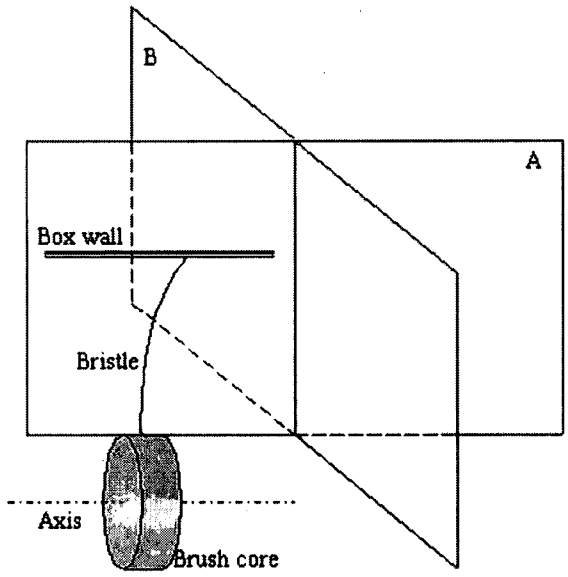

Figure 6.13: Transverse plane and perpendicular plane of brush core

In the reverse traction experiment, the travel speed of the brush unit was slow and hence the bristles of the brush unit experienced the following process. Reference to Figure 6.14, the stage OA of the curve shows that the bristles have no sign of slipping and are in the gripping mode when the reverse traction experiment starts. The traction force increases sharply and the deformation of the bristles is relatively small.

Stage AB of the curve shows that the increase of the bristle traction force slows down and bristles begin to show the tendency to collapse. The deformation of the bristles becomes larger at this stage. At the point B, the traction force reaches a peak value and bristles begin to collapse due to the failure of the buckling, which is an instability condition. In stage BC, single bristle collapses quickly and the traction force decreases sharply. The gradient of the curve at this stage is dependent upon the test conditions. The gradient of the curve has little meaning because it follows an instability condition and is test dependent. In the traction experiment, the bristles of the brush unit are in different shapes and the buckling collapse of each bristle is not synchronized, so the collapse process for all bristles appears to be longer and slower than the single bristle.

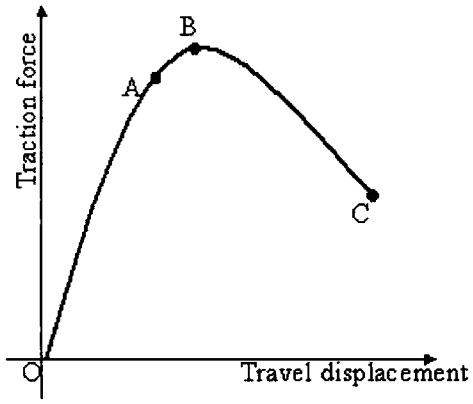

Figure 6.14: The traction force changes in the reverse traction experiment

6.2.4 Factors influencing traction force

Traction forces for brush units applied to the different boxes were considered to be influenced by several factors described as follows:

1. Number of bristles in operation

(1) Active bristle number

Bristles may be considered to be active or inactive. A bristle contacting the box wall is considered as "active". If more bristles are active, both the forward traction force and the reverse traction force will increase.

(2) The contact area between the brush unit and the box wall

If a brush unit has a large contact area with the box wall, more bristles will be in contact with the box wall. Therefore, both a large forward traction force and a large reverse traction force will be produced.

2. Effectiveness of bristles in operation

(1) The shape of the bristle

The shape of the bristle has a significant influence on the reverse traction force. The work of Stutchbury (Stutchbury, N., 1999) and Han (Han, C., 1999) suggests that an optimum reverse traction force can be achieved if the bristle is in an optimum shape that is the bristle tip forms a particular angle with the box wall. The angle is influenced by various factors such as bristle material and friction factor. The forward traction force is influenced by the degree of bristle deformation. A large degree of bristle deformation will produce a large forward traction force.

(2) Sloping contact surface

If bristles contact a sloping surface, the inclination of the contact surface relative to the bristle direction will influence the traction force. If bristles interact with the sloping box surface, reverse traction force will decrease. By way of example, a circular brush is tested in a triangular box, as illustrated in Figure 6.15. This figure shows three sample bristles that contact the box wall. Bristle B contacts the wall and the bristle tip will grip the wall in the usual manner. However, bristle A and C will not grip the surface effectively and will simply splay out. This behaviour will be

dependent upon the bristle stiffness, the curvature of the bristle, the friction condition and the relative slope of the box surface. Therefore, the sloping box surface does not allow the bristles to grip effectively and the reverse traction force is decreased. If the brush shape geometrically matches the box shape better, there will be fewer bristles interacting with sloping box surface and thus a larger reverse traction force can be produced.

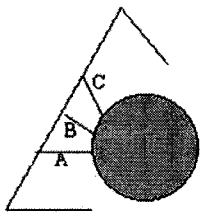

Figure 6.15: Bristles interact with a sloping box surface

3. The ability of bristles to withstand buckling

An important way of increasing reverse traction force without increasing forward traction force is to constrain the bristles so that their individual buckling forces are increased without increasing their beam deflection properties.

(1) X-PLY mechanism

The interaction between bristles and box surfaces is a complicated phenomenon. Rotation and translation of brush cores were found in some traction experiments. By way of example, if a circular brush is subjected to a reverse force in a square box and in its gripping mode, the circular brush may rotate as shown in Figure 6.16 (a). If a square brush is subjected to a reverse force between two parallel boards, the square brush may experience transverse translation as shown in Figure 6.17 (a). The distribution and status of bristles of brush units can influence the interaction between the bristles and the contact surface. An X-PLY mechanism means that the bristles are crossed like an "X". The bristles of the approximately square brush unit

and rectangular brush unit naturally form the X-PLY mechanism, as shown in Figure 6.4 (c) and (d). The X-PLY mechanism can help to prevent the brush core from rotating and translating, and hence enables the bristles to grip the box wall more tightly and effectively increases the reverse traction force. The X-PLY mechanism can help to stop the rotation of a circular brush unit as shown in Figure 6.16 (b) and the transverse translation of a square brush unit as shown in Figure 6.17 (b).

(a) The rotation of a circular brush in a square box (b) X-PLY mechanism stops the rotation

Figure 6.16: Circular brush with different bristle mechanisms in a square box

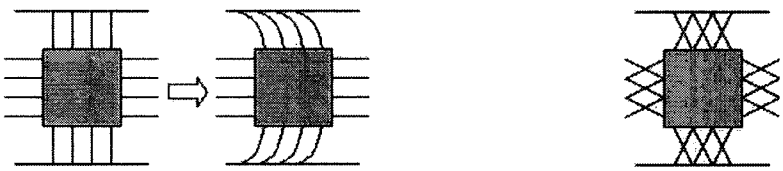

(a) The transverse translation of a square brush (b) X-PLY mechanism stops the translation

Figure 6.17: Square brush with different bristle mechanisms between two parallel boards

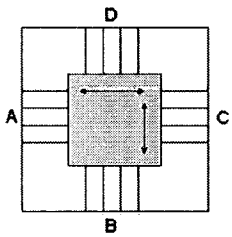

Figure 6.18: The interaction between the square brush unit and the square box

(2) The particular interaction and shape match between the brush unit and the box

The particular interaction and shape match between the brush unit and the box may also help to prevent the brush unit from rotating and translating. If a square brush

unit is tested in a square box as shown in Figure 6.18, bristles on the part A and C contact the box wall and their support against the box wall will prevent the translation of the square brush along the direction AC. Similarly, bristles on the part B and D contact the box wall and their support against the box wall will prevent the translation of the square brush along the direction BD. Thus, no rotation and translation will take place in this case.

6.2.5 The ratio of reverse traction force and forward traction force

In a good brush system design the robot should experience a low forward traction force but be able to withstand a high reverse traction force. This helps the sliding brush unit to go forward easily and the gripping brush unit to have a sufficiently large force to avoid slipping back or reversal. So, the ratio of the reverse traction force to the forward traction force reflects the drive performance of the robot. In the brush robot design, it is desirable that the ratio should be as high as possible.

Traction Test	The ratio of reverse force and forward force
A circular brush unit tested between two parallel boards	7:1
A circular brush unit tested in a rectangular box	7:1
A circular brush unit tested in a square box	7:1
A circular brush unit tested in an equilateral triangular box	7:1
An elliptical brush unit tested between two parallel boards	7:1
An elliptical brush unit tested in an isosceles triangular box	8:1
An elliptical brush unit tested in a hexagonal box	4:1
An elliptical brush unit tested in a rectangular box	6:1
A rectangular brush unit tested between two parallel boards	10:1
A rectangular brush unit tested in an isosceles triangular box	5:1
A rectangular brush unit tested in a rectangular box	8:1
An approximately square unit tested between two parallel boards	9:1
An approximately square unit tested in a rectangular box	9:1
An approximately square unit tested in a square box	7:1
An approximately square unit tested in an equilateral triangular box	3:1
A square brush unit tested between two parallel boards	5:1
A square brush unit tested in a rectangular box	7:1
A square brush unit tested in a square box	5:1

Table 6.2: The ratio of reverse traction force and forward traction force

To investigate the traction performance of different brush units in different boxes, the ratio of the reverse traction force and forward traction force was calculated and shown in Table 6.2. In the table, an approximately square unit tested in an equilateral triangular box has the lowest ratio but a rectangular brush unit tested between two parallel boards had the highest ratio.

There are several factors that influence these ratios, for example, the X-PLY mechanism, the active bristle number, the effectiveness of bristles in operation and the ability of bristles to withstand buckling, etc. It can be seen in Table 6.2 that:

For the cases of a rectangular brush unit tested between two parallel boards and an approximately square brush unit tested in a rectangular box or between two parallel boards, as shown in Figure 6.19 (a), (b), (c), the ratio of reverse traction force and forward traction force is the highest at about 9:1. If X-PLY bristles interact with flat surfaces, the ratio of reverse traction force and forward traction force will increase. This is caused by several factors. Firstly, the bristles of an approximately square brush or a rectangular brush naturally form the X-PLY mechanism and at the contact with flat surfaces. The X-PLY mechanism prevents brush units from rotating and translating, causing them to grip the box tightly and effectively increase the reverse traction force. Secondly, for these cases, brush units have large areas of contact with the box walls. More active bristles are in operation. These cases have two or four regions of bristle interaction with the box surfaces as shown in Figure 6.19 (a), (b), (c). These active bristles also exhibit the X-PLY mechanism. Thus, large reverse traction forces can be produced. Thirdly, bristles in these cases contact with the flat non-sloping surfaces, so the bristles can grip the contact surface effectively and hence increase the ratio.

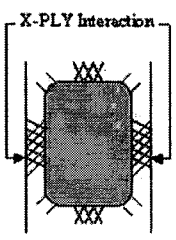

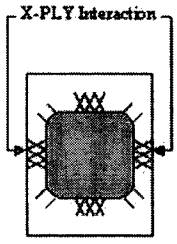

(a) Rectangular brush between two parallel boards (b) Approximately square brush in a rectangular box

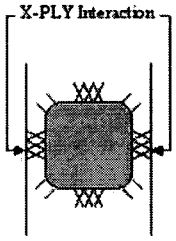

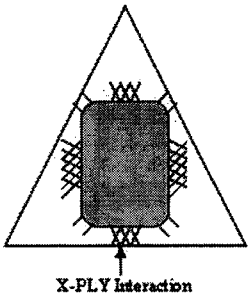

(c) Approximately square brush between two parallel boards (d) Rectangular brush in an isosceles triangular box

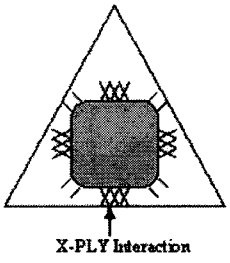

(e) Approximately square brush in an equilateral triangular box

Figure 6.19: Traction tests of brushes with X-PLY mechanism

If an approximately square brush unit is tested in an equilateral triangular box, the ratio decreases to 3:1. As shown in Figure 6.19 (e), when an approximately square brush unit is tested in an equilateral triangular box, only one part of the X-PLY bristles interact with the box surface. Fewer bristles are in contact with the box wall than in the cases previously described. In addition, some active bristles in this case contact a sloping surface. The inclination of the contact surface relative to the bristle

direction causes the active bristles not to be able to grip the contact surface effectively and hence decrease the reverse traction force and the ratio. Similarly, these factors also apply to a rectangular brush unit tested in an isosceles triangular box as shown in Figure 6.19 (d).

If a circular brush unit is tested in a rectangular box, a square box, an equilateral triangular box and between two parallel boards, the ratio of reverse traction force and forward traction force is in the region of 7:1. So, the interaction between a circular brush unit and these box shapes is a medium level ratio. This may lead to the assumption that a circular brush is a reasonable compromise. However, an average ratio of 7:1 may not be adequate for demanding applications. Recent development for the design of a tractor for pipeline inspections has achieved a ratio of 18:1 and for rescue operations ratios of this magnitude have a considerable advantage. (Gale, N., 2002)

If bristles interact with sloping surfaces, as found in a hexagonal box or a triangular box, the ratio of reverse traction force and forward traction force decreases. The decrease of the ratio is the effect of the inclination of the contact surface relative to the bristle direction. Examples of this effect can be seen in an approximately square brush unit tested in an equilateral triangular box, an ellipse brush unit tested in a hexagonal box, an ellipse brush unit tested in a rectangular box and a rectangular brush unit tested in an isosceles triangular box. In these cases, some regions of bristles contact with sloping box surfaces, decreasing the ratio of traction force.

In conclusion, the ratio of reverse traction force and forward traction force is influenced by several factors, such as X-PLY mechanism and sloping contact surfaces. Active X-PLY bristles help to prevent the brush core from rotating and translating and hence increase the ratio. Active bristle number, contact area and annular gap between brush units and boxes also influence the ratio and the interaction between bristles and contact surfaces.

The above discussion assumes that the shape of the brush is the same in both its slipping mode and its gripping mode. However, using the same brush shape for both modes may have a significant impact on the brush forward motion. For example, in a rectangular void, the trailing brush may change into a rectangular body shape to obtain the maximum reverse force. However, when the trailing brush moves forward, a circular body shape in the rectangular void will produce a smaller resistance to the forward motion than the original rectangular body shape. However, it is important that the adapted shape is able to maintain the axis of the machine and does not allow the front of the machine to dip. Table 6.3 was calculated to show the ratio of reverse force and forward force in different shaped boxes using the best available shapes for the gripping and sliding modes. It was found that in most cases, if the robot brush unit changed to a circular shape, it made the unit easier to move forward. However, if it is changed to a rectangular shape, it gains a maximum reverse traction force. Comparing this table with Table 6.2, much higher ratios of reverse force and forward force can be obtained by such an arrangement. However, this arrangement will make the robot shape change mechanism more complicated and its reliability needs to be examined by practical field tests.

Tested box	Brush unit achieving the minimum forward force	Brush unit achieving the maximum reverse force	Minimum forward force (N)	Maximum reverse force (N)	The ratio of reverse force and forward force
Two parallel boards	Circular brush	Rectangular brush	90	1900	21:1
Square box	Circular brush	Approximately square brush	180	3100	17:1
Rectangular box	Circular brush	Rectangular brush	75	2800	37:1
Equilateral triangular box	Circular brush	Circular brush	120	850	7:1
Isosceles triangular box	Elliptical brush	Rectangular brush	60	720	12:1

Table 6.3: The ratio of reverse traction force and forward traction force (The brush changes its shape when moving forward)

6.2.6 The relationships between traction force, active bristle number and contact area with the box

The robot body brush units tested in the experiments have bristles arranged in 8 rows, 32 bunches per circumference. Each bunch includes approximately the same number of bristles. Bristles installed on the brush unit are not necessarily distributed evenly around the perimeter of the brush unit, as shown in the photographs in Figure 6.4 (b)-(e). If a brush unit was tested in a similarly shaped box, it was found that not all bristles of the brush unit contacted the box. The traction force was influenced by bristle number expressed on a nominal contact area with the box. So, it is essential for the understanding of the design of a robot brush and the brush mechanism to investigate the relationship between traction forces and active bristle numbers and brush contact area with the box. Graphs were produced from the experimental traction results and were classified in two categories. The first category considers the relationship between traction force and active bristle number. Figure 6.20 and Figure 6.21 show the ratio of traction force and active bristle number in different traction

tests. In the figure, the X-axis shows the code for the particular traction force test. The code explanation is given in section 6.1.3.

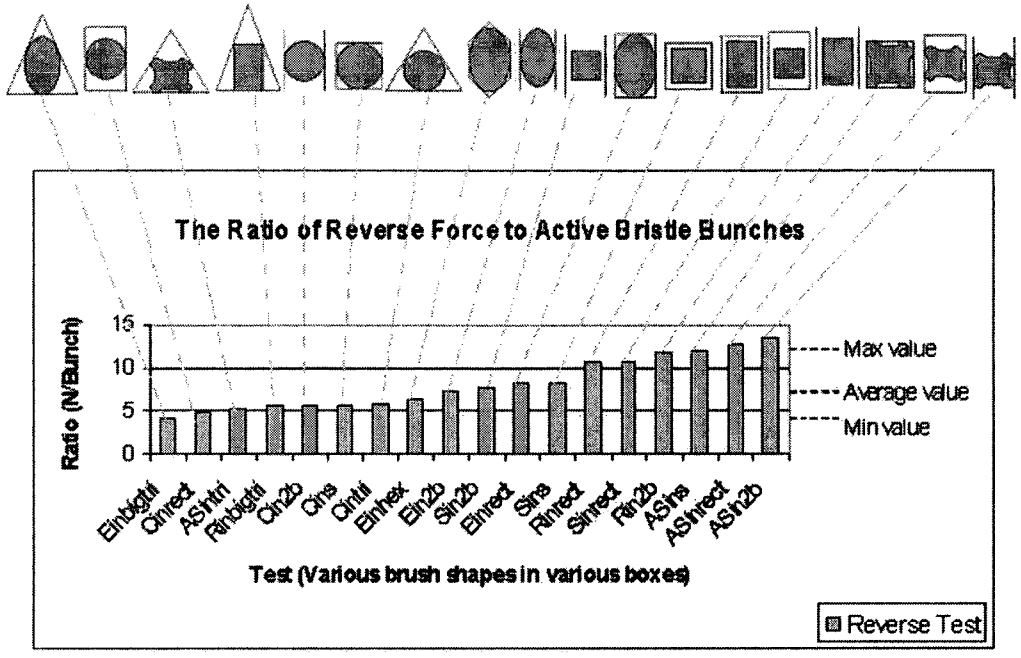

Figure 6.20: The ratio of reverse force and active bristle bunches

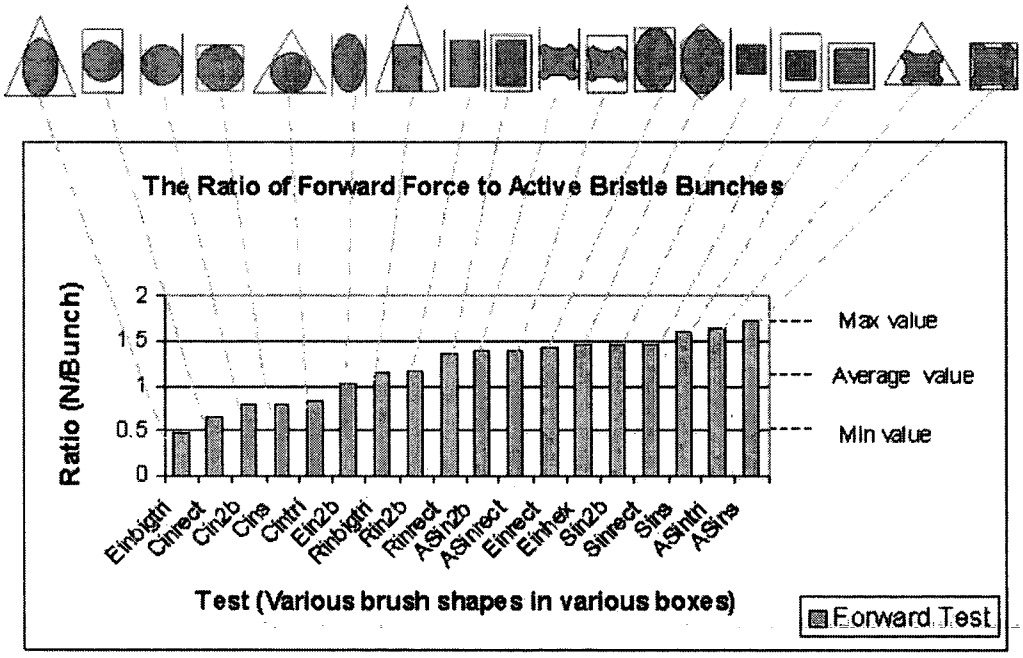

Figure 6.21: The ratio of forward force and active bristle bunches

In Figure 6.20, the ratios of reverse traction force and active bristle number range between 4 and 14. The average value of these ratios is approximately 8. In Figure 6.21, the ratios of forward traction force and active bristle number range between 0.5 and 1.8. The average value of these ratios is approximately 1.2. It was found that the ratio between the average ratio from the reverse traction experiment and the average ratio from the forward traction experiment is about 7:1. This corresponds to most of the cases shown in Table 6.2.

From Figure 6.20, it can be seen that:

If bristles with an X-PLY mechanism interact with the box surfaces, the ratio of traction force and active bristle number will increase. This is because the X-PLY mechanism inhibits rotation or transverse translation of the brush and gives a larger traction force. In the cases considered here, bristle buckling is complicated and is associated with the mode of bristle reversal that occurs if the brush is allowed to rotate or translate transversely. This has been discussed in section 6.2.4 and is illustrated in Figure 6.16 and Figure 6.17.

Another influence on the results shown in Figure 6.20 is the effect of the inclination of the contact surface relative to the bristle direction. If bristles interact with sloping box surfaces, the sloping box surfaces do not allow the bristles to grip effectively and the reverse traction force is decreased. Thus, the ratio of traction force and active bristle number will decrease. Referring to Figure 6.15, section 6.2.4 has given explanation how the inclination of the contact surface relative to the bristle direction influences the traction force. An elliptical brush in an isosceles triangular box and an approximately square brush in a triangular box are also examples in which

the effect of the inclination of the contact surface relative to the bristle direction is significant.

If brush shapes geometrically match the box shapes, a higher ratio of traction force and active bristle number will be produced. This is because more bristles can attain optimum shapes and grip the contact surface effectively and hence produce a larger traction force.

Figure 6.22 and Figure 6.23 consider the relationship between traction force and contact area. The contact area is defined by the area enveloped by the bristles in contact with the box wall. Figure 6.22 shows reverse traction force plotted against contact area and a linear trend line applied to the plot. Figure 6.23 shows forward traction force plotted against contact area and a linear trend line applied to the plot. The trend lines in both graphs show that the traction force increases with contact area increasing. The bigger the contact area, the higher the traction force. It should be noted that this relationship may not exactly match the linear trend lines, since not all contact bristles are in the optimum shape and their contributions to the traction force are consequently not the same. However, the linear trend lines reflect the empirical relationship between traction force and contact area and can be used to generate guidance rules in the design of brush units. The linear trend lines plotted in Figure 6.22, 6.23, 6.24 and 6.25 are used to generalise the approximate relationship of traction force, contact area and active bristles and may not exactly match the actual relationships since these actual relationships are not simply linear but complicated non-linear. However, the linear trend lines can be used as indicative guidance in the design of brush units.

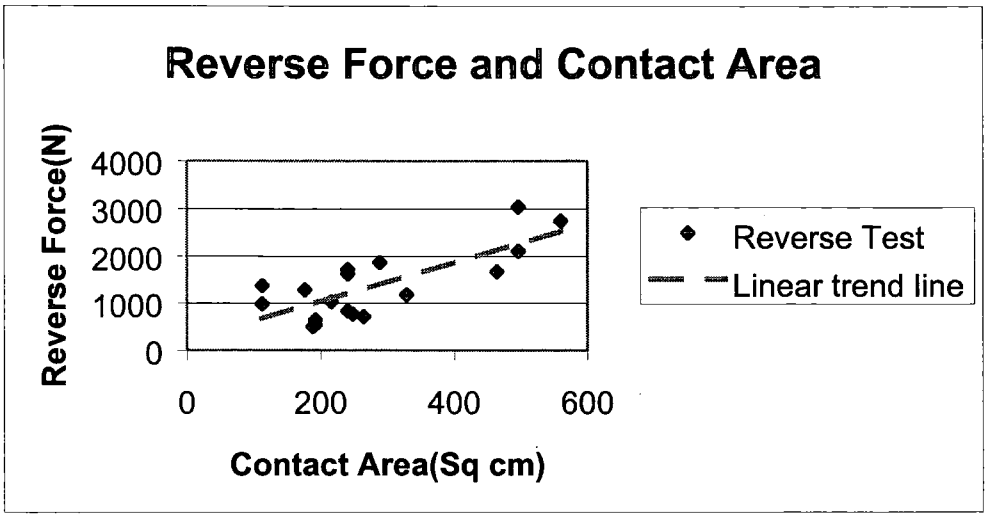

Figure 6.22: Reverse force plotted against contact area

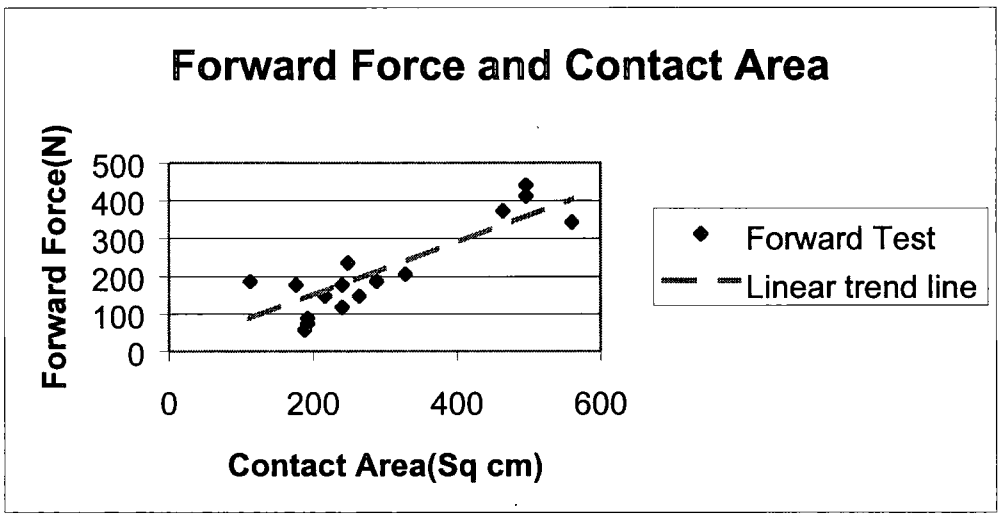

Figure 6.23: Forward force plotted against contact area

Figure 6.24 and Figure 6.25 consider the relationship between traction force and active bristle number. Figure 6.24 shows reverse force plotted against active bristle number and a linear trend line applied to the plot. Figure 6.25 shows forward force plotted against active bristle number and a linear trend line applied to the plot. Both trend lines show that the traction force increases with active bristle number. The more active bristles, the higher the traction force. It should be noted that the actual

relationship between traction force and active bristle number may not exactly match the two trend lines since not all active bristles are the same shape. Some bristles are in an optimum shape and others are active but not in an optimum shape. So, bristles in the optimum shape contribute a higher traction force than those active bristles in a non-optimum shape. Figure 6.24 and Figure 6.25 show a trend in the relationship between traction force and active bristle number that can be used in the design of brush units.

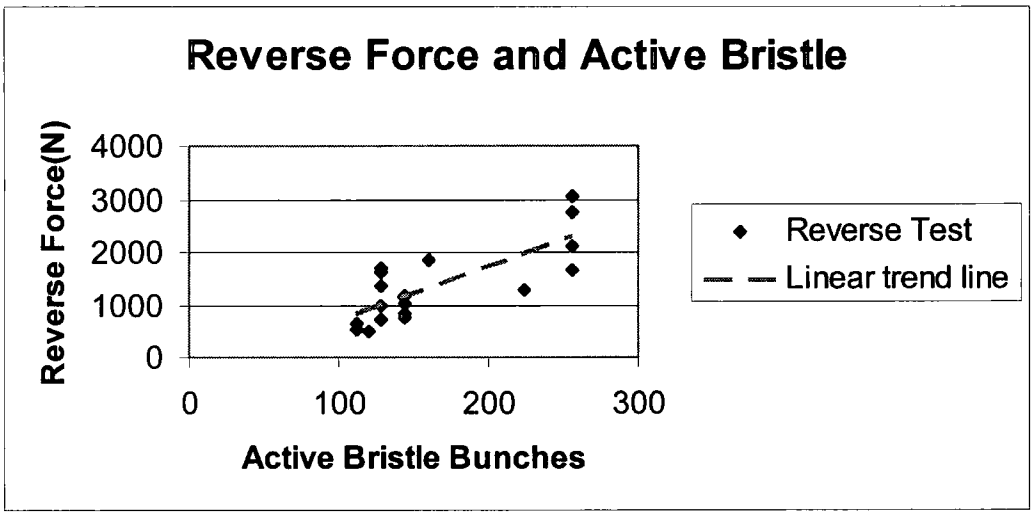

Figure 6.24: Reverse force plotted against active bristle bunches

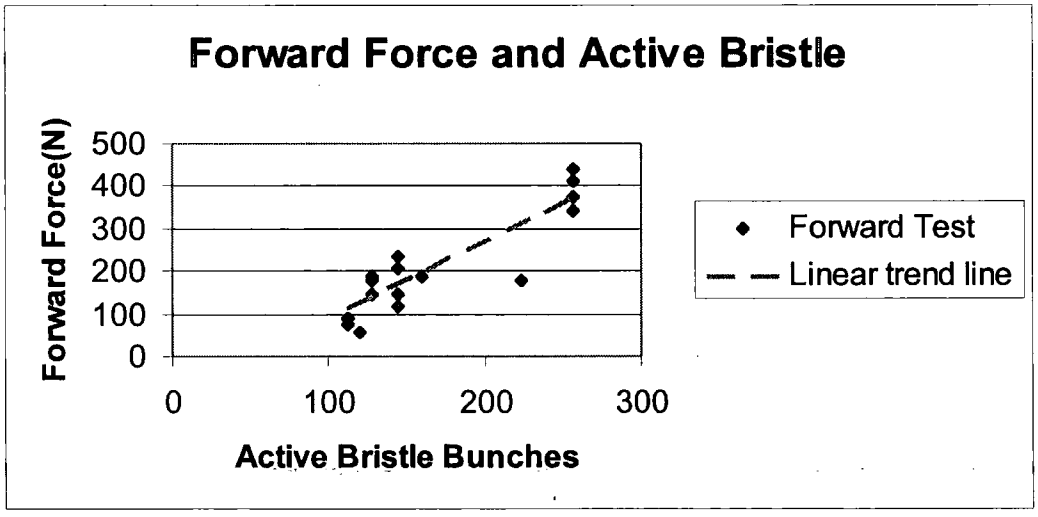

Figure 6.25: Forward force plotted against active bristle bunches

In previous work (Stutchbury, N., 1999) the main thrust was to seek the optimum brush design parameters to minimize resistance to forward motion and maximize gripping or reversal load. This is also important in this work but rather than determining some optimum designs this work is concerned with the maintenance of traction under various void conditions. As a consequence, there is a focus upon the influence of the annular clearance between the brush core and void surface. Chapter 5 investigated this issue. Han (Han, C., 1999) provided some useful analysis of the shape of a bristle when deflected at a surface. Han's work has shown that optimum traction can be obtained when the bristle tip makes a particular angle at the void surface. In a non-circular void the bristle geometry will vary from place to place. So, taking a circular brush inserted into a triangular void as an example, Figure 6.26 shows that in some regions the bristles do not make contact with the void. In some regions, the bristles make contact but are inclined at an angle too great to get a significant grip. Between these two conditions are bristles that meet the wall at or near to the optimum angle and these bristles are the ones that produce a significant proportion of the traction. The theory in the following section seeks to give an understanding of the relative effect of the bristle-wall contact conditions.

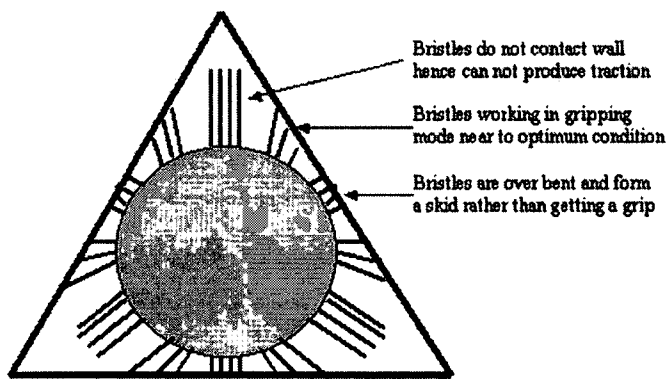

Figure 6.26: A circular brush in a triangular void

6.3 BRISTLE TRACTION FORCE MODEL

This thesis is concerned with the performance of a bristle based traction mechanism. In this mechanism the bristles "grip" the box surface in the manner described earlier. A major consideration of this work relates to the traction that can be achieved by various bristle system designs. The design parameters for a bristle traction system include, bristle length, diameter and material. The performance of the traction force will be influenced by the number of bristles and their distributions. These issues have been considered in previous work. (Stutchbury, N., 1999)

This work focuses upon the use of a bristle based traction system in ill constrained environments such as collapsed buildings or mines. As such the performance of individual bristles will be important and will vary from bristle to bristle. In order to investigate bristle traction performance under these different conditions the previous work needs to be reviewed and in the light of meeting the new constraints. This section starts with a review of the previous work and gives an in-depth understanding of bristle characteristics, paying particular attention to the interaction between bristle physical properties and geometry particularly the annular gap between the brush core and void wall.

In many mechanical systems traction force is derived from an assumption of Coulomb friction ($F_\mu = \mu F_n$) where μ is the coefficient of friction, and F_n is the normal force at the contact area. In simple cases, the normal force is often derived from the gravitational force and is a constant no matter which direction the vehicle is moving. The fundamental characteristics of the bristle based system described here is

that the reaction force F_n is highly direction sensitive. The reaction force F_n is derived from the elastic properties of the bristle. In the forward sliding motion of bristle traction the reaction force at the bristle tip is relatively small and caused by bristle resilience. In the reverse motion of bristle traction, the brush is pushed horizontally against the inclination of the bristle and the reaction force is considerably increased because of the large axial thrust force on the bristle. This increased reaction force F_n is then transformed into a high friction force μF_n.

Stutchbury investigated this mechanism and produced a force equilibrium diagram that showed how the reversal mechanism produced the characteristic grip of the bristles and how design parameters influenced the traction characteristics (Stutchbury, N., 1999). Considering a bristle sliding forwards through a pipe, it can be assumed that the bristle forms an angle with the pipe wall which is represented by line OH in Figure 6.27, which is based on Stutchbury's diagram. If the bristle moves towards the left, its motion will be opposed by a friction force μF_n, where F_n is the force normal to the pipe wall caused by the bristle's resilience. A brush inside a pipe is in transverse equilibrium so that the sum of all the F_n values for all the bristles extending from the brush core will be zero and the sum of all the μF_n components will equal the total force required to move the brush forward through the pipe. The sum of the force F_n perpendicular to the pipe wall and the frictional force μF_n is the resultant force F_{OC}. The angle between OA and OC is the complementary angle θ of the friction angle α. The resultant force F_{OC} can be resolved into two components, one component perpendicular to the bristle F_{OD} and the other component along the bristle F_{DC}. If the bristle is relatively straight and the thrust along the bristle is not

sufficient to cause buckling, the bending of the bristle can be assumed to be caused by the bending force F_{OD} acting perpendicular to the bristle.

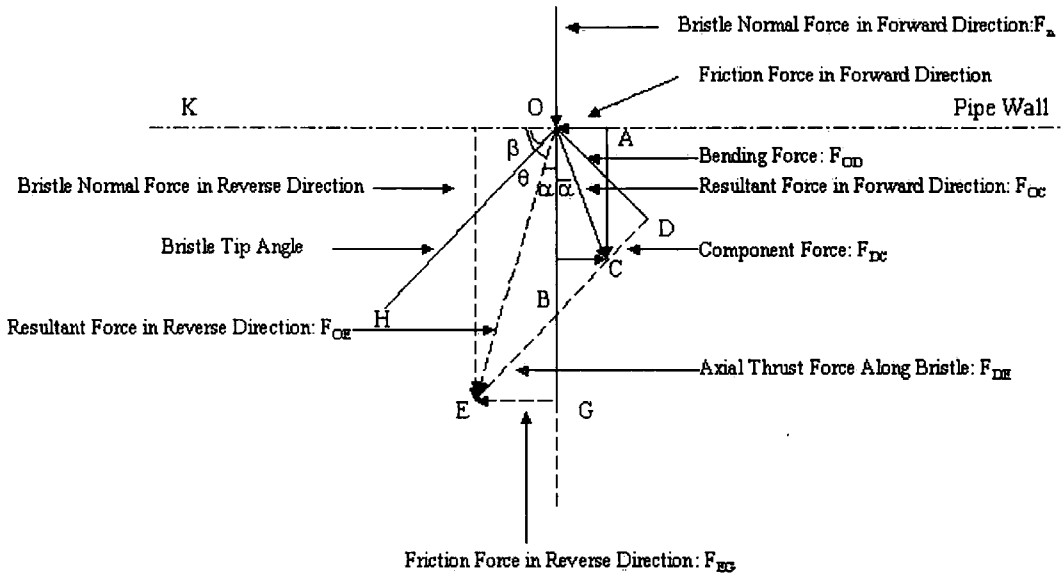

Figure 6.27: Illustration of bristle force

If the brush is put into a gripping mode by pushing the core in the reverse direction, the frictional force direction is also reversed. If the value of friction coefficient μ is assumed to be the same in both directions, the resultant force acting on the bristle tip will be along the line OE and the angle between OE and the pipe wall is once again the angle θ. Although the limiting line of action of the resultant force acting on the bristle in its gripping mode is known at this stage, the magnitude of the resultant force has not yet been determined. In the forward sliding mode it was assumed that the shape of the bristle, that is the bending of the bristle, was determined by the bending force F_{OD}. If it is further assumed that the shape of the bristle remains the same in the gripping mode, only the thrust force along the bristle increases. If the line of the thrust force along the bristle is extended, it will eventually intersect with the friction angle line OE and give a thrust magnitude DE, which is the force F_{DE}. In

Figure 6.27 it can be seen that in gripping mode the resultant force acting at the bristle tip is F_{OE}, which can be resolved into two components F_{OD} perpendicular to the bristle and F_{DE} along the bristle. Resolving the resultants into the direction along the pipe axis, in both forward sliding and gripping modes, the ratio of the force required to push a brush forward and the reverse force available in the gripping mode can be calculated, that is GE/BC. The model proposed has provided a method for predicting the forward to reverse or "slip to grip" ratio, for given frictional conditions. This model is deemed satisfactory up to the onset of bristle buckling.

Although Stutchbury's description was useful in understanding the bristle gripping mechanism it was purely geometrical in nature. For the purpose of this work, Stutchbury's approach has been absorbed into a mathematical approach which, although abstract, can be used in a more quantitative and analytical manner.

6.3.1 Mathematical discussion of bristle reverse theory

This section described the author's extension of Stutchbury's work and its application to a particular case to obtain theoretical results. In Figure 6.27, OH is the bristle and $\angle KOH = \beta$ is the bristle tip angle. $\angle KOE = \theta$ is the complementary angle of the friction angle of the bristle. OH is perpendicular to OD, μ is a friction coefficient and $\alpha + \theta = 90°$. It is assumed that F_{OD} remains the same in gripping mode as it does in the forward direction, so F_{OD} is constant. In the force diagram of Figure 6.27, the thrust along the bristle F_{DE} increases considerably if the angle β between the bristle and pipe wall approaches the angle θ. When the angle β equals

the angle θ, the vector representing the thrust force along the bristle (extension of DC) is parallel to the vector of the resultant acting along the frictional angle line OE. This means that the theoretical thrust along the bristle is infinite. These conclusions can be explained by the following mathematical discussion.

From the geometry of the Figure 6.27, the following equations are known,

$$\angle HOE = 90° - \alpha - \beta, \tag{6.2}$$

$$\angle DOC = 90° - 2\alpha - \angle HOE = \beta - \alpha, \tag{6.3}$$

$$\angle EOD = 2\alpha + \angle DOC = \beta + \alpha, \tag{6.4}$$

Thus,

$$F_{OE} = \frac{F_{OD}}{\cos \angle EOD} = \frac{F_{OD}}{\cos(\alpha + \beta)} \tag{6.5}$$

$$F_{EG} = F_{OE} \sin\alpha = \frac{F_{OD} \sin\alpha}{\cos(\alpha + \beta)} \tag{6.6}$$

If β increases, $\cos(\alpha + \beta)$ decreases, and $\frac{F_{OD}}{\cos(\alpha + \beta)}$ will increase, thus F_{EG} will increase.

If β decreases, $\cos(\alpha + \beta)$ increases, and $\frac{F_{OD}}{\cos(\alpha + \beta)}$ will decrease, thus F_{EG} will decrease.

If $\beta = \theta, \alpha + \beta = 90°$. This in turn leads to $\cos(\alpha + \beta) = 0$ and thus $\frac{F_{OD}}{\cos(\alpha + \beta)} = +\infty$.

The above explains how the theoretical thrust along the bristle becomes infinite when the angle β is equal to the angle θ. However, the bristle and the pipe wall cannot sustain thrust forces of infinity. For example, a slender bristle will obviously collapse by elastic buckling before reaching the infinite value. Alternatively, a short stubby

bristle may not buckle but may collapse by plastic yielding. The failure of the pipe wall may also limit the magnitude of the bristle thrust force. The buckling of a slender flexible bristle is probably the mode of failure in most practical cases and thus the magnitude of the thrust along the bristle is limited to the buckling load. Since the thrust along the bristle is limited to the buckling load, it may not be possible for the resultant force acting on the bristle tip to reach the frictional limit. So, in the case of a bristle failing by buckling, even if the bristle angle is near or beyond the angle θ, the force in the axial direction will be less than the limiting friction value and therefore the bristle will grip without slip. However, as the bristle tip rotates about O and the bristle angle moves beyond the angle θ, the axial force that the bristle can sustain decreases to zero and thus the bristle flips through, pushing the brush core back along the pipe. The failure of the bristle by buckling is an instability phenomenon so the flip through of the bristle is a quick and unstable process.

6.3.2 Reverse force F_{EG} of a single bristle

It is important to understand how a bristle behaves before it collapses because this is helpful in understanding the bristle characteristics and the design of robot brush units. In Figure 6.27, F_{DE} is a thrust force along the axial direction of the bristle and F_{EG} is a component of force F_{OE}. The force $F_{EG}^{'}$ represents the maximum value of F_{EG} and is influenced by F_{DE}, as shown by the equation (6.8). So, $F_{EG}^{'}$ is determined by the maximum value of F_{DE}, which is the maximum thrust force a bristle can sustain and is determined by many factors, such as the Young's modulus of the bristle

material, bristle length and diameter, etc. In Figure 6.27, the angle $\beta(\angle KOH)$ between the pipe wall and OH also influences this maximum force.

Based on the force diagram shown in Figure 6.27, a simulation of the reverse force of single bristle was carried out. The simulation investigates how the maximum value F'_{EG} of force F_{EG} changes and how the reverse force F_{EG} changes with the increase of the angle $\beta(\angle KOH)$ between the pipe wall and OH. F'_{EG} is a variable influenced by F_{DE}, α and β, so it may be plotted against β. The first task in the simulation is to calculate the maximum value F'_{EG}. From Figure 6.27, the following equations can be acquired:

$$F_{OE} = \frac{F_{DE}}{\sin(\alpha + \beta)} \tag{6.7}$$

$$F'_{EG} = F_{OE} \sin\alpha = \frac{F_{DE} \sin\alpha}{\sin(\alpha + \beta)} \tag{6.8}$$

In the simulation, the properties of the bristle are based on those used in the experiments. For the simulation, bristle length $l = 55mm$, bristle diameter $d = 0.25mm$, $E = 207 \times 10^9 Pa$, $(1Pa = 1N/M^2)$, and the friction coefficient between steel and wood is 0.16 (Carvill, J., 1997). The fourth mode of Euler buckling described in section 6.2.3 was used to calculate the axial thrust force P assuming the bristle fixed at one end and pinned at the other end. So, in the computation by using equation (6.1), $K = 2.05$. In addition, the cross section of the bristle was circular, thus,

$$I = \frac{\pi d^4}{64}.$$

So, from the formula of Euler buckling (6.1),

$$P = \frac{K\pi^2 EI}{l^2} = \frac{K\pi^2 E\frac{\pi d^4}{64}}{l^2} = \frac{K\pi^3 Ed^4}{64l^2} = 0.265\text{N},$$

In the simulation, using the values above, F_{DE} is equal to 0.265N and substituted in equation (6.8) to calculate the maximum value $F_{EG}^{'}$ of F_{EG}. With different values of the angle β, the value of $F_{EG}^{'}$ could be calculated and plotted in Figure 6.28.

The other task in the simulation was to calculate the reverse force F_{EG} by using equation (6.9). F_n can be calculated by formula (3.1). So, F_n = 0.078N in the simulation. In Figure 6.27, $\alpha = \arctan(\mu) = 9.09°$ can be known. From Figure 6.27, the following relationship can be determined:

$$F_{OC} = \frac{F_n}{\cos\alpha} \qquad F_{OD} = F_{OC}\cos(\beta - \alpha)$$

Thus,

$$F_{EG} = \frac{F_{OD}\sin\alpha}{\cos(\alpha+\beta)} = \frac{F_n \sin\alpha\cos(\beta-\alpha)}{\cos\alpha\cos(\alpha+\beta)} \tag{6.9}$$

The simulation calculated the force F_{EG} with different values of the angle β and plotted the results in the graph in Figure 6.28. In the plot of Figure 6.28, the X-axis variable is the bristle tip angle β in radians and the Y-axis variable is the reverse friction force in Newton. Curve A represents a limitation line $F_{EG}^{'}$, which decreases with the increase of the angle β. Curve B represents the reverse force F_{EG}, which increases slowly at the starting stage and then increases quickly before the bristle reaches buckling failure. Curve A and curve B intersect at point H. If F_{EG} reaches the point H, β is 73.8° (1.29 in radian). The projected point of H in the X-axis is M. The Y-axis coordinate of H is the maximum value of force F_{EG}. That is, the value of F_{EG}

cannot exceed the limitation curve A at the intersection point H. The bristle has already failed because of the buckling before the angle β reaches point M.

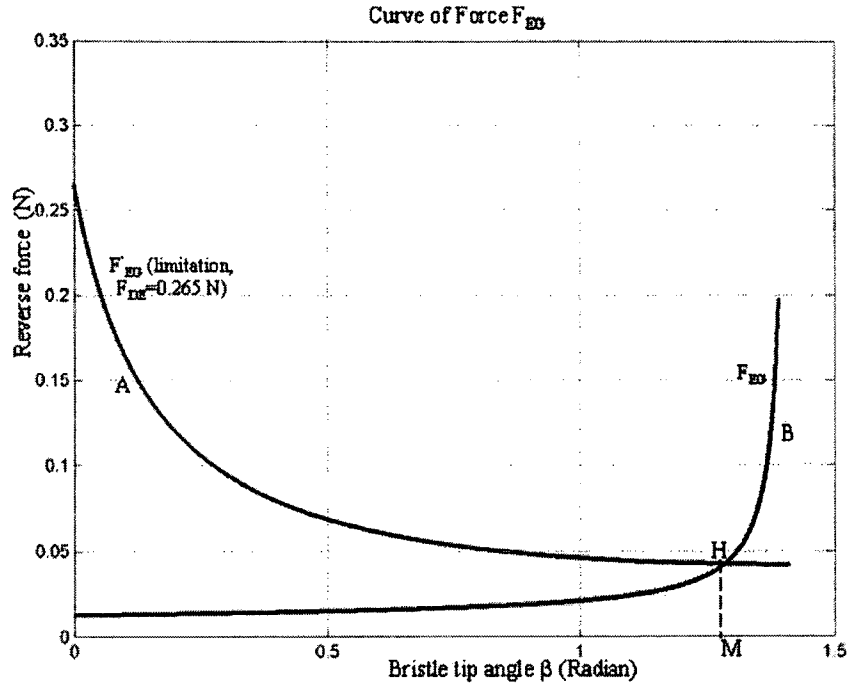

Figure 6.28: The characteristics of the reverse force F_{EG}

From formula (6.9), the value of F_{EG} at the point H can be calculated and equals 0.043N. The brush unit has 32 columns, 8 rows of bunches of bristles. Each bunch has an average of 200 bristles. So, in theory, the traction force should be $F = 0.043 \times 32 \times 8 \times 200 = 2201N$. This agrees with the traction experiment in Figure 6.11-(18). In the traction experiment, the maximum reverse force is about 2300N. The reason for choosing the experiment of a square brush in a square box is because all of the bristles are seen to be active and approximately in the same shape.

6.4 SUMMARY

This chapter described the traction force experiment of brush units in different boxes. The interaction between the boxes and the brushes units was investigated. It

was found that the traction forces of brush units were influenced by several factors such as number of bristles in operation, effectiveness of bristles in operation and the ability of bristles to withstand buckling. These factors also influenced the ratio of reverse traction force and forward traction force. The relationships of traction force, active bristle number and contact area with the box were also plotted and investigated. Traction force increases with the increase of active bristle number and contact area between the brush unit and the box. The traction force plots were explained mathematically and analyzed by using different modes of Euler buckling. Bristle traction theory was analyzed in depth and the reverse friction force of a single bristle was investigated through a simulation. The next chapter will give conclusions for all of the research work presented in this thesis.

CHAPTER 7

CONCLUSION AND FUTURE WORK

7.1 THESIS SUMMARY

This thesis describes the concept of a brush based robot for earthquake rescue and for traversing pipes with various cross sections. To illustrate the concept, the thesis first discussed the current development of rescue robots and pipe robots. Then the thesis focused on the description of a brush based pipe crawling robot developed by the University of Durham, which could be used as a basis of an earthquake rescue robot. The concept of the robot was illustrated and compared with other current rescue robots and pipe robots. The robot could change its body shape by means of moving support actuators acting upon a steel spring hoop. After outlining the characteristics of this robot, the robot body shape change approach was illustrated and simulations were carried out to test the feasibility of the robot body shape change approach. Chapter 4 described the design and working principle of a robot void shape sensor which was strain gauge based and used to detect box shape in robot body shape change experiments. Chapter 5 described the design details of the robot body shape change experiments and discussed the experimental results. The experiments demonstrated the robot concept and tested the feasibility of the robot working principle. Chapter 6

focused on the robot brush unit traction investigation, bristle traction force theory and its mathematic model. In addition, the mathematic model and bristle traction force theory were used to explain the variation of traction force in brush unit traction experiments.

These conclusions are discussed in three sections. Section one considers the robot body shape change mechanism and the robot body shape change control algorithm. Section two considers the robot sensor design characteristics, robot body shape change experiments and experimental results. Section three considers the robot brush unit traction experiments, bristle traction force theory and mathematic model applied to the traction experiments. In addition, further work is considered at the end of the chapter.

7.1.1 The mechanism and algorithm of robot body shape change

The literature review shows that there is a primary need for developing a USAR rescue robot, which can help rescue personnel to carry out a rescue task in a hazardous environment. More and more researchers and industrialists are involved in research in this field because of the potential market and industrial applications of USAR robots. Some USAR robots have been developed and are available in the market, but none can fulfil the strict requirements of practical USAR tasks.

The brush based rescue robot was designed to be able to travel in voids within a collapsed building. The robot is intended to be pneumatically driven and the shape of its body component can be changed by moving the support actuators acting upon a

thin spring steel hoop. The robot body shape change mechanism was investigated by both computer simulations and lab experiments. The robot was articulated and composed of several body components in order to deal with pipe bents and irregular paths through linked voids.

The robot shape change algorithm is the combination of a least square algorithm and a look-up table method. The algorithm can predict the robot body shape by referring to an array of coordinates, which is the best search result from a robot body shape information database. The algorithm was found to be effective by both computer simulation and lab experiments.

In this research, a robot body shape information database was built and composed of data files of the deformed robot body shape. The data files were acquired by repeatedly running finite element computations, which involved considerable work. It was found that several programs written in C could run these computations automatically and considerably reduced the work involved.

7.1.2 The robot body components and void shape sensor

A robot void shape sensor and a robot body component were used to conduct robot body component shape change experiments and test the robot body shape change mechanism. It was found that the robot void shape sensor could detect the approximate shape of the void. If the robot void shape sensor was installed with more fingers, the sensor could give more detailed information of the void shape.

In the robot body component shape change experiments, boxes of different geometrical shapes were used to simulate void shapes. This simplification is appropriate because the research work is still in an initial stage and more focused on the demonstration of the robot concept and working principle. It was found that the robot body component could change its shape symmetrically and fit the boxes with sufficient precision to allow the traction mechanism to work.

As expected from a consideration of the design constraints, it was found that the robot body component could only change its body shape symmetrically. This was because restriction to a symmetrical change of the robot body shape simplified the robot body structure and the algorithm program for the robot body shape change. The robot body component used in the experiment had four actuators and this determined that it could only change to limited symmetrical shapes. It was concluded that the robot body component could be equipped with more actuators and hence be able to achieve more complex shapes. This could help the robot to fit a void better and be more able to work in a real environment.

It was found that the currently used actuator in the experiment, a linear stepper motor, could achieve the required movements by the robot body shape change program to change the robot body shape symmetrically but it is not powerful enough to change the robot body shape non-symmetrically. So, more powerful actuators may be required for the future non-symmetrical shape change of the robot body.

7.1.3 Traction force experiments and bristle traction force theory

It was observed in the forward traction force experiments that a forward traction force curve rose up gradually and reached a peak loading force, and then fell gradually to a steady forward force. This phenomenon happened in all forward traction force experiments. A large forward traction force could be produced if a brush unit had a similar shape to a box and had good contact with the box wall.

It was observed in the reverse traction force experiment that a reverse traction force curve rose up sharply and reached a peak reverse force, and then fell quickly. This phenomenon happened in all reverse traction force experiments. A large reverse traction force could be produced in a reverse traction force experiment if a brush unit had a similar shape to a box and had good contact with the box wall.

It was found that bristle traction forces were influenced by several factors such as number of bristles in operation, effectiveness of bristles in operation and the ability of bristles to withstand buckling. More active bristles and a better contact with the void wall help to increase the traction force. Bristles of a rectangular brush unit and an approximate square brush unit in the experimental work naturally formed an X-PLY mechanism in which bristles crossed like an "X". The X-PLY mechanism helps to enhance the ability of bristles to withstand buckling and prevent the brush core from rotating or translating, and thus producing a large reverse traction force. Traction force was also influenced by the inclination of the contact surface relative to the bristle direction because bristles could not grip the contact surface effectively if the bristle contacted with a sloping surface. The number of bristles in operation, effectiveness of

bristles in operation and the ability of the bristles to withstand buckling also influenced the ratio of reverse traction force and forward traction force.

A mathematic model of bristle traction force theory was used to explain the variation of traction force. Buckling theory was used to analyse how a bristle behaved in the traction force experiment and the maximum reverse friction force for the bristle was calculated through a simulation based on the buckling theory. The simulation result matched the experimental result of the reverse traction experiment. It was concluded that in a reverse traction force experiment the bristle failed before the angle between the bristle tip and the box wall reached the friction angle because the stiffness of the bristle could not sustain the maximum buckling force.

7.2 THESIS CONTRIBUTIONS

This thesis studies the concept design of a brush-based, shape reconfigurable robot for earthquake rescue. The research work described in this thesis involves both lab experimental work and theoretical research. A number of contributions have been made to the field of earthquake rescue robotics. These contributions are embodied in several published papers.

A paper "*The Concept and Research of a Pipe Crawling Rescue Robot*" was published in the *International Journal of Advanced Robotics* (Wang, Z., 2002 a) and an overlapping paper "*The Simulation and Concept of a Pipe Crawling Robot for Earthquake Rescue*" was presented in an IEEE international conference (Wang, Z., 2002 b). These two papers presented the concept model of a shape reconfigurable

earthquake rescue robot. The robot body shape change mechanism and its control algorithm were developed to enable the rescue robot to change its body shape intelligently and negotiate changes of void shape. The robot body shape change algorithm is the combination of a least square algorithm and a look-up table method. The algorithm can predict the robot body shape by selecting an array of coordinates, which is the best search result from a pre-computed robot body shape information database. The algorithm was found to be effective by both computer simulation and lab experiments. A control system for the robot body shape change mechanism, including software and hardware, was also developed and found to be effective. In addition to the published papers, a set of programs were written in C language and used to conduct finite element calculations with ABAQUS and automatically acquire the coordinate data for the pre-computed robot body shape information database.

Another paper, *"A Void Shape Detecting Sensor for a Rescue Robot"* was published in the *international journal the Industrial Robot* (Wang, Z., 2003 a). In the work described in this paper, a void shape sensor based on an electrical strain gauge system was developed and used to detect void shapes in an experimental investigation of the robot body shape change mechanism. The sensor used strain gauges to measure the deflections of sensor fingers and a spline interpolation algorithm was used to provide the curving fitting through the detected points on the void wall and thus acquire the void shape. The software system and hardware system for the void shape sensor were developed and used to conduct a number of exploratory robot body shape change experiments. The experimental results showed that the void shape sensor worked effectively and the robot body component could change its body shape to match the detected void shapes.

The paper "*The Bristle Theory and Traction Experiment of a Brush Based Rescue Robot*" was published in the *International Journal of Robotica* (Wang, Z., 2003 b) and a further paper "*Bristle Mechanism Study of a Shape Reconfigurable Brush Robot*" was published in the *international journal the Industrial Robot* (Wang, Z., 2003 c). These two papers presented the research work related to an experimental and theoretical study of bristle traction force. Traction experiments were carried out to investigate the traction change related to robot body shape change. The interaction between the robot body shape and the void shape and the bristle behaviour were investigated and analysed, using an adaption of the Euler buckling theory. It was found that bristle traction forces were influenced by several factors such as number of bristles in operation, effectiveness of bristles in operation and the ability of bristles to withstand buckling. A mathematical model of bristle traction force was set up and a simulation of reverse traction force of one single bristle was conducted to test the model. The maximum reverse force for the bristle was acquired through this simulation. The simulation results matched the results of practical traction experiments.

7.3 FUTURE WORK

There are a few areas, which are deemed to be in need of further work in the future. The first concerns the distribution of forces generated by the robot body acting against the void wall because of the restriction to a symmetrical change of the robot body shape. This will influence the robot traction performance when the robot body does not fit the void very well and some parts of the robot body do not contact with

the void wall, or these parts become too closed to the void wall. The anticipated robot body shape, as determined by the robot body shape change algorithm, could be distorted. To deal with this concern, further work may be conducted to improve the robot body shape change mechanism and enable the robot body to change to a non-symmetrical shape. More actuators can be used to make the robot able to change to more complicated shapes. The robot void shape sensor may need further work to be able to detect the void shape more accurately. Thus, the robot shape change algorithm will have more accurate information of the void shape and be able to decide a shape closer to the void shape.

Although the current brush robot concept primarily deals with void shape, there will also be a need to accommodate void size changes. The present concept is able to deal, to some extent, with both shape change and size change by virtue of the use of long flexible bristles. Future work should include a more active system that can change both brush shape and size. Some concepts of an expandable robot body hoop, which can be used to substitute for the continuous body hoop used in this work have been described in chapter 5 and can serve as a starting point for the expandable body change research for future design work.

The robot body shape information database can include more data files of robot body shape so that the robot will be able to change to more shapes. The robot body shape change algorithm may take a longer time to find the best robot body shape from a big robot body shape information database and the more data files will need more memory space. However, a powerful computer and optimization of the robot body shape change program can deal with this situation. It was found in this work that

the robot body shape change algorithm program worked on a Pentium II MMX 233 computer promptly and correctly.

For the robot void shape sensor, narrow spring flat bristles can be used to take the place of the aluminium fingers used in the current sensor prototype. This could help to allow more fingers on the limited space of the circular sensor base and avoid the finger penetrating the void wall.

In the future field test stage, stronger actuators should be used to sustain the large side forces, which will exceed the capacity of current linear stepper motors. The robot control system can be integrated into an on-board system instead of running on a remote PC. This could make the robot control system more portable for the purpose of practical field use. The robot prototype used in the field test may be equipped with a camera, a microphone, a speaker and a CO_2 detector. Correspondingly, the robot hardware and the robot control software need further development to be able to manage and respond to the information from these external sources.

REFERENCE

ABAQUS/Standard User's Manual, Version 5.6, Hibbitt, Karlsson & Sorensen, Inc. (1996).

Adachi, Y. and Nakagawa, O. (1996), Development of the Under Water Pipe Cleaning Robot, *Proceedings of the Techno Ocean Symposium*, Vol. 2, Kobe, Japan, pp. 443-448.

Adachi, Y., Tokuyama, K. and Sawada, T. (1998), Field Actual Experiment of Under Water Pipe Cleaning Robot, *Proceeding of the Techno Ocean Symposium,* Kobe, Japan, pp. 165-168.

Ahlberg, J., Nilson, E. and Walsh, J. (1967), The Theory of Splines and Their Applications, London: Academic Press.

Beller, M. and Schoenmaker, H. (1998), Pipeline inspection: A turnkey approach, pp. 1-10, research report of Pipeline Integrity International Ltd.

Blitch, J. (1994), AI Applications for Robot Assisted Urban Search and Rescue, *AI exchange*, Vol.147, August, pp. 92-98.

Blitch, J. (1996), An Expert System Application for Robot Assisted Urban Search and Rescue, *Robotics for Challenging Environments Conference,* Albuquerque, pp. 199-205.

Borden, W. (1994), USAR Operations: An Overview (Northbridge Earthquake), *Fire Engineering*, Vol. 9, pp. 15-20.

Bradbeer, R., Harrold, S., Nickols, F. and Yeung, L. (1997), An Underwater Robot for Pipe Inspection, *Annual Conference on Mechatronics and Machine Vision in Practice,* Toowoomba, Australia, pp. 152-157.

Carvill, J. (1997), Mechanical Engineer's Data handbook, Oxford: Butterworth-Heinemann.

Casper, J., Murphy, R. and Micire, M. (2000), Issues in Intelligent Robots for Search and Rescue, *SPIE Ground Vehicle Technology II*, Orlando, Florida, April, 2000.

Casper, J. (2002), Human-robot Interactions During the Robot-assisted Urban Search and Rescue Response at the World Trade Centre, M.Sc. thesis, University of South Florida.

Choset, H. and Burdick, J. (1996), Sensor Based Planning for a Rod Robot, *IEEE/ICRA*, Minneapolis, Minnesota.

Clarke, T. (1990), The Use of Optical Triangulation for High Speed Acquisition of Cross Section or Profiles of Structures, *Photogrammetric record*, no.13 (76), October, pp. 523-532.

Clarke, T. (1995), The Development of an Optical Triangulation Pipe Profiling Instrument, Optical 3-D Measuring Techniques III, Wichmann, pp. 331-340.

CleanFlow system Ltd. (2001), ClearLine Profiler, Albany, New Zealand, (information annotated from product brochures).

CUEA (Cambridge University Engineering Department and Engineers' Association), (1995), a Gem of an Idea, *Enginuity*, the newsletter of Cambridge University Engineering Department and Engineers' Association, no.4, Spring, Article 5.

Edward, G. (1999), New Scientist, October 26, No.2206, U.K., pp. 11.

Estier, T., Crausaz, Y., Merminod, B., Lauria, M., Piguet, R. and Siegwart, R. (2000), An Innovative Space Rover with Extended Climbing Abilities, *Proceedings of Space and Robotics 2000*, Albuquerque, USA, Feb. 27-Mar. 2.

Gale, N. (2002), Bi-directional Tractor Mechanism, M. Eng. Thesis, University of Durham.

Glen, B., Devon, F. and Rhett, M. (1997), Automated Pipe Inspection Robot, *Industrial robot*, Vol. 24, no.4, pp. 285-289.

Han, C. (1999), The Experiment Investigation of a Pipe Robot, M.Sc. thesis, University of Durham.

Hu, H., Yu, L., Tsi, P. and Zhou, Q. (2001), Internet-based Robotic Systems for Teleoperation, *Assembly Automation*, Vol.21, No.2, pp. 143-151.

Kawaguchi, Y., Yoshida, I., Kurumatani, H., Kikuta, T. and Yamada, Y. (1995), Internal Pipe Inspection Robot, *IEEE International Conference on Robotics and Automation*, No.1, May, Nagoya; Japan, pp. 857-862.

Kitano, H. and Tadokoro, S. (2001), RoboCup Rescue A Grand Challenge for Multiagent and Intelligent Systems, *AI Magazine*, Spring.

Kuntze, H. and Haffner, H. (1998), Experience with the Development of a Robot for Smart Multisensoric Pipe Inspection, *Proceeding of the 1998 IEEE International Conference on Robotics and Automation*, Leuven, Belgium, May, pp. 1773-1778.

Loughlin, C. (1992), Sensors for Industrial Inspection, Dordrecht: Kluwer Academic Publishers.

Luk, B., Stone, T. and Cooke, D. (1995), Robug III - The Design of an Eight Legged Teleoperated Walking and Climbing Robot, *Mechanical Incorporated Engineer*, Vol. 7, no. 2, pp. 37-45.

Masuda, R., Oinuma, T. and Muramatsu, A. (1996), Multi-Sensor Control System for Rescue Robot, *IEEE/SICE/RSJ International Conference on Multisensor Fusion and Integration for Intelligent Systems,* Washington, pp. 381-388.

Matthies, L., Xiong, Y., Hogg, R., Zhu, D., Rankin, A., Kennedy, B., Hebert, M., Maclachlan, R., Won, C., Frost, T., Sukhatme, G., McHenry, M. and Goldberg, S. (2000), A Portable, Autonomous, Urban Reconnaissance Robot, *The 6th International Conference on Intelligent Autonomous Systems*, Venice, Italy.

Mills, C., and Navarro, M. (1995), Urban Search and Rescue Task Force Overview, *Proceeding 3rd International Symposium on Mine Mechanization and Automation*, June, Golden, Colorado, USA.

Miyagawa, T., Suzumori, K., Kimura, M. and Hasegawa, Y. (1999), Development of Micro-inspection Robot for Small Piping, *International Journal of Japan Society of Precision Engineering*, Vol. 33, no.2, pp. 90-93.

Murphy, R., Casper, J., Hyams, J. and Micire, M. (2000 a), Mobility and Sensing Demands in USAR, *IECON 2000*, Nagoya, Japan, October.

Murphy, R., Casper, J., Micire, M., and Hyams, J. (2000 b), Assessment of the NIST Standard Test Bed for Urban Search and Rescue, *NIST Workshop on Performance Metrics for Intelligent Systems.*

Pierce, F. (1956), A Short Table of Integrals, Boston: Ginn and Company, fourth version.

Prassler, E., Ritter, A., Schaeffer, C. and Fiorini, P. (2000), A Short History of Cleaning Robots, *Autonomous Robots*, no. 3, pp. 211-226.

Ryder, G. (1965), Strength of Materials, Macmillan & Co. Ltd.

Sarig, Y. (1993), Robotics of Fruit Harvesting: A State of the Art Review, *Journal of Agricultural Engineering Research*, No. 54, pp. 265-280.

Seig, J. (1992), Introductory Robotics, Prince Hall International (UK) Ltd.

Stutchbury, N. (1999), Design Characteristics of a Pipe Crawling Robot, Ph.D. thesis, University of Durham.

Suzumori, K. (1991), Flexible Microactuator for Miniature Robots, *Proc. IEEE Micro Electro Mechanical System*, pp. 204.

Tokuda, K., Osuka, K. and Ono, T. (1999), Concept and Development of General Rescue Robot CUL, *IROS Proceedings*, Vol. 3, October 12th, Kyongju, Korea, pp. 1902-1907.

Toll, D. (1993), A Computer Control System for Stress Path Triaxial Testing, *5th International Conference on Civil and Structural Engineering and Computing,* Edinburgh, 1993, pp. 107-113.

Tonoike, A., Kitagawa, A. and Tsukagoshi, H. (1998), A Study on a Gap Creeping Robot for the Disaster Rescue Operation, *Symposium on Fluid Control*, Vol. 13, December, Saitama, Japan, pp. 69-72.

Trevelyan, J. (1999), Redefining Robotics for the New Millennium, *International Journal of Robotics Research*, Vol. 18, No 12, December, pp. 1211-1223.

Wang, Z. and Appleton, E. (2002 a), The Concept and Research of a Pipe Crawling Rescue Robot, *International Journal of Advanced Robotics*, Vol. 17, No.4, pp 339-358

Wang, Z. and Appleton, E. (2002 b), The Simulation and Concept of a Pipe Crawling Robot for Earthquake Rescue, *Proc. IEEE Conference on Control Applications/Computer Aided Control System Design*, pp 339-344, Glasgow.

Wang, Z. and Appleton, E. (2003 a), A Void Shape Detecting Sensor for a Rescue Robot, *international journal of Industrial Robot*, No.5, pp 459-462.

Wang, Z. and Appleton, E. (2003 b), The Bristle Theory and Traction Experiment of a Brush Based Rescue Robot, *International Journal of Robotica*, Vol. 21, No.4, pp453-460.

Wang, Z. and Appleton, E. (2003 c), Bristle Mechanism Study of a Shape Reconfigurable Brush Robot, *international journal of Industrial Robot*, No.6, pp 543-551.

BIBLIOGRAPHY

ABAQUS/Post User's Manual, Version 5.6, Hibbitt, Karlsson & Sorensen, Inc. (1996).

ABAQUS/Standard Example Problems Manual, Version 5.6, Hibbitt, Karlsson & Sorensen, Inc. (1996).

Coiffet, P. and Chirouze, M. (1982), An Introduction to Robot Technology, London: Kogan Page Ltd.

Engelberger, J. (1980), Robotics in Practice, London: Kogan Page Limited.

Henning, W., Hickman, F., and Choset, H. (1998), Motion Planning for Serpentine Robots, *ASCE Space and Robotics Albuquerque*, New Mexico, USA.

Hershberger, D. and Murphy, R. (1999), Handling Sensing Failures in Autonomous Mobile Robots, *International Journal of Robotics Research*, Vol. 18, no. 4, pp. 382-400.

Liu, C., Zhang, K. and Sun, X. (1994), A Research of Robot Moving Inside Pipe, *ICARCV-International Conference*, Vol. 2, 3rd, Singapore, pp. 745-749.

Mali, A. and Murphy, R. (1997), Lessons Learned in Integrating Sensing into Autonomous Mobile Robot Architectures, *Journal of Experimental and Theoretical Artificial Intelligence*, special issue on Software Architectures for Hardware Agents, No. 9, (2), pp. 191-220.

McCarty, B. and Gilbert, S. (1998), Visual C++ 6 Programming Blue Book, Albany, New York: Coriolis Group Books.

Murphy, R. and Martinez, J. (1997), Lessons Learned from the NSF REU Site Grant: Multiple Autonomous Mobile Robots for Search and Rescue Applications, *Frontiers in Education.*

Murphy, R., Ausmus, M., Bugajska, M., Ellis, T., Johnson, T., Kelley, N., Kiefer, J. and Pollock, L. (1999), Marsupial-like Mobile Robot Societies, *IEEE Intelligent Systems,* Vol. 15, no. 3, pp. 364-365.

Murphy, R., Casper, J., Micire, M., and Hyams, J. (2000), Assessment of the NIST Standard Test Bed for Urban Search and Rescue, *NIST Workshop on Performance Metrics for Intelligent Systems.*

Murphy, R. (2000), Marsupial Robots for Urban Search and Rescue, *IEEE Intelligent Systems,* Vol. 15, no. 2, March, pp. 14-19.

Murray, W. and Pappas, C. (1995), The Visual C++ handbook, McGraw-Hill, 2nd version.

Prautsch, P., Mita, T. and Iwasaki, T. (2000), Analysis and Control of a Gait of Snake Robot, *Trans. IEE of Japan*, Vol. 120-D, No. 3, March.

Redern, D. and Campbell, C. (1998), The MATLAB 5 Handbook, New York: Springer.

Rogers, E., Thompson, C. and Murphy, R. (1997), Outbreak Agent: Intelligent Wearable Technology for Hazardous Environments, *International Conference on Systems, Man and Cybernetics*, pp. 3198-3203.

Rossmann, T. and Pfeiffer, F. (1996), Simulation and Control of a Pipe Crawling Robot, *Robotics and manufacturing, International Symposium*, May 2nd, Montpellier, pp. 683-690.

Rudall, B. (1996), Reports and Surveys, *Robotica*, Vol. 14, pp. 595-601.

Specification of Micro Variable Geometry Tracked Vehicle, Inuktun Services Ltd.

Specification of PCI-30F/G Data Acquisition Boards, (1999), Eagle Technology Ltd.

Specification of Rovver 900, Everest VIT.

Specification of Urban Robot Pebble, IS Robotics.

Sprouse, J. and Murphy, R. (1996), Strategies for Searching an Area with Semi-Autonomous Mobile Robots, *Robots for Challenging Environments 96*, June, Albuquerque, New Mexico.

Strain Gauge Users' Guide, Tokyo Sokki Kenkyujo Co. Ltd.

Sun, L., Sun, P., Qin, X. and Wang, C. (1998), Micro Robot in Small Pipe with Electromagnetic Actuator, *Proceedings of the International Symposium on Micromechatronics and Human Science*, Nov. 9th, Nagoya, Japan, pp. 243-248.

Tokuda, K., Osuka, K. and Ono, T. (1998), Rescue Robot CUL: Carry and Power Assist Robot for Unspecified Landform, *Control in natural disasters Workshop*, Sep., Tokyo, pp. 75-78.

Using Strand7: Introduction to Strand7 Finite Element Analysis System, (1999), G+D Computing Pty Ltd.

Xu, S. (1996), C Algorithm Programming Handbook, Tsinghua University Press, 2nd version (Chinese).

APPENDIX A

PROGRAM LIST

(1) *Beginnew*

```
#!/bin/csh
set filenum=flag.txt
mypoint:
echo w.dat have to run again
if(! -e $filenum) then
     echo w.dat is running now
     csh new
     goto mypoint
else
     goto myover
endif
myover:
echo w.dat is over
```

(2) *Myd.c*

```
#include <stdio.h>
#include <stdlib.h>
#include <string.h>
#include <ctype.h>
#include <math.h>
#define filedata force.dat
#define delf 0.3
#define maxforce -1.2
#define tiny 0.0001

main()
{
int i,j,xnum,ynum,filenum,num,forceitem;
float xforce,yforce,xf,yf;
FILE *fp,*fptemp,*fpdata,*fpinp,*fpori,*fptempdata,*fpflag;

char str3[6];
char str1[20];
char str4[20]="form";
char *str2=".txt";
char chtemp,chinp;

forceitem=abs(maxforce/delf);
printf("force=%d\n",forceitem);

if( (fpdata= fopen( "force.dat", "r" )) == NULL )
  {
    printf( "The force.dat file was not opened\n" );
```

```
    exit(0);
  }

fscanf(fpdata,"%f  %f  %d  %d  %d\n",&xforce,  &yforce,  &xnum,  &ynum,
&filenum);
xf=xforce;
yf=yforce;
num=filenum;
fclose(fpdata);
printf("first  %5.2f  %5.2f  %d  %d  %d\n",xforce,  yforce,  xnum,  ynum,
filenum);

if( (fptempdata= fopen( "tempforce.dat", "w+" )) == NULL )
  {
    printf( "The tempforce.dat file was not built\n" );
    exit(0);
  }

if(abs(xnum-0)>tiny)
{
    printf("here xnum<> 0\n");
    yforce=yforce+delf;
    ynum=ynum-1;
    filenum=filenum+1;
    printf("%5.2f %5.2f %d %d %d\n",xforce,yforce,xnum,ynum,filenum);
    if(abs(ynum-0)<tiny)
    {
        printf("here ynum==0\n");
        xnum=xnum-1;
        ynum=forceitem;
        yforce=maxforce;
        printf("yforce=%5.2f\n",yforce);
        xforce=xforce+delf;
    }
fprintf(fptempdata,"%5.2f  %5.2f  %d  %d  %d\n",xforce,  yforce,  xnum,
ynum, filenum);
}
else
{
 if( (fpflag= fopen( "flag.txt", "w+" )) == NULL )
  {
    printf( "The file flag.txt was not built\n" );
    exit(0);
  }
  else
   {
      fclose(fpflag);
   }
}
fclose(fptempdata);

if( (fptemp= fopen( "abaqus.rpt", "r" )) == NULL )
  {
    printf( "The file abaqus.rpt was not opened\n" );
    exit(0);
  }
  sprintf(str3,"%d",num);
  strcpy(str1,str4);
  strcat(str1,str3);
  printf("%s\n",str1);
  strcat(str1,str2);
```

```
  printf("%s\n",str1);
  if(fp= fopen( str1, "w+" ))
  {
    printf( "The file was built\n" );
  }
  while(!feof(fptemp))
  {
    printf("%c\n",chtemp);
    chtemp=fgetc(fptemp);
    fputc(chtemp,fp);
  }
  fclose(fp);
  fclose(fptemp);

  if( (fpinp=fopen("inpfile.inp", "w+" )) == NULL )
  {
    printf( "The file inpfile.inp was not built\n" );
    exit(0);
  }

  if( (fpori=fopen("origin.inp", "r" )) == NULL )
  {
    printf( "The file origin.inp was not opened\n" );
    exit(0);
  }

  while(!feof(fpori))
  {
    chinp=fgetc(fpori);
    if(chinp=='£')
    {
     fprintf(fpinp,"%5.2f",xforce);
    }
    if(chinp=='$')
    {
     fprintf(fpinp,"%5.2f",yforce);
    }
    if((chinp!='£')&&(chinp!='$'))
    {
       fputc(chinp,fpinp);
    }
   }
  fclose(fpinp);
}
```

(3) *Mydata1.c*

```
/* this is used to reformat data from form.txt and write them into a
f.txt, filenum is the amount of all data files which need to be
changed and items is the number of data lines in a form.txt. */
#include <stdio.h>
#include <stdlib.h>
#include <string.h>
#include <ctype.h>
#include <math.h>
#define filenum 781
#define items 400
#define tiny 0.0001
#define unitconvert 25.4
```

```
main()
{
  int i,num,j;
  float x,y,xd,yd;
  FILE *fpf,*fpform;
  char str3[6];
  char str1[20];
  char str4[20]="form";
  char str40[20]="f";
  char str10[20];
  char *str2=".txt";
  char strtemp[6],chtemp;

  for(i=1;i<=filenum;i++)
  {
    sprintf(str3,"%d",i);
    strcpy(str1,str4);
    strcpy(str10,str40);
    strcat(str1,str3);
    strcat(str10,str3);
    strcat(str1,str2);
    strcat(str10,str2);
    if(fpf= fopen( str10, "w+" ))
    {
      printf( "The file f was built\n" );
    }
    if( (fpform=fopen(str1, "r" )) == NULL )
    {
      printf( "The file form  was not open\n" );
      exit(0);
    }
    fseek(fpform,574L,0);
    for(j=1;j<=items;j++)
    {
      fscanf(fpform,"%d %f %f %f %f\n",&num,&x,&y,&xd,&yd);
      printf("%d  %6.2f  %6.2f  %f  %f\n",num,x,y,xd,yd);
      x=x*unitconvert;
      y=y*unitconvert;
      fprintf(fpf,"%6.3f %6.3f\n",x,y);
      printf("%6.3f  %6.3f\n",x,y);
    }
    fclose(fpf);
    fclose(fpform);
  }
}
```

(4) *Mylast*

```
sleep 60
chmod u+x abaqus.rpt
chmod u+x tempforce.dat
cp abaqus.rpt abaqus.txt
rm inpfile.inp
cp tempforce.dat force.dat
rm tempforce.dat
a.out
chmod u+x *
rm force.dat
rm try.*
rm abaqus.*
```

(5) *Myrpt*

```
#!/bin/csh
set fname=abaqus
myaga:
echo abaqus have to run post again
if((-e $fname.jnl)&&(-e $fname.rpt)) then
     echo post is running now
else
     goto myaga
endif
```

(6) *Myunix*

```
#!/bin/csh
set filename=try
myagain:
echo abaqus have to run standard again
if((((! -e $filename.023)&&(-e $filename.sta))&&(-e $filename.res))
then
     echo abaqus is running standard
else
     goto myagain
endif
```

(7) *New*

```
chmod u+x *
abaqus analysis job=try input=inpfile background
csh myunix
abaqus post res=try input=w1.jnl device=terminal background
chmod u+x *
csh myrpt
csh mylast
```

(8) *W1.jnl*

```
dra,displaced
print nodes
OUT
End
```

APPENDIX B

MEASUREMENT DATA

Shape measured by coordinate measuring machine										
Robot body unit fits in the square box		Robot body unit fits in the rectangular box		Robot body unit fits in the triangular box		Robot body unit fits in the hexagonal box		Robot body unit fits in the irregular box	
X	Y	X	Y	X	Y	X	Y	X	Y
2.337	104.401	1.988	100.428	1.179	115.048	1.816	102.988	0.704	103.071
10.367	104.401	9.994	100.386	9.109	114.726	9.733	102.545	8.671	102.809
18.376	104.45	17.983	100.266	16.993	113.875	17.604	101.575	16.611	102.262
26.373	104.404	25.952	99.969	24.804	112.491	25.41	100.123	24.515	101.381
34.33	104.088	33.889	99.391	32.506	110.582	33.119	98.222	32.36	100.14
42.231	103.359	41.776	98.44	40.067	108.154	40.719	95.903	40.133	98.498
50.045	102.082	49.58	97.033	47.434	105.216	48.195	93.197	47.795	96.433
57.703	100.128	57.254	95.094	54.594	101.781	55.531	90.115	55.328	93.918
65.093	97.411	64.741	92.566	61.491	97.865	62.702	86.68	62.682	90.927
72.13	93.858	71.987	89.386	68.113	93.477	69.707	82.897	69.82	87.45
78.66	89.465	78.896	85.557	74.406	88.65	76.512	78.776	76.686	83.475
84.553	84.265	85.391	81.053	80.358	83.395	83.1	74.318	83.244	79.006
89.715	78.323	91.395	75.912	85.934	77.735	89.453	69.524	89.432	74.051
94.058	71.754	96.832	70.184	91.09	71.706	95.505	64.409	95.214	68.626
97.554	64.689	101.843	63.92	95.805	65.326	101.256	58.945	100.536	62.755
100.206	57.246	105.801	57.194	100.057	58.626	106.662	53.123	105.358	56.467
102.066	49.563	109.28	50.095	103.831	51.651	111.655	46.95	109.633	49.811
103.229	41.725	112.093	42.693	107.114	44.422	116.164	40.436	113.339	42.808
103.827	33.805	114.255	35.07	109.887	36.988	120.121	33.568	116.433	35.522
104.011	25.852	115.819	27.292	112.141	29.379	123.438	26.383	118.898	27.998
103.918	17.859	116.844	19.422	113.856	21.626	126.016	18.914	120.722	20.286
103.731	9.852	117.408	11.494	115.016	13.774	127.746	11.219	121.891	12.455
103.627	3.833	117.588	3.543	115.509	7.841	128.514	3.381	122.405	4.555